8-2014

Incorporating Physics-Based Patterns into Geophysical and Geostatistical Estimation Algorithms

Erasmus Kofi Oware
Clemson University

Recommended Citation

Oware, Erasmus Kofi, "Incorporating Physics-Based Patterns into Geophysical and Geostatistical Estimation Algorithms" (2014). *All Dissertations*. 1767.
https://tigerprints.clemson.edu/all_dissertations/1767

INCORPORATING PHYSICS-BASED PATTERNS INTO GEOPHYSICAL AND GEOSTATISTICAL ESTIMATION ALGORITHMS

A Dissertation
Presented to
the Graduate School of
Clemson University

In Partial Fulfilment
of the Requirements for the Degree
Doctor of Philosophy
Environmental Engineering and Science

---

by
Erasmus Kofi Oware
August 2014

Accepted by:
Dr. Stephen Moysey, Committee Chair
Dr. Ron Falta
Dr. Lawrence Murdoch
Dr. Taufiquar Khan

GENERAL ABSTRACT

Geophysical imaging systems are inherently non-linear and plagued with the challenge of limited data. These drawbacks make the solution non-unique and sensitive to small data perturbations; hence, regularization is performed to stabilize the solution. Regularization involves the application of *a priori* specification of the target to modify the solution space in order to make it tractable. However, the traditionally applied regularization model constraints are independent of the physical mechanisms driving the spatiotemporal evolution of the target parameters. To address this limitation, we introduce an innovative inversion scheme, *basis-constrained inversion*, which seeks to leverage advances in mechanistic modeling of physical phenomena to mimic the physics of the target process, to be incorporated into the regularization of hydrogeophysical and geostatistical estimation algorithms, for improved subsurface characterization.

The fundamental protocol of the approach involves the construction of basis vectors from training images, which are then utilized to constrain the optimization problem. The training dataset is generated via Monte Carlo simulations to mimic the perceived physics of the processes prevailing within the system of interest. Two statistical techniques for constructing optimal basis functions, Proper Orthogonal Decomposition (POD) and Maximum Covariance Analysis (MCA), are employed leading to two inversion schemes. While POD is a static imaging technique, MCA is a dynamic inversion strategy. The efficacies of the proposed methodologies are demonstrated based on hypothetical and lab-scale flow and transport experiments.

DEDICATION

Dedicated to the memory of my grandma, Afia Nipaa; and to my lovely boys, Ethan and Ean, each equally my pride and joy.

ACKNOWLEGEMENTS

I would like to express my profound appreciation and gratitude to my doctoral advisor, Dr. Stephen Moysey, you have been a tremendous mentor for me. I could not have asked for a different doctoral advisor. I would like to thank you for the opportunity to work on this particular project, which has developed and shaped my career in a direction I could not have imagined four years ago. Your advice on both research as well as on my career have been indispensable. I would also like to thank Dr. Taufiquar Khan, your mathematical perspective provided an invaluable dimension to my dissertation. In the same vein, I would also like to thank my committee members, Prof. Ron Falta and Prof. Lawrence Murdoch. I want to thank you for letting my defense be an enjoyable moment, and for your brilliant comments and suggestions regarding potential applications of the techniques developed in this dissertation, thanks a lot.

A special thanks to my family. Words cannot express how grateful I am to my parents for all of the sacrifices they’ve made on my behalf. The financial difficulties they’ve endured just to ensure my education. Finally, my acknowledgement will not be complete if I fail to mention the innumerable sacrifices made by my beloved wife, Mrs. Augustina Oware, in shouldering far more than her fair quota of the parenting and household duties while I pursued my PhD. Her prayer for me was what sustained me.

TABLE OF CONTENTS

Page

Table of Contents (Continued)

Table of Contents (Continued)

Table of Contents (Continued)

Table of Contents (Continued)

LIST OF TABLES

Table Page

LIST OF FIGURES

Figure Page

List of Figures (Continued)

Figure Page

List of Figures (Continued)

List of Figures (Continued)

Figure Page

CHAPTER ONE

GENERAL INTRODUCTION

Accurate estimation of subsurface dynamic processes is critical to diverse applications. For example, subsurface characterization is of particular importance to the investigation of natural transient processes, such as infiltration of water [e.g., *Daily et al.*, 1992; *Hinnell et al.*, 2010; *Nenna et al.*, 2011], investigation of preferential flow pathways [*Gish et al.*, 2002; *Holden*, 2003; *Samouelian et al.*, 2003; *Truss et al.*, 2007], and prediction of transport of contaminants in porous media [e.g., *Binley et al.*, 1996; *Kemna et al.*, 2002; *Perri et al.*, 2012]. Investigation of the subsurface is also important for engineered systems, such as monitoring and evaluating the performance of remediation schemes [Lane *et al*., 2004, 2006; Hubbard *et al*., 2008; Johnson *et al.*, 2010)].

Geophysical imaging is a non-invasive approach for characterizing the subsurface. However, geophysical imaging problems are inherently ill-posed and non-linear [*Kirsch*, 1996], which require regularization [*Tikhonov and Arsenin,* 1977; *Greenhalgh et al*., 2006] to stabilize the resulting image. Regularization, by definition, involves utilizing *a priori* (data independent) information to constrain the optimization procedure, thereby making the ill-posed problem tractable.

Generally, Tikhonov-style regularization [*Tikhonov and Arsenin*, 1977] is the conventional approach used within geophysical imaging problems. The mathematical optimization framework for Tikhonov-style regularization consists of two parts: the data norm ($\mathbf{E}_d$) and the model regularization norm ($\mathbf{E}_m$), i.e.

$$E(\boldsymbol{\sigma}) = \mathbf{E}_d + \beta\mathbf{E}_m$$

$$= \left\|\mathbf{W}_d\left[\mathbf{V}_{obs} - \boldsymbol{f}_g(\boldsymbol{\sigma})\right]\right\|_2 + \beta\left\|\mathbf{W}\left(\boldsymbol{\sigma} - \boldsymbol{\sigma}_{ref}\right)\right\|_2, \quad (1.1)$$

where $\|\cdot\|_2$ shows the l_2-norm, $\boldsymbol{\sigma}$ signifies the target model parameters being estimated; $\boldsymbol{\sigma}_{ref}$ is a reference model representing assumed background values of the target; $\mathbf{V}_{obs}$ denotes measured data; $f_g(\boldsymbol{\sigma})$ represents synthetic data obtained from geophysical forward model, $f_g(\,.\,)$. The data weighting matrix, $\mathbf{W}_d$ represents the inverse of the covariance matrix. The first term in Eq.1.1 represents the data norm, which measures the agreement between the observed voltages with the synthetic voltages. The second term is the model regularization term that enforces *a priori* constraints for stabilizing the solution. The regularization parameter β weights the relative importance of the data norm and the model regularization terms. Finally, **W** is the regularization operator, which is used to enforce *a priori* relationship between parameters in the inversion scheme.

The design of the regularization filter, **W**, is crucial to the retrieval accuracy of the optimization process. There are three *a priori* spatial model assumptions commonly used in the traditional formulation of **W** in geophysical problems, namely: smallness, flatness, and smoothness constraints. The smallness regularization criterion seeks a solution that is closest to zero or some reference model, $\boldsymbol{\sigma}_{ref}$. The flatness constraint uses the 1st-order spatial derivative filter to minimize the difference between neighboring model parameters. In contrast, the smoothness constraint invokes smoothness in the distribution of the resultant estimated parameters through the use of the 2nd-order spatial derivative [e.g., *Tikhonov and Arsenin*, 1977; *Pidlisecky et al.,* 2007].

A notable drawback of the above listed traditional *a priori* model assumptions is that they are independent of the physical mechanisms of the underlying transport process that is driving the evolution of the target parameters. This limitation introduces artifacts in the tomograms [e.g., *Moysey and Knight*, 2004; *Moysey et al*., 2005]. For instance, *Day Lewis and Lane* [2004], in the context of inferring spatial statistics from radar tomograms, concluded that the influence of applied regularization criteria can erode the accuracy of estimating spatial covariance structure from tomograms. *Singha and Gorelick* [2005], in a field application, observed a drastic underestimation of mass of the initially injected solute from resistivity tomograms. These authors attributed the underestimation of mass to the suppression of estimated concentrations due to the effects of regularization.

Coupled inversion [e.g., *Rucker and Ferré*, 2004; *Ferré et al.*, 2009; *Hinnell et al.*, 2010, Fowler and Moysey, 2011], is a recent advancement in hydrogeophysical inversion that is geared toward leveraging our *a priori* understanding of the physics of the underlying transport process for the purpose of employing physics-based information in constraining the estimation of the desired parameters. In the coupled inversion framework, a hydrologic model is coupled with a geophysical model in an effort to calibrate the parameters of the hydrologic model. Here, in order to accomplish the coupling, the hydrologic variables (e.g., solute concentration) that we seek are directly coupled with their associated geophysical properties (e.g., electrical conductivity) via a petrophysical relationship [e.g., *Archie,* 1942]. The calibration of the hydrologic parameters then proceeds via least-squares minimization of the differences between observed and synthetic data.

Hinnell et al. [2010] compared the resolution powers of coupled and uncoupled inversion schemes through resistivity monitoring of one-dimensional infiltration and redistribution. In the event when the assumed process simulator was representative of the structural features of the actual field under investigation, the authors observed the performance of coupled approach to be superior in comparison with that of the uncoupled strategy in terms of prediction uncertainty of the hydrologic properties. They concluded that where there are structural errors in the assumed hydrologic simulator, coupled inversion may be inaccurate.

As a consequence, the recovered hydrologic patterns are limited to the hydrologic behaviors allowed for by the applied process simulator. It is reasonable, therefore, to assert that coupled inversion imposes an implicit hard process constraint on the inversion procedure.

Novel imaging strategies are proposed in this dissertation in an effort to address the combined drawbacks of both traditional Tikhonov regularization and coupled inversion strategies. The suggested techniques are envisioned to infuse non-parametric, site-specific, physics-based *a priori* information to constrain geophysical inversion procedures in a comparatively flexible fashion, i.e., by invoking soft process constraints.

The proposed approach for quantifying physics-based *a priori* information involves the extraction of basis functions from training images. Training images representing a particular site are generated via Monte Carlo simulations of the target process constrained to a conceptual model. The generated basis patterns are subsequently applied to constrain the geophysical optimization procedure.

The general hypotheses posed in this dissertation are:

(1) *Physics-based* s*oft process constraint can be implemented within existing Tikhonov scheme to improve retrieval accuracy of tomograms relative to the traditional Tikhonov and contemporary coupled inversion approaches.*

(2) *Physics-based coupled patterns captured between two adjacent time steps can be applied as* s*oft process constraints within existing Tikhonov framework to implement time-lapse monitoring of dynamic processes*.

Two statistical bases construction schemes are explored, Proper Orthogonal Decomposition (POD) and Maximum Covariance Analysis (MCA), leading to two basis-constrained imaging methodologies, namely:

i) POD-constrained inversion.

ii) MCA time-lapse inversion.

In principle, the basic dissimilarity between POD and MCA is that, whereas POD captures static (one time step) pattern information in the distribution of model parameters, MCA extracts dynamic (adjacent time periods) patterns that explain the evolution of the system across consecutive time periods. As a consequence, the proposed POD-based inversion denotes a static imaging technique, whereas MCA represents a time-lapse (dynamic) inversion strategy.

This dissertation comprises seven Chapters. While Chapters One and Seven provide general introduction and general conclusions, Chapters Two to Six introduce and evaluate the performance of the POD and MCA time-lapse inversion algorithms. Chapter Two introduces the original POD-constrained inversion algorithm. It also compares the accuracy of estimated concentrations based on the POD strategy with those estimated from the traditional Tikhonov and that of the contemporary coupled inversion schemes.

The importance of robustness of an estimation algorithm to data and model uncertainties cannot be overemphasized. To evaluate this important feature, Chapter Three appraises the robustness of the POD-constrained imaging methodology in the presence of manifold data and model input uncertainties.

Chapter Four focuses on the application of the POD algorithm to evaluate spatial moments of subsurface solute plumes. This is importance given the vital role that spatial moments of solute plumes play in various disciplines in environmental studies. Chapter Four also addresses a limitation of the original algorithm, which pertains to a lack of translation of the basis vectors in the original algorithm. To fix that, Chapter Four introduces an adaptive version of the POD algorithm that addresses this limitation.

It is important to emphasize that the evaluation of the POD algorithm in Chapters two to four are based on hypothetical saturated flow and transport experiments, which is an important step in the development of original geophysical estimation algorithms. While field-data presents a more complicated and realistic dataset, their geometry and statistical properties are not exactly known. This presents a challenge when it comes to the appraisal of the viability of an original algorithm. As a consequence, the utility of hypothetical models (parsimonious models) for the first stage of proof-of-concept is crucial, given that their geometry and statistical properties are exactly known, which enables us to evaluate and validate the viability of a proposed technique.

Inversion of real data, however, presents challenges such as measurement errors, non-parametric error distributions, lack of data sensitivity, faulty instruments, operational errors, etc. These challenges are usually simplified in hypothetical scenarios. To demonstrate the capability of the POD-constrained algorithm to invert real datasets, Chapter Five applies the POD algorithm to a lab-scale saline-tracer unsaturated flow experiment. It implements static imaging on time-lapse data. Finally, Chapter six introduces the MCA algorithm, which is a dynamic version of the POD-constrained algorithm. It also employs the same lab-scale dataset to illustrate the dynamic imaging capabilities of the MCA strategy.

This Chapter was originally published in Water Resources Research.

Oware et al. [2013] with doi:10.1002/wrcr.20462

CHAPTER TWO

PHYSICALLY-BASED REGULARIZATION OF HYDROGEOPHYSICAL INVERSE PROBLEMS FOR IMROVED IMAGING OF PROCESS-DRIVEN SYSTEMS

ABSTRACT

We introduce a new strategy for integrating hydrologic process information as a constraint within hydrogeophysical imaging problems. The approach uses a basis-constrained inversion where basis vectors are tuned to the hydrologic problem of interest. Tuning is achieved using proper orthogonal decomposition (POD) to extract an optimal basis from synthetic training data generated by Monte Carlo simulations representative of hydrologic processes at a site. A synthetic case study illustrates that the approach performs well relative to other common inversion strategies for imaging a solute plume using an electrical resistivity survey, even when the initial conceptualization of hydrologic processes is incorrect. In two synthetic case studies we found that the POD approach was able to significantly improve imaging of the plume by reducing the root mean square error of the concentration estimates by a factor of two. More importantly, the POD approach was able to better capture the bimodal nature of the plume in the second case study, even though the prior conceptual model for the POD basis was for a single plume. The ability of the POD inversion to improve concentration estimates exemplifies the importance of integrating process information within geophysical imaging problems. In contrast, the ability to capture the bimodality of the plume in the

second example indicates the flexibility of the technique to move away from this prior process constraint when it is inconsistent with the observed ERI data.

1. INTRODUCTION

There is growing interest in using geophysical methods, such as electrical resistivity imaging (ERI), to investigate systems where the evolution of subsurface properties through space and time are constrained by physical, chemical, or biologic processes, such as the infiltration of water or transport of solutes in porous media. Subsurface imaging using ERI, however, usually requires the solution of an ill-posed inverse problem. While there are a variety of approaches addressing this issue in the inverse theory literature, Tikhonov regularization [*Tikhonov and Arsenin*, 1977] is commonly applied to ERI as it readily allows spatial constraints, such as smoothly varying property variations, to be enforced in subsurface images [e.g., *Daily and Ramirez,* 1995; *LaBrecque and Yang*, 2001; *Kemna et al.*, 2002]. The spatial constraints applied in these inversions are typically generalized filters selected independently from the underlying processes affecting the target resistivity distribution (Figure 2.1a). In the context of imaging solute transport, it is well known that this regularization can lead to imaging artifacts causing problems with mass recovery and poor spatial resolution [e.g., *Singha and Gorlick,* 2005].

In contrast, an emerging approach known as coupled inversion explicitly takes advantage of the dependence of geophysical properties on subsurface processes by using geophysical measurements to calibrate the parameters of a hydrologic model [e.g., *Rucker and Ferré,* 2004; *Ferré et al.,* 2009; *Hinnell et al.*, 2010]. Figure 2.1b illustrates how the coupled hydrologic and geophysical models can be considered as a single model with hydrologic parameters as inputs and geophysical responses as outputs. An advantage of the technique is that the coupled process model may have only a few parameters that control the detailed spatial and temporal evolution of hydrologic state variables in the subsurface, which in turn control the geophysical response. Coupled inversion can therefore be viewed as an implicit form of regularization that enforces a physics-based constraint on the inversion through the physical process simulator, e.g., the flow and transport model. A disadvantage of the approach, however, is that poor results may be obtained if the hydrologic model is subject to conceptual or structural errors or the geophysical model fails to capture the influence of non-hydrologic factors, such as background variations in resistivity.

We propose a new approach for physics-based regularization of inverse problems that is dependent on, but less restricted by, assumptions about subsurface processes compared to coupled inversion (Figure 2.1c). The approach uses proper orthogonal decomposition (POD) [e.g, *Banks et al*., 2000; *Kunisch and Volkwein,* 2003; *Rathinam and Petzold*, 2004; *Pinnau*, 2008] of a set of training data generated by Monte Carlo simulation of a hydrologic process to generate an optimal set of basis vectors for the imaging problem. These hydrologically “tuned” basis vectors are subsequently used within a basis-constrained inversion framework to obtain a resistivity image.

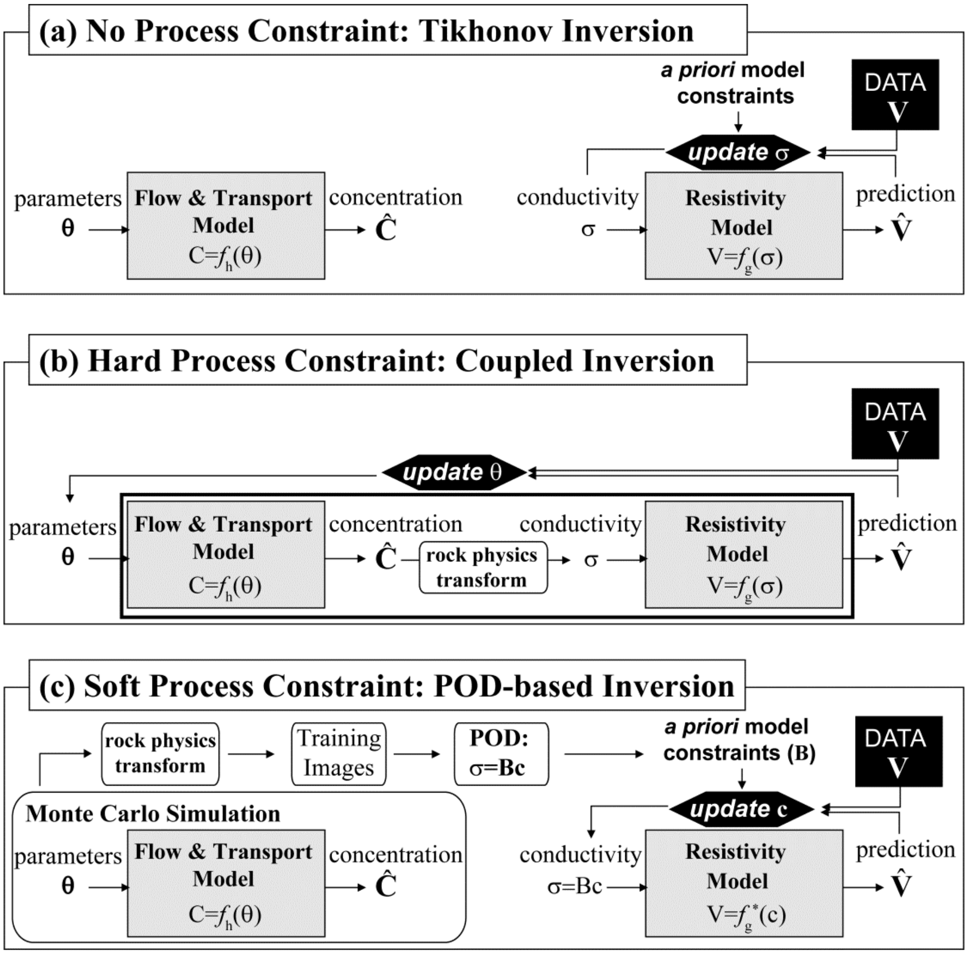

Figure 2.1: Schematic comparison of the (a) Tikhonov, (b) coupled, and (c) POD-based inversion strategies.

To our knowledge this work is the first use of POD to constrain geophysical inversions by physical process information. The use of training data to characterize spatially-distributed patterns, however, is well established in a variety of fields in the geosciences. For example, the adoption of training images to infer spatial patterns in applications of multiple-point geostatitistics [e.g., *Strebelle*, 2000] is increasingly common. *Moysey et al*. [2005] applied the training data concept by using geostatistically-based Monte Carlo simulations of geophysical surveys to quantitatively capture and correct for spatially-variable inversion artifacts associated with non-linear imaging problems. Similarly, *Lehikoinen et al.* [2010] used Monte Carlo simulations of flow in a heterogeneous vadose zone to construct a statistical model of approximation errors resulting from the assumption of a homogenous medium, which they were subsequently able to utilize within a Kalman filter to improve resistivity imaging of water content changes. The use of simulations and training data to capture relevant information to constrain estimation and imaging problems is, therefore, already well-established in the literature. The key contribution of this work is establishing the use of POD to capture patterns from training data and efficiently integrate this information as a constraint within an inverse problem.

In this paper, we compare the results of POD-based inversion to results obtained using standard Tikhonov regularization techniques and coupled inversion for a problem where ERI is used to image a solute plume. We investigate two distinct scenarios; one where the *a priori* understanding of flow and transport utilized in generating the training images for the inversions is correct and one where the training data are inconsistent with the actual processes.

2. POD-BASED IMAGING STRATEGY FOR ERI

Details of ERI have been described by many authors [e.g., *Kemna et al.*, 2002]. In principle, ERI surveys operate by sequentially applying electric currents (I) to the subsurface using different pairs of current electrodes. The resulting voltage responses (V_{obs}) are measured at potential electrodes and depend strongly on the electrical conductivity distribution of the subsurface σ, where each element σ_m represents the electrical conductivity at spatial location x_m and electrical resistivity is the inverse of conductivity ($1/\sigma_m$). The inverse or "imaging" problem involves estimating the conductivity distribution σ from the voltage observations V_{obs}. The Tikhonov objective function (Eq.1) addresses the ill-posed nature of the inverse problem by minimizing data misfit (E_d) subject to a model regularization constraint (E_m), where β is a tradeoff parameter that balances these two objectives, $f_g(\cdot)$ represents the resistivity forward model, W is a spatial filter, and σ_o is a reference model or *a priori* estimate of conductivity.

$$E(\boldsymbol{\sigma}) = E_d + \beta E_m = \left\| \mathbf{V_{obs}} - f_g\left(\boldsymbol{\sigma}\right) \right\|_2 + \beta \left\| \mathbf{W}\left(\boldsymbol{\sigma} - \boldsymbol{\sigma}_{\mathbf{o}}\right) \right\|_2 \tag{1}$$

Basis-constrained inversions or subspace solutions [Greenhalgh et al., 2006] restrict the inverse problem by assuming that a finite number of orthogonal spatial (or spatiotemporal) basis functions can be linearly recombined using an appropriate set of scaling coefficients **c** to reconstruct $\boldsymbol{\sigma}$ within a specified level of accuracy (i.e., approximation errors given by $\boldsymbol{\varepsilon} = \boldsymbol{\sigma} - \hat{\boldsymbol{\sigma}}$).

$$\boldsymbol{\sigma} \approx \hat{\boldsymbol{\sigma}} = \mathbf{Bc} \tag{2}$$

Here the N_p columns of the matrix **B** each contain a basis vector of length N_m that captures a particular spatial pattern needed to reproduce $\boldsymbol{\sigma}$. Given a known set of basis vectors, **B**, the basis constrained inversion can be obtained by substituting the expansion of $\boldsymbol{\sigma}$ from Eq.2 into an appropriate objective function, i.e., Eq.1. A regularization filter $\tilde{\mathbf{W}}$ can be designed to place an *a priori* constraint directly on **c**, e.g., to force coefficients of unnecessary basis vectors toward zero, or can be derived from spatial constraints on $\boldsymbol{\sigma}$ by projecting a desired spatial filter (i.e., **W**) onto the basis (i.e., $\tilde{\mathbf{W}} = \mathbf{WB}$). Likewise, the reference model for the coefficients $\mathbf{c_o}$ can be obtained by projection of $\boldsymbol{\sigma}_\mathbf{o}$ onto the basis. The modified function $f_g^*(\cdot)$ in Eq.3 denotes that the electrical conductivity distribution must be reconstructed from the current estimate of **c** prior to applying the geophysical forward model $f_g(\cdot)$ to simulate the voltage responses. Given that only a few basis vectors may be needed to reconstruct $\boldsymbol{\sigma}$ within an acceptable level of error [*Jin et al.*, 2011], the basis constrained inversion should generally be more stable than standard inversion strategies as fewer parameters need to be estimated (i.e., $N_p \ll N_m$). For this to be true, however, the basis vectors in **B** must be selected to allow for the reconstruction of $\boldsymbol{\sigma}$ in an efficient and accurate manner.

$$\begin{aligned} E(\mathbf{c}) &\approx \left\| \mathbf{V_{obs}} - f_g\left(\mathbf{Bc}\right) \right\|_2 + \beta \left\| \mathbf{W}\left(\mathbf{Bc} - \mathbf{Bc_o}\right) \right\|_2 \\ &= \left\| \mathbf{V_{obs}} - f_g^*\left(\mathbf{c}\right) \right\|_2 + \beta \left\| \tilde{\mathbf{W}}\left(\mathbf{c} - \mathbf{c_o}\right) \right\|_2 \end{aligned} \tag{3}$$

Selection of an optimal basis constraint to minimize N_p for a particular subsurface process is not trivial. If a representative training data set is available, however, proper orthogonal decomposition (POD), which is also known as principal component analysis (PCA) or the Karhunen-Loève (KL) transform, can be used to derive an optimal orthogonal basis where the maximum amount of variability in the training data set (in a least-squares sense) is captured with the fewest number of basis vectors [*Pinnau*, 2008]. While this decomposition is commonly used for image compression, pattern recognition, data analysis, and model order reduction in computational applications, it presents a challenge for subsurface imaging problems since high-resolution databases of real geologic environments do not exist. We suggest that this problem can be addressed by using Monte Carlo simulations of subsurface processes to produce a set of training data that captures general *patterns* of subsurface variability expected for $\boldsymbol{\sigma}$ at a particular site, which can subsequently be analyzed by POD (or equivalently PCA) to generate the basis.

3. METHODS

3.1 Simulation Overview for Test Scenarios

We use a numerical test to compare the performance of ERI for imaging a solute plume using the POD approach versus standard Tikhonov methods and coupled inversion. The simulation domain for the tests consists of a 50m x 50m vertical cross section discretized into 0.5m x 0.5m cells. Refer to Figure 2.2 for an illustration of the experimental setup. The true target electrical conductivity distribution is obtained by simulating conservative solute transport through a heterogeneous hydraulic conductivity (K) field. The K field is generated using the algorithm SGSIM [*Deutsch and Journel,* 1998] for a log-normal hydrologic conductivity distribution with mean ln(K) = -4.6 and variance ln(K) = 0.39 to produce K values (in m/s) typical of a silty sand [Freeze and Cherry, 1979]. The spatial variability of the K field is described using an isotropic exponential variogram model with a correlation length of 25m. The longitudinal dispersivity and porosity throughout the domain are fixed to values of 3.0m and 0.3, respectively. A uniform unit hydraulic gradient drives mean horizontal flow, while zero flux conditions were applied at the top and bottom boundaries of the domain.

Two different transport scenarios are considered to test the ERI inversion techniques. In the first synthetic case the solute originates from a single source location (x=2.5m, z=10m) with an initial fixed concentration of 2g/L, thereby producing a unimodal plume at the time of imaging (see Figure 2.5a). In contrast, the solute originates from two distinct source zones in the second scenario (x_1=2.5m, z_1=7.5m and x_2=4m, z_2=10m) each with an initial concentration of 2g/L, thereby producing a bimodal plume as the imaging target (see Figure 2.5e). The initial background concentration in the aquifer was assumed to be uniform and equal to 140mg/L. The total solute mass in the imaged area, including the background solutes, is therefore 1.6kg for synthetic #1 and 1.8kg for synthetic #2. The calculated values reported for the simulations in Table 2.1 are lower by approximately 1% and 3%, respectively, due to numerical errors in the transport simulation. All concentration boundary conditions were fixed to the background concentration throughout the simulation. Both the flow and transport simulations were performed using a finite-difference code written in MATLAB.

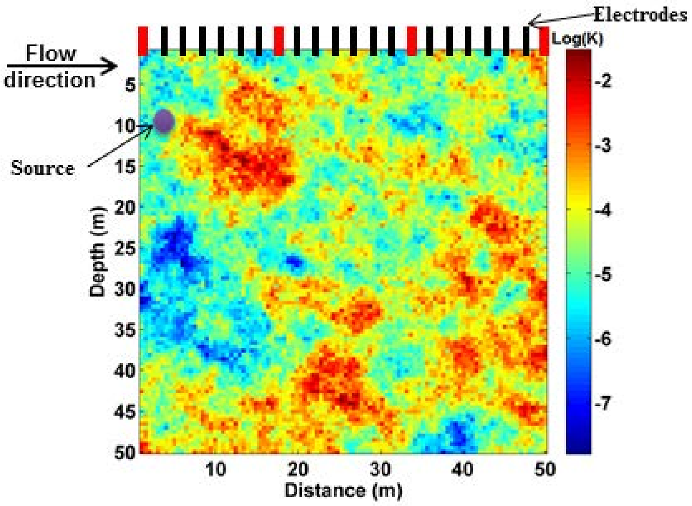

Figure 2.2: Schematic illustration of the experimental setup of the 2-D flow and transport in a random hydraulic conductivity field, along with the resistivity survey design. While the red electrodes served as both current and potential electrodes, the black electrodes were used exclusively as potential electrodes.

Solute concentrations were converted to electrical conductivities using Archie's law: $\sigma(x) = \sigma_f n^m$, where n is porosity, the cementation exponent, *m*, was fixed to 1.3, and the electrical conductivity (S/m) of the fluid, σ_f, is assumed to be 1.5x10^{-4} times the solute concentration (given in mg/L) [*Lesmes and Friedman*, 2005]. Dipole-pole surveys were performed using a total of 22 electrodes deployed along the upper surface of the simulation domain (see Figure 2.2), four of which were utilized as current electrodes. The voltage potential resulting from six independent current injections were monitored at all remaining 20 electrodes, thereby producing 120 voltage measurements for each survey. All ERI forward simulations were performed using a modified version of the MATLAB code by *Pidlisecky et al.* [2007]. Notably, all of the ERI surveys are performed for the single observation time t=5.85 years after the release of the solutes, i.e., the surveys do not represent time-lapse measurements.

Table 2.1: Summary of metrics for concentration and conductivity values estimated by ERI for the single source (synthetic #1) and dual source (synthetics #2) transport scenarios. TI Mean refers to estimates obtained by taking the mean of the training images obtained by Monte Carlo flow and transport simulation, which are independent of the geophysical data.

		Total Mass (kg)	Max Value		RMSE	
			Conc. (g/L)	Log(σ)	Conc. (g/L)	Log(σ)
Synthetic #1	True Plume	1.58	1.18	-3.30	-	-
	TI Mean	1.56	1.14	-3.34	0.08	0.18
	Tikhonov	1.56	0.38	-4.43	0.07	0.17
	Coupled	1.51	0.51	-4.14	0.07	0.17
	POD	1.60	1.45	-3.09	0.03	0.07
Synthetic #2	True Plume	1.75	1.79	-2.88	-	-
	TI Mean	1.56	1.14	-3.34	0.13	0.28
	Tikhonov	1.63	0.93	-3.53	0.12	0.25
	Coupled	1.62	0.63	-3.93	0.12	0.25
	POD	1.70	1.64	-2.97	0.08	0.12

3.2 Details for the ERI Inversions

Standard Tikhonov regularization of the ERI data using spatial smoothness and model smallness constraints was performed using RESINVM3D [*Pidlisecky et al.,* 2007]. An additional depth weighting factor equivalent to $1/z^2$ was used to penalize against changes in $\boldsymbol{\sigma}$ near the electrode locations as suggested by *Pidlisecky et al.* [2007]. The reference model $\boldsymbol{\sigma_o}$ was set to a constant value based on the initial solute concentration in the aquifer. The regularization parameter β was optimized by trial and error.

Models of varying complexity can be utilized to represent flow and transport in a heterogeneous domain for the coupled inversion approach. We chose to use a very simple conceptual model given by the 2-D analytical solution for uniform lateral flow in Eq.4 [*De Josselin De Jong*, 1958]. The use of this model implicitly assumes that the influence of the hydraulic conductivity heterogeneity on the solute can be captured by effective transport parameters, which is clearly not an accurate assumption since the second synthetic example has two solute sources whereas the model assumes a single source. Regardless, we chose this simplified model to highlight strengths and weaknesses of the coupled inversion approach when model errors exist. We do not suggest that this is the only choice or even the optimal choice for providing accurate images of the plume using the coupled inversion approach.

$$C(x,z,t) = \frac{C_0 A}{4\pi t (D_L D_T)^{1/2}} \exp\left\{-\frac{[(x - x_0) - v_x t]^2}{4 D_L t} - \frac{(z - z_0)^2}{4 D_T t}\right\}, \qquad (4)$$

The initial tracer concentration C_o is injected over an area A at location (x_o,z_o), such that the total solute mass in the system is given by $M=C_oA$. The plume moves through the aquifer with a velocity v_x and the concentration at time t after tracer injection is $C(x,z,t)$. The longitudinal (D_L) and traverse (D_T) dispersion coefficients are defined as the product of velocity and dispersivity (α), i.e., $D_j = v_x \alpha_j$, where for this example we chose α_L=3.0m, and α_T=α_L/3. We recognize that this choice is not general and limits the ability of the model to reproduce a full range of plume aspect ratios, but the limitation does not impact the conclusions made in this study. Since dispersion is controlled by the plume velocity and transport time in this model, there are three parameters in Eq.4 to be estimated: the mass of solute released from the source (M), the average lateral velocity of the plume (v_x), and the total time since the release of the plume (t). We used the trust-region-reflective optimization algorithm *lsqnonlin* in MATLAB [*Coleman and Li*, 1996] to perform this optimization subject to the constraint that all three model parameters are positive.

Training data for the POD-based inversions were obtained by simulating flow and transport for the same conditions as the reference model with a single source zone, except that each simulation used an independent, randomly generated hydraulic conductivity realization. To account for the fact that the true spatial structure of the subsurface would normally be uncertain, the K realizations were simulated using four different correlation lengths (15, 20, 25, and 30m). A total of 400 flow and transport simulations were performed. Each resulting concentration image was transformed to electrical conductivity using the form of Archie's law given earlier. Maps showing the mean and standard deviation of the training images are given in Figures 3a and 3b, respectively.

Four sample realizations illustrating differences in the morphology of the plumes in the training images are also given (Figures 2.3c-f).

Prior to extraction of the basis vectors from the training data the center of mass for each realization was calculated and the plumes were aligned to the true center of mass for the reference (i.e., true) plume. The plume centering step accounts for the translational dependence of the individual realizations in the training data and therefore reduces the number of realizations required to capture patterns that characterize an individual plume. We assume that the plume center of mass could generally be estimated directly from resistivity data based on the results of *Fowler and Moysey* [2011], who used numerical models to demonstrate that the effective plume velocity – which can be directly related to the center of mass – can be accurately estimated with a single four-electrode array, and *Pidlisecky et al.* [2011], who used a moment-based inversion to improve plume imaging, though this work was demonstrated for cross-borehole ground-penetrating radar tomography, which has significantly different data sensitivities from ground-based resistivity surveys. The impact of our assumption is explored in the Discussion section of this paper, but we suggest investigation of robust methods for the estimation of the center of mass of a plume using resistivity surveys in complex, heterogeneous flow systems as a future research direction.

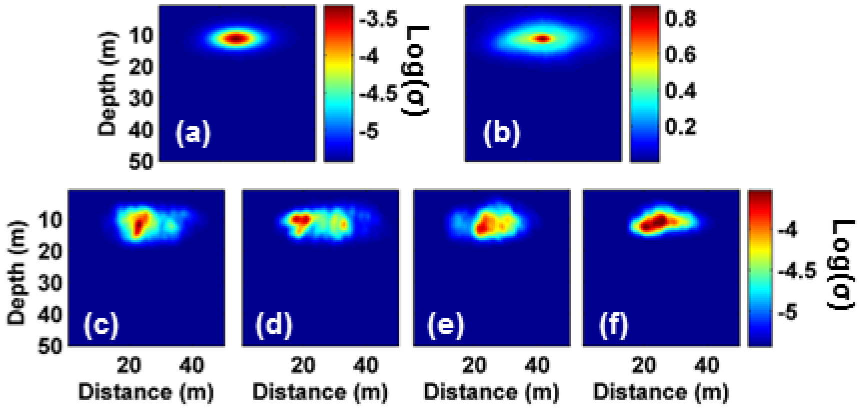

Figure 2.3: Mean (a) and standard deviation (b) maps of the log-electrical conductivity for the 400 images in the training data. Four sample realizations are shown in c-f to illustrate the variability in the shape of the plumes observed in the realizations. Note that the realizations have been shifted such that the center of mass of each plume is aligned with the center of mass of the true plume.

Singular value decomposition of the training data set was used to calculate the POD basis vectors [*Pinnau*, 2008], of which the first 300 were retained as these could account for 99.6% of the variability in the training data set. Since only one coefficient needs to be estimated for each basis vector, this represents a 97% reduction in the number of parameters to be estimated in the inversion relative to the 10,000 pixels of the original $\boldsymbol{\sigma}$ image. Examples of the patterns captured from the training data are illustrated by the first 20 POD basis vectors given in Figure 2.4.

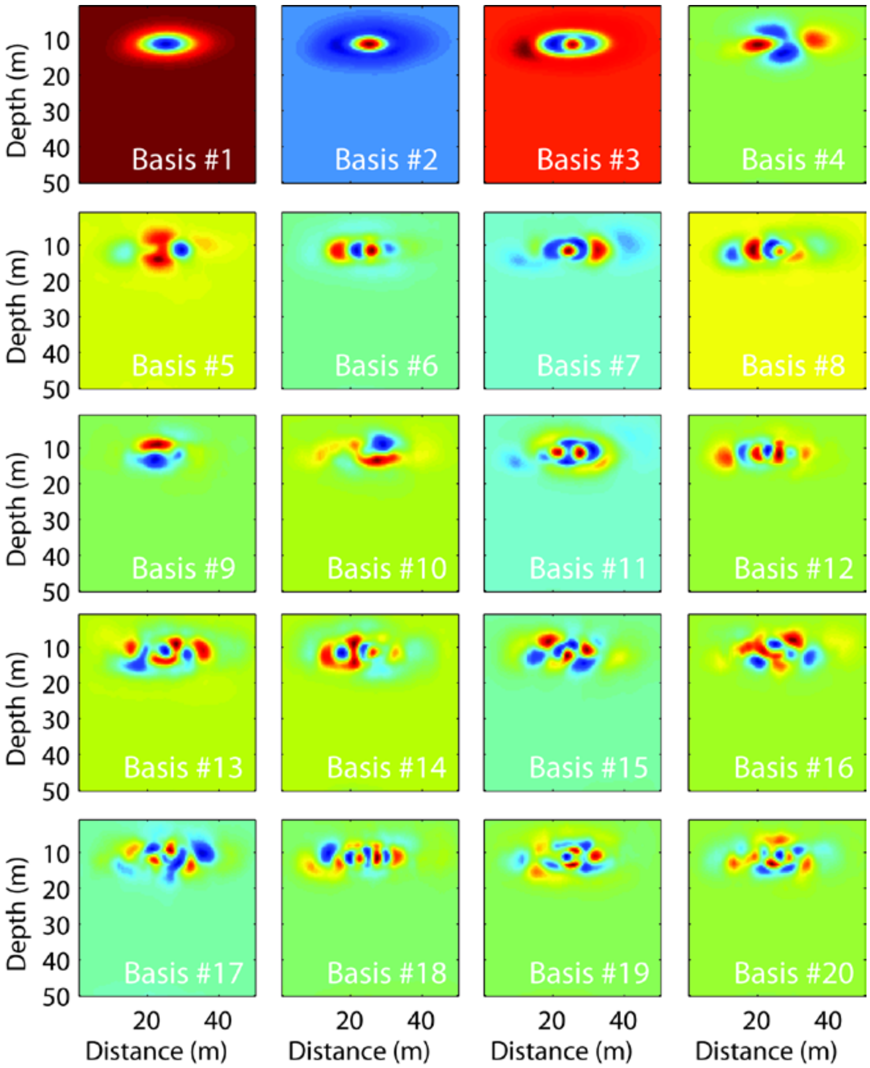

Figure 2.4: Examples of the top 20 most important POD basis images extracted from the training data set.

The regularization operator $\tilde{\mathbf{W}}$ used in Eq.2 consisted of two components. First, the same depth weighting function and spatial smoothness constraints on electrical conductivity used in the traditional Tikhonov regularization approach, i.e., **W**, were applied here by projecting the previous regularization operator onto the basis vectors obtained from the training data, i.e., $\tilde{\mathbf{W}}_1 = \mathbf{WB}$. Second, a diagonal operator ($\tilde{\mathbf{W}}_2$) containing the inverse of the singular values derived from the SVD of the training data was added to $\tilde{\mathbf{W}}_1$ to force the basis coefficients, i.e., **c**, toward zero with a preference to retain the basis vectors most representative of the training data. This constraint enforces a bias to produce ERI results that are similar to the mean of the training images. The overall regularization operator used in Eq.2 for the basis constrained inversion is therefore $\tilde{\mathbf{W}}^T\tilde{\mathbf{W}} = \tilde{\mathbf{W}}_1{}^T\tilde{\mathbf{W}}_1 + \gamma\tilde{\mathbf{W}}_2 = \mathbf{B}^T\,\mathbf{W}^T\mathbf{WB} + \gamma\tilde{\mathbf{W}}_2$, where the parameter γ is an additional regularization parameter providing a relative weighting between these two terms. The reference model $\mathbf{c_0}$ was obtained from projection of $\boldsymbol{\sigma_0}$ onto **B**.

Estimates of electrical conductivity obtained by each inversion technique were subsequently back converted to concentrations according to Archie’s law, as presented earlier. A variety of metrics were then evaluated for each image to quantitatively compare the inversion strategies. The metrics used here include root mean square error (RMSE) of the estimated concentrations, maximum (peak) plume concentration, and total plume mass (zeroth-order spatial moment).

4. RESULTS AND DISCUSSION

A comparison of the electrical conductivity images estimated by each of the three different inversion schemes is given in Figure 2.5 and comparisons of the true and estimated concentrations are given in Figure 2.6. A summary of the metrics used to compare the estimated results to the true plume is given in Table 1.

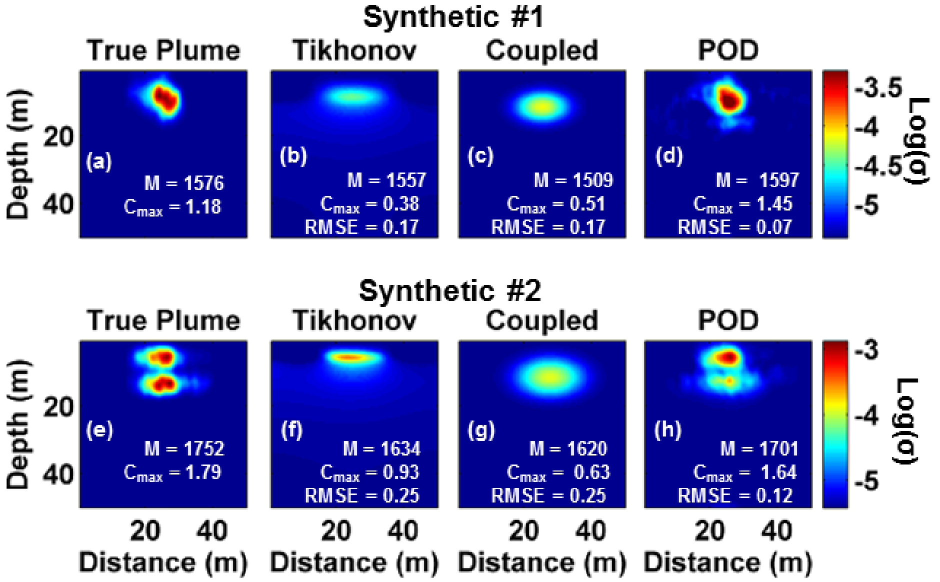

Figure 2.5: True (a,e) and estimated conductivity tomograms for Tikhonov regularization with spatial constraints (b,f), coupled inversion (c,g), and POD-based inversion for transport scenario 1 (unimodal plume; top row) and scenario 2 (bimodal plume; bottom row). Inset on each plot is the root mean square error (RMSE), maximum estimated concentration (Peak; mg/L), and total estimated mass of solute (Mass; g).

For synthetic #1, i.e., the scenario with a single solute source and unimodal plume, the traditional Tikhonov inversion with smoothness and smallness constraints produces an overly smooth and damped image compared to the true plume (Figure 2.5b). As a result, the estimated concentrations are low compared to their true values (Figure 6a), resulting in a high concentration RMSE of 70mg/L. The peak concentration of the plume is also greatly underestimated at 380mg/L versus 1180mg/L for the true plume, i.e., a 68% error. The total mass of the estimated plume is 1.56kg versus 1.58kg, thus yielding only a 1% error for this example. In this case the low mass error is presumably a result of the fact that the smoothness constraint in the Tikhonov inversion forces the estimated plume to spread out over a much larger region of the subsurface than the true plume, which compensates for the low concentration estimates.

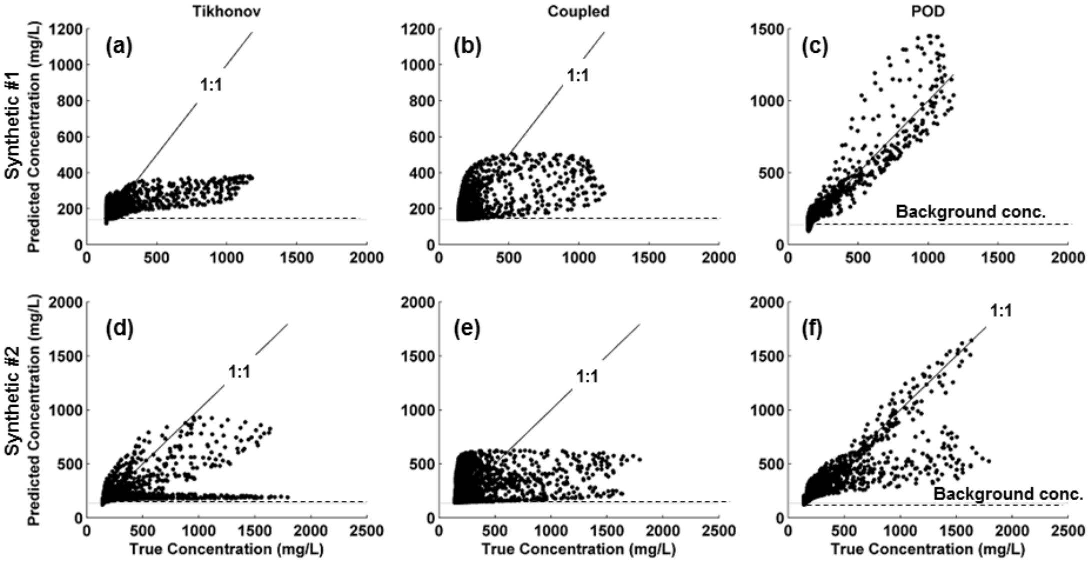

Figure 2.6: Scatterplots showing accuracy of concentration estimates for Tikhonov regularization with spatial constraints (a,d), coupled inversion (b,e), and POD-based inversion (c,f). The dashed line in each figure shows the background concentration of the aquifer (140mg/L).

Coupled inversion does a better job capturing the compact morphology of the plume for synthetic #1 (Figure 2.5c). The limitations of the analytical transport model are clear, however, as the irregular shape and off-axis rotation of the true plume cannot be reproduced. We emphasize that these particular issues are limitations of the analytical model selected for this example, not inherent limitations of the coupled inversion approach. Regardless, the analytical model facilitates localization of the solute mass within a distinct plume, thus allowing the estimate of the peak concentration to increase to 510mg/L, which yields an error of 57% (a decrease of 11% compared to the Tikhonov approach). The average concentration misfit as quantified by the RMSE is similar to that observed for the Tikhonov inversion (70mg/L), but the error for the estimated total solute mass (M=1.51kg) is slightly higher in this case.

The POD-based inversion provides the best overall estimate of both plume morphology and concentrations (Figure 2.5d and 2.6c). The peak plume concentration estimated by the POD approach is 1450mg/L, which is an overestimate of the true peak concentration by 23%. From Figure 2.6c, however, it is clear that only a small percentage of the 10,000 pixels in the image are significantly overestimated, whereas the concentration underestimation that occurred for the Tikhonov and coupled inversions was more systematic. The total mass is also slightly overestimated, but with an error similar in magnitude to the other two inversion approaches (i.e., 1%). The concentration RMSE in this case is only 30mg/L, however, which indicates a marked improvement in the overall reproduction of the solute plume concentrations compared to either the Tikhonov or coupled inversion approach.

Given that the POD inversion is dependent on the simulated training images to obtain the basis functions, it is important to evaluate whether the ERI data actually improved the concentration estimates or if the POD inversion results simply reflect the mean behavior of the training data. In other words, we ask the question “Could an equally good estimation result be obtained using stochastic simulation alone?”. Comparing the image obtained by taking the mean of the training realizations (Figure 2.3a) to the true plume (Figure 2.5a), it is apparent that the resulting images are substantially different. The RMSE obtained for the mean of the concentration realizations is 80mg/L, which is higher than that obtained for any of the other ERI-based imaging methods. The total mass and peak concentration estimated from the mean of the realizations, however, are similar to their true values. The high degree of misfit indicated by the RMSE, but good match for the other two plume metrics suggests that the realizations capture some general characteristics of the true plume that are independent of the specific spatial distribution of the solute concentrations. Including the ERI data in the estimation problem focuses the image toward the specific subsurface distribution of concentration for the true plume.

As pointed out earlier, we made the assumption in this work that it would be possible to shift the training images to the true center of mass of the plume prior to performing the POD analysis. To assess the significance of this assumption, we explored the performance of the POD inversion under varying degrees of error in the estimated center of mass. To account for differences in the lateral and vertical sensitivity of resistivity data, we considered cases where the estimated center of mass was shifted either laterally or diagonally relative to the true center of mass for the reference plume. In an effort to gain quantitative insight into how the magnitude of the positioning error affected the imaging results, we tested cases where the training images were shifted by 10, 25, 50, 75, and 100% of the width of the plume (as quantified by the second spatial moment of the plume [Freyberg, 1986]).

Overall the POD inversion appears to be relatively robust to errors in the plume's estimated center of mass. Figure 2.7 qualitatively illustrates that lateral shifts in the plume center of mass are minor for synthetic #1 until the training data are shifted by an entire plume-width. In contrast, the image degrades significantly when the plume is shifted by 50% of its width in the diagonal direction. These results are shown quantitatively in Figure 2.8 for both synthetic #1 and #2, where the RMSE of the estimated log-conductivity image does not become greater than that obtained using either the Tikhonov or coupled inversion strategies until the training images are shifted by at least 25% of the reference plume's width. It is also clear from this plot that lateral errors in the plume center of mass generally produce small increases in the imaging error.

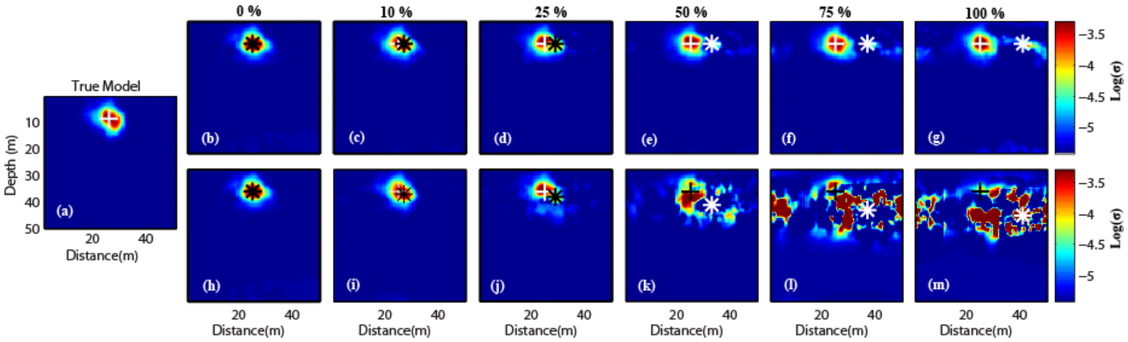

Figure 2.7: True plume (a) versus estimated conductivity tomograms obtained when the center of mass of the training images used for the POD inversion is shifted longitudinally (first row, b-g) and diagonally (second row, h-m). The white + in each image denotes the position of the center of mass of the true plume, whereas the * indicates the center of mass used to shift the training images; the title above each column indicates the magnitude of the shift as a percentage of the plume width.

Synthetic #2 was a more complicated problem in the sense that the two solute sources produced a bimodal plume (Figure 2.5e). Since the Tikhonov inversion makes no assumptions about the underlying processes generating the target conductivity distribution, there is no conceptual inconsistency introduced in the imaging problem compared to synthetic #1. The resistivity survey, however, consisted of only 120 measurements over a limited range of electrode separations. The sensitivity of the resistivity measurements for this data poor survey are therefore limited for imaging the deeper part of the plume in this particular example. The result is that the upper portion of the plume is still not well estimated and the lower part is completely missed by the survey (Figure 2.5f). The plume metrics from Table 1 now indicate a significant underestimation of total mass (7%), peak concentration (48%), and high RMSE (120mg/L) for the Tikhonov-based estimates.

The coupled inversion approach produces similarly poor estimation results based on the concentration metrics from Table 1 (7% error in total mass, 65% error in peak concentration, and 120mg/L concentration RMSE). Figure 2.4g shows that the reason for this poor estimation is somewhat different than the Tikhonov case. The estimated plume for the coupled inversion has shifted downward and grown to reflect the greater size of the true bimodal plume. Since the analytical model used in the inversion only allows for plumes with a single peak, the coupled inversion produced a result that spread the solute mass over a larger part of the subsurface to account for the larger distribution of mass of the true plume.

An improved estimate of the plume could, of course, be achieved by coupled inversion if the transport model were updated to allow for bimodal plumes, e.g., by using superposition of two unimodal plumes or increasing the degree of complexity by using a numerical transport model with multiple sources and heterogeneous flow and transport parameters. The point of our example, however, is to very simply illustrate the problem that occurs when the hydrologic conceptual model is inaccurate, not to illustrate which method can produce the best possible image when the conceptual model is correct. Our belief is that coupled inversion is the optimal approach for inversion when an accurate hydrologic model is available and estimating the value of the model parameters is the goal, though research is still continuing on this front.

The training images used for the POD analysis were also based on the incorrect conceptual model of a single solute source. The fact that the concentration realizations, which are the same ones used in synthetic #1, capture the behavior of the incorrect conceptual model is made clear by comparing the mean image in Figure 3a to the true plume in Figure 2.5e. Likewise the plume metrics for the training image realizations indicate a significant underestimation of mass 11% error) and peak concentration (36% error) because the second plume was not included within the conceptual model used to generate the realizations.

Despite the incorrect conceptual model used to generate the training images for synthetic #2, the POD inversion result suggests that the ERI data are able to compensate to obtain a much improved estimate for the bimodal plume. The POD inversion is able to recover 97% of the total solute mass, underestimates the peak concentration of the plume by only 8%, and has a concentration RMSE of 120mg/L, which is a factor of two less than the other methods. More importantly, the plume image in Figure 2.5h suggests that the assumption of a unimodal plume for the distribution of solute mass may not be appropriate. Though the bimodal plume is not fully reproduced, the imaging result does suggest that a reconceptualization of the underlying transport model would be appropriate. In this way, the POD approach shows flexibility in moving estimates away from our preconceptions, while still providing the ability to account for the morphologic characteristics imparted to the target by the driving physical processes.

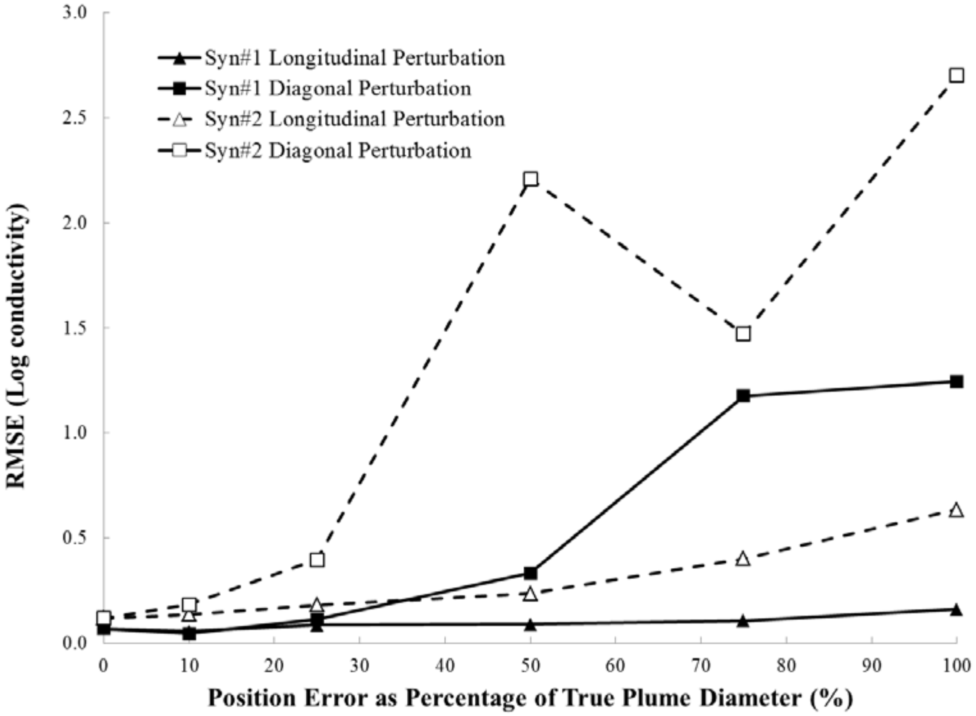

Figure 2.8: Change in RMSE for the estimated conductivity images as a function of the position error for the plume center of mass used to shift the training images prior in the POD analysis.

5. CONCLUSIONS

In this paper we presented a new approach for integrating process-based information within geophysical inversions. Specifically, proper orthogonal decomposition (POD) was used to extract a set of basis vectors for the imaging problem that are “tuned” for a particular hydrologic problem of interest using Monte Carlo simulation. We explored the approach here using two synthetic examples, one with a single source zone and one with two source zones leading to the formation of a bimodal plume.

Although the examples presented here are simple, they effectively illustrate the potential of the POD-based inversion strategy for enforcing physical or biogeochemical process constraints on geophysical inverse problems. When the conceptual transport model was correct in the first scenario, both coupled and POD-based inversions are able to produce better estimates of the target plume than the Tikhonov inversion. In contrast, the coupled inversion failed when the conceptual model of transport was incorrect in the second scenario. The POD inversion, however, captured the bimodality of the plume by constraining the inversion by *a priori* process information while retaining the flexibility to honor observed geophysical data.

The POD inversion is therefore a promising intermediate approach for enforcing physics-based regularization in a wide array of geophysical inverse problems. When a process controlling the imaging target is not known or highly uncertain, the POD approach is unlikely to perform better than standard Tikhonov methods since the range of results captured by a process simulator could be large. In contrast, when processes at a site are known and well understood, the coupled inversion approach can be an excellent choice for parameterizing models of the flow system. The POD approach is therefore an intermediate strategy that should be applied in cases where the processes are generally known, but not fully defined.

Additional research is needed to more fully evaluate how uncertainty in site processes affects the overall performance of the POD approach compared to existing Tikhonov and coupled inversion techniques. This work, however, provides a first introduction to the technique and the synthetic examples illustrate how it may perform for real imaging problems. Many questions remain to be addressed in the future, however, such as how robust the technique is in the presence of noisy data?, what is the role of data coverage on estimation accuracy?, how uncertain and/or non-linear a hydrologic model must be before the POD approach will not work?, how will performance be affected by considering a three-dimensional system?, and what methods may be used for efficient solutions to estimate the POD coefficients and assess the imaging results. We therefore feel that the POD methodology provides a novel new approach for geophysical imaging that is ripe for future exploration.

REFERENCES

Banks, H.T., M.L. Joyner, B. Wincheski, and W.P. Winfree (2000), Nondestructive evaluation using a reduced-order computational methodology, *Inverse Problems*, 16, 929-945

Coleman, T.F., and Y. Li (1996), An interior, trust region approach for nonlinear minimization subject to bounds, *SIAM J. Optim*., 6, 418-445.

Daily, W., and A. Ramirez (1995), Electrical-resistance tomography during *in-situ* trichloroethylene remediation at the Savanna river site, *Journal of Applied Geophysics*, 33, 239-201.

De Josselin De Jong, G. (1958), Longitudinal and transverse diffusion in granular deposits, *Trans. AGU*, 39, 1-6.

Deutsch, C.V., and A.G. Journel (1998), *GSLIB: Geostatistical software library and user's guide*, Oxford Univ. Press, New York.

Ferré, T., L. Bentley, A. Binley, N. Linde, A. Kemna, K. Singha, K. Holliger, J. A. Huisman, and B. Minsley (2009), Critical steps for the continuing advancement of hydrogeophysics, *EOS Trans. AGU, 90(23)*, 200, doi:10.1029/2009Eo230004.

Fowler, D.E., and S.M.J. Moysey (2011), Estimation of aquifer transport parameters from resistivity monitoring data within a coupled inversion framework, *Journal of Hydrology*, 409, 545-554, doi:10.1016/j.jhydrol.2011.08.063.

Freyberg, D.L. (1986), A natural gradient experiment on solute transport in a sand aquifer: 2. Spatial moments and the advection and dispersion of nonreactive tracers, *Water Resources Research*, 22(13), 2031-2046, doi:10.1029/WR022i013p02031.

Jin, B., T. Khan, and P. Maass (2011), A reconstruction algorithm for electrical impedance tomography based on sparsity regularization, *Int. J. Num. Methods in Engineering*, 89, 337-353, doi:10.1002/nme.3247.

Greenhalgh, S.A., Z. Bing, and A. Green (2006), Solutions, algorithms and interrelationships for local minimization search geophysical inversion, *Journal of Geophysics and Engineering*, 3, 101-113, doi:10.1088/1742-2132/3/2/001.

Hinnell, A.C., T.P.A. Ferre, J.A. Vrugt, J.A. Huisman, S. Moysey, J. Rings, and M.B. Kowalsky (2010), Improved extraction of hydrologic information from geophysical data through coupled hydrogeophysical inversion, *Water Resources Research*, 46, W00D40, doi:10.1029/2008WR007060.

Kemna, A., J. Vanderborght, B. Kulessa, and H. Vereecken (2002), Imaging and characterisation of subsurface solute transport using electrical resistivity tomography (ERT) and equivalent transport models, *Journal of Hydrology*, 267, 125-146.

Kunisch, K., and S. Volkwein (2003), Galerkin Proper Orthogonal Decomposition for a General Equation in Fluid Dynamics, *SIAM Journal on Numerical Analysis*, 40(2), 492-515.

LaBrecque, D.J., and X. Yang, (2001), Difference inversion of ERT data; A fast inversion method for 3-D *in-situ* monitoring, *Journal of Environmental and Engineering Geophysics*, 6(2), 83-89.

Lehikoinen, A., J. M. J. Huttunen, S. Finsterle, M. B. Kowalsky, and J. P. Kaipio (2010), Dynamic inversion for hydrogeophysical process monitoring with electrical resistance tomography under model uncertainties, *Water Resources Research*, 46, doi:10.1029/2009WR008470.

Lesmes, D.P., and S.P. Friedman (2005), Relationships between the electrical and hydrogeological properties of rocks and soils, in: Y. Rubin and S.S. Hubbard (Eds.), *Hydrogeophysics*,. Springer, Dordrecht, The Netherlands, pp. 87–128.

Moysey, M. S., K. Singha, and R. Knight (2005), A framework for inferring field-scale rock physics relationship through numerical simulation, *Geophys. Res. Lett., 32,* L083, doi:10.1029/2004GL022152.

Pidlisecky, A., E. Haber, and R. Knight (2007), RESINVM3D: A 3D resistivity inversion package, *Geophysics,* 72(2), H1-H10, doi:10.1190/1.2402499.

Pidlisecky, A., K. Singha, and F.D. Day-Lewis (2011), A distribution-based parameterization for improved tomographic imaging of solute plumes, *Geophys. J. Int.*, 187, 214-224, doi:10.1111/j.1365-246X.2011.05131.x.

Pinnau, R. (2008), Model reduction via proper orthogonal decomposition, in: W.H.A. Schilder and H. van der Vorst, *Model Order Reduction: Theory, Research Aspects and Applications,* Springer, New York, pp. 96-109.

Rathinam, M., and L.R. Petzold (2004), A new look at Proper Orthogonal Decomposition, *SIAM Journal on Numerical Analysis*, 41(5), 1893-1925.

Rucker, D. F., and T. P. A. Ferré (2004), Parameter estimation for soil hydraulic properties using zero-offset borehole radar: Analytical method, *Soil Sci. Soc. Am. J.*, 68, 1560–1567.

Singha, K., and S.M. Gorelick (2005), Saline tracer visualized with three-dimensional electrical resistivity tomography: Field-scale spatial moment analysis, *Water Resources Research*, 41, W05023, doi:10.1029/2004WR003460.

Strebelle, S., 2000, *Sequential simulation drawing structures from training images*, Ph.D. Dissertation, Stanford University, Stanford, CA, 187pp.

Tikhonov, A.N., and V. Y. Arsenin (1977), Solutions of ill-posed problems, *John Wiley & Sons*.

CHAPTER THREE

ASSESSING THE ROBUSTNESS OF A POD-BASED INVERSION SCHEME FOR RESISTIVITY IMGAGING OF SOLUTE PLUMES.

ABSTRACT

Understanding the potential impacts of input data and model uncertainties on model resolution in geophysical estimation algorithms is crucial. We present an appraisal of the robustness of the recently developed POD-constrained inversion algorithm. Two hypothetical flow and transport scenarios were utilized as test cases. Uncertainties were evaluated based on three distinct error components, namely: (1) measurement errors, (2) uncertain *a priori* hypotheses and model complexity, and (3) varying data coverage.

We noted increasing deterioration of model resolution with increasing measurement noise, which goes to emphasize the effects of the extensively researched bottleneck of measurement errors in geophysical investigations. Also, increasing the number of inversion parameters from 100 to 300 produced only marginal or no improvement in model resolution. This finding illustrates a potential application of the POD-algorithm for lossless truncation in the dimensionality of resistivity inverse problems, which can result in gains in computational overhead and potential reduction of ill-posedness. Root mean square error of log electrical conductivity respectively ranged from 0.07 to 0.17 and 0.12 to 0.3, in transitioning from a scenario with a fully understood conceptual model to a case where inaccurate *a priori* hypothesis underpinned the reconstruction. This demonstrates

the vital importance of *a priori* constraints on the performance of the POD algorithm. Finally, utilization of more data samples may not necessarily translate into gains in model resolution without considering optimal array configuration. An increase in the number of data samples seems to exaggerate the impact of data noise on model resolution. Also, there appears to be a trade-off relationship between data noise, data coverage, and accuracy of *a priori* constraints. The exaggerated effect of noise as a result of increased data samples is worsened by inaccurate basis constraints. This observation underscores the importance of optimal survey configuration as opposed to increasing data coverage. It also implies that improving our conceptual understanding of a system can presumably enhance the robustness of the POD-algorithm to measurement errors.

1. INTROUCTION

Geophysical imaging systems are inherently non-linear and plagued with limited data [*Kirsch*, 1996] as compared to the number of model parameters to estimate. These challenges make the solution non-unique and sensitive to small data perturbations. Regularization is, therefore, performed to stabilize the solution. Regularization involves the utilization of *a priori* understanding of the system of interest to condition the problem in order to make it tractable.

Tikhonov regularization [*Tikhonov and Arsenin*, 1977] is often employed in geophysical imaging algorithms. It enforces spatial model constraints that seek a realistic and spatially coherent solution. There are three *a priori* spatial model constraints commonly utilized in the Tikhonov regularization: smallness, flatness, and smoothness constraints. The smallness regularization criterion seeks a solution that is closest to zero or some baseline value. The flatness constraint uses the 1st-order spatial derivative filter to minimize the difference between neighboring model parameters. In contrast, the smoothness constraint uses the 2nd-order spatial derivative to penalize for roughness in the distribution of the solution.

Tikhonov regularization enforces spatial constraints without considering the physics of the processes controlling the migration of the target parameters. To address this limitation, *Oware et al*. [2013] introduced the POD-constrained inversion strategy that implements physics-based regularization within a Tikhonov inversion framework.

Understanding the potential impacts of input data and model uncertainties on model resolution in geophysical estimation algorithms is critical to the generalizability of the strategy. Toward this end, the objective of this Chapter is to evaluate and appraise the robustness of the POD-constrained inversion algorithm.

Rodgers [1990] characterizes inversion retrieval errors into three broad components, namely: (1) random errors that stem from measurement noise. (2) systematic errors as a result of inexact system parameters and inverse model bias, and (3) null space errors attributable to insufficient observational data. The retrieval error components specified by *Rodgers* [1990] are adapted as a guideline to design, evaluate, and appraise the robustness of the POD-constrained algorithm in this study. It is important to emphasize that these error constituents may be insufficient assess the robustness of the POD inversion scheme; however, they provide reasonable bases for testing the validity of the technique.

In this Chapter, descriptions of the design of experiments according to the error component specifications by *Rodgers* [1990] are presented in section 2. Results and discussion of salient findings are detailed in section 3 whiles section 4 outlines the principal conclusions of the study.

2. METHODS

Detailed discussion of the theoretical underpinning of the POD-constrained inversion algorithm is provided in Chapter 2 Section 2. Details of the hydrological simulations of the two hypothetical test cases and details regarding the ERI inversions are presented in Chapter 2 sections 3.1 and 3.2, respectively.

The relevant protocols for assessing the robustness of the POD-based inversion algorithm were designed according to the three retrieval error components outlined by *Rodgers* [1990].

To assess error Component One, which arises as a result of measurement noise, three conditions of data inexactness were explored. Noise-free data were corrupted with Gaussian noise according to the following noise model:

$$\mathbf{d}_{noise} = \mathbf{d}_{no\_noise} + n_{per} \cdot \mathbf{d}_{no_{noise}} \cdot \mathrm{N}(0,1), \qquad (1)$$

where $\mathbf{d}_{noise}$ and $\mathbf{d}_{no\_noise}$ represent the corrupted and noise-free data, respectively. n_{per} denotes the proportion of the voltage signal applied to corrupt the noise-free data. $\mathrm{N}(0,1)$ signifies a random normal distribution with zero mean and standard deviation of one.

To test error Component Two, which stems from uncertainty in model parameters and inverse model errors, two scenarios of flow and transport with accurate and inaccurate *a priori* specifications were investigated. The same synthetic examples used by *Oware et al*. [2013] were applied here. In addition, inversions based on 100 and 300 basis functions were explored. It should be noted that, in principle, the number of basis functions utilized implicitly characterizes the quantity of *a priori* information incorporated.

To address error Component Three, which deals with varying data coverage, two observing systems with 120 and 560 data samples were studied. To achieve this, the number of source electrodes applied for current injection (see Chapter 2 section 3.1) was doubled from four to eight. This increased the number of independent current injections from 6 to 28 resulting in 120 and 560 resistivity measurements, respectively.

All the data inversions are performed based on the prescribed combinations of error components presented in Table 3.1. In all, a total of 12 data inversions were performed for each of the two transport scenarios investigated.

Table 3.1: Combinations of parameters of error components investigated to characterize the robustness of the POD inversion algorithm. Each model uncertainty was investigated in terms of varying data coverage, signal noise additive, and number of basis vectors applied. A total of 12 data inversions were performed for each flow and transport scenario considered.

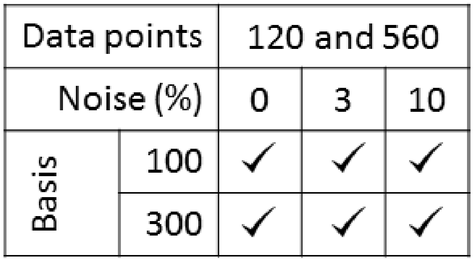

Data points		120 and 560		
Noise (%)		0	3	10
Basis	100	✓	✓	✓
	300	✓	✓	✓

3. RESULTS AND DISCUSSION

In the context of error Component One, model resolution was found to degrade with increasing data corruption (Figures 3.1, 3.2, 3.3, and 3.4). This observation is expected because the excitation of the noise-free data with random noise diminishes the quality of resistivity measurements applied in the data inversion.

Concerning the assessment of error component two, increasing the number of basis vectors utilized in the inversion from 100 to 300 results in only marginal or no improvement in the model resolution (Figures 3.1, 3.2a, 3.2b, 3.3, 3.4a, and 3.4b). This is presumably due to the marginal gain in the associated singular value weights contribution of the first 100 basis vectors in contrast with that of the first 300 basis functions.

Particularly, whereas the first 100 singular values accounted for 97.99% of the total singular values weight extracted from the training dataset, that of the first 300 contributed

98.99%, representing a marginal increase of 1%. This observation suggests that increasing the number of basis vectors applied in the inversion, without a corresponding increase in the variability of the applied basis patterns as a result of the additional basis vectors, will only increase the number of parameters to be estimated without a commensurate gain in model resolution. It should be noted that the first basis function alone accounted for 89.27% of the total singular value weights. This suggests that we possibly could have performed further truncation in the number of basis vectors applied without much loss in the model resolution.

Furthermore, while RMSE for synthetic #1 (i.e., the scenario with accurate *a priori* hypothesis) ranges from 0.07 to 0.17 (Figure 3.2), that of synthetic #2 (i.e., the case with incorrect *a priori* assumption) varies from 0.12 to 0.3 (Figure 3.4). The comparatively smaller RMSE values associated with reconstructions involving the target with accurate understanding of the underlying flow and transport process, in contrast with that of the scenario involving incorrect *a priori* hypothesis, demonstrates the critical importance of accurate *a priori* information in the performance of the POD-constrained inversion algorithm.

With respect to error component three, increasing data coverage from 120 to 560 data points almost invariably results in degradation of model resolution (Figures 3.1, 3.2c, 3.2d, 3.3, 3.4c, and 3.4d). This observation appears to be more severe at the 10% noise level, in the case of synthetic #2 (Figures 3.4c and 3.4d). This phenomenon is presumably attributable to a lack of optimal survey configuration involving the observing system of the 560 data samples as compared to that of the 120 data coverage. It must be emphasized that optimal array configuration was not considered in selecting the two observing systems here.

In addition, we postulate that the aggregate impact of increasing data noise on model resolution appears to be exaggerated with increasing number of data samples. This exaggerated aggregate effect of noise appears multiplied in the case of synthetic #2 where the basis functions were also inaccurate. This suggests a trade-off relationship between data noise, data coverage, and accuracy of basis functions. This implies that increasing data coverage, in an effort to reduce the null-space (unobserved space), does not necessarily translate into improvement in the model resolution.

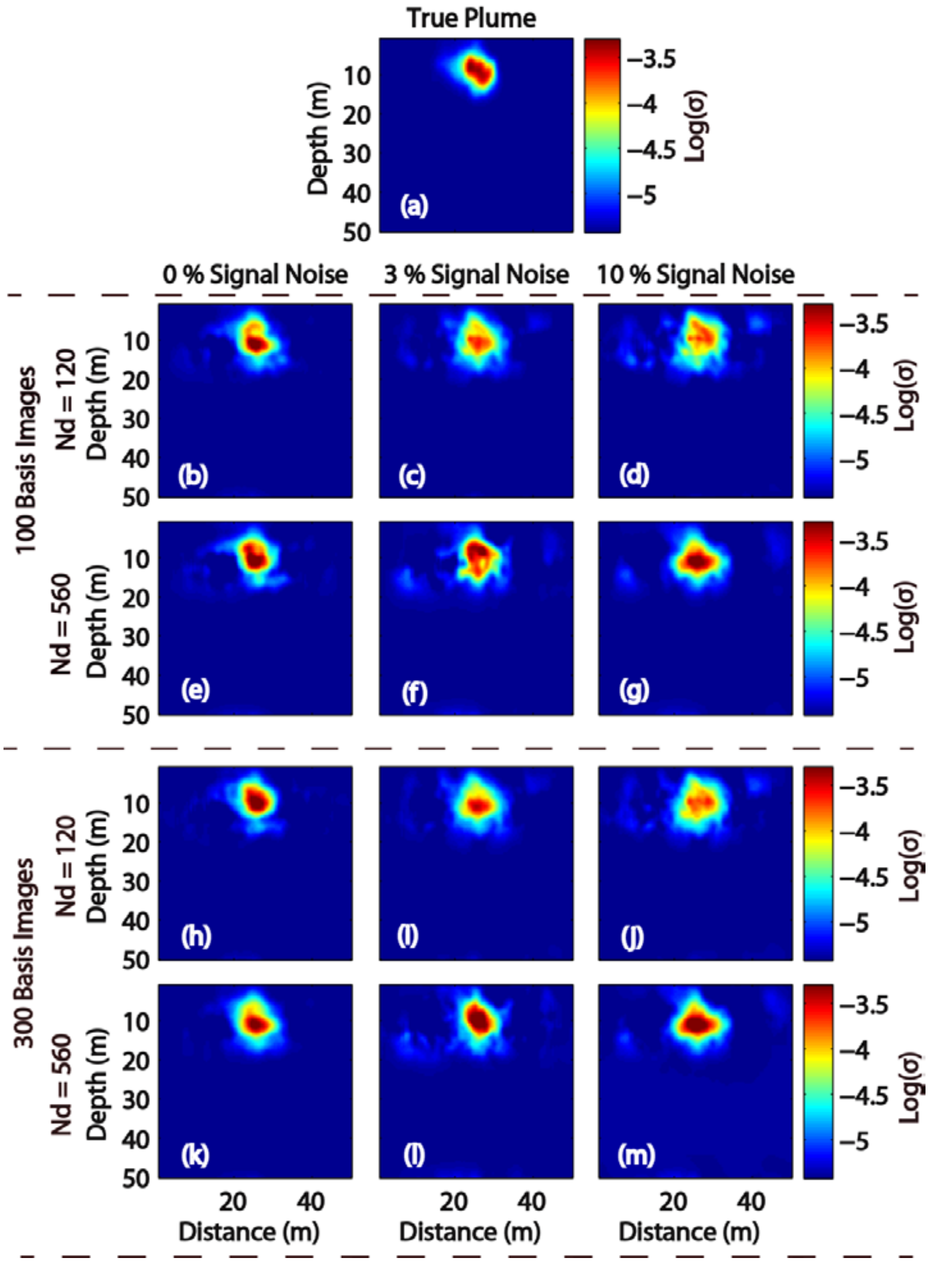

Figure 3.1: Reconstruction of log of electrical conductivity distributions. (a) Synthetic #1; Rows 1 and 2 utilized 100 basis (b-g), rows 3 and 4 utilized 300 basis (h-m); rows 1 and 3 utilized 120 data samples (b-d and h-j), rows 2 and 4 utilized 560 data samples (e-g and k-m). Columns 1, 2, and 3 represent signal noise cases 0, 3, and 10 %, respectively.

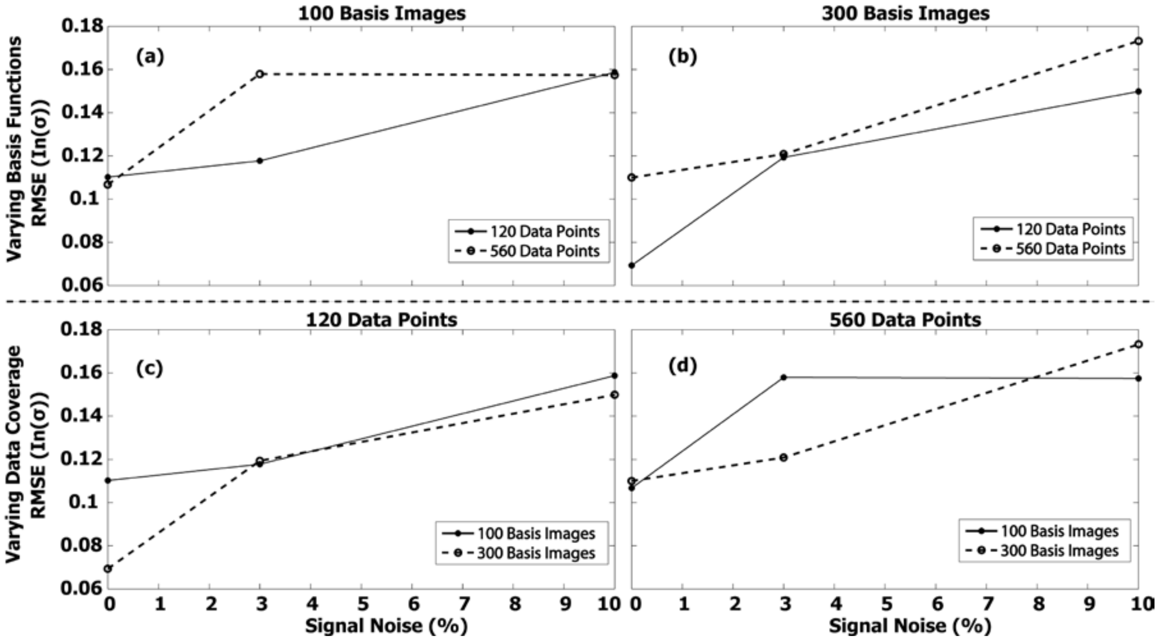

Figure 3.2: Root mean square errors (RMSE) versus signal noise for synthetic #1. Application of 120 and 560 data samples based on (a) 100 basis functions, and (b) 300 basis function; Utilization of 100 and 300 basis functions based on (a) 120 data points, and (b) 560 data points. Note that the plots are on the same axis to provide a sense of scale.

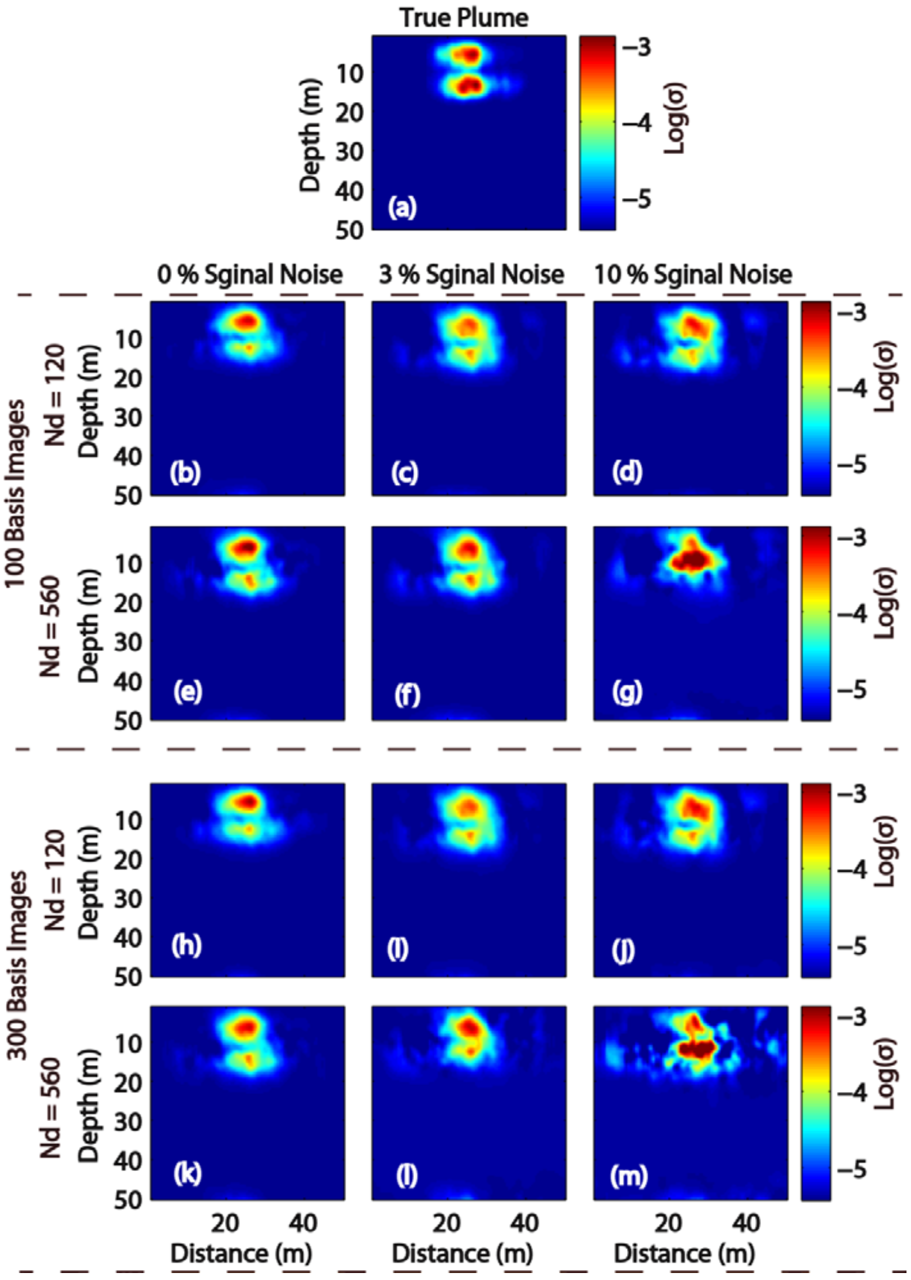

Figure 3.3: Reconstruction of log of electrical conductivity distributions. (a) Synthetic #2; Rows 1 and 2 utilized 100 basis (b-g), rows 3 and 4 utilized 300 basis (h-m); rows 1 and 3 utilized 120 data samples (b-d and h-j), rows 2 and 4 utilized 560 data samples (e-g and k-m). Columns 1, 2, and 3 represent signal noise cases 0, 3, and 10 %, respectively.

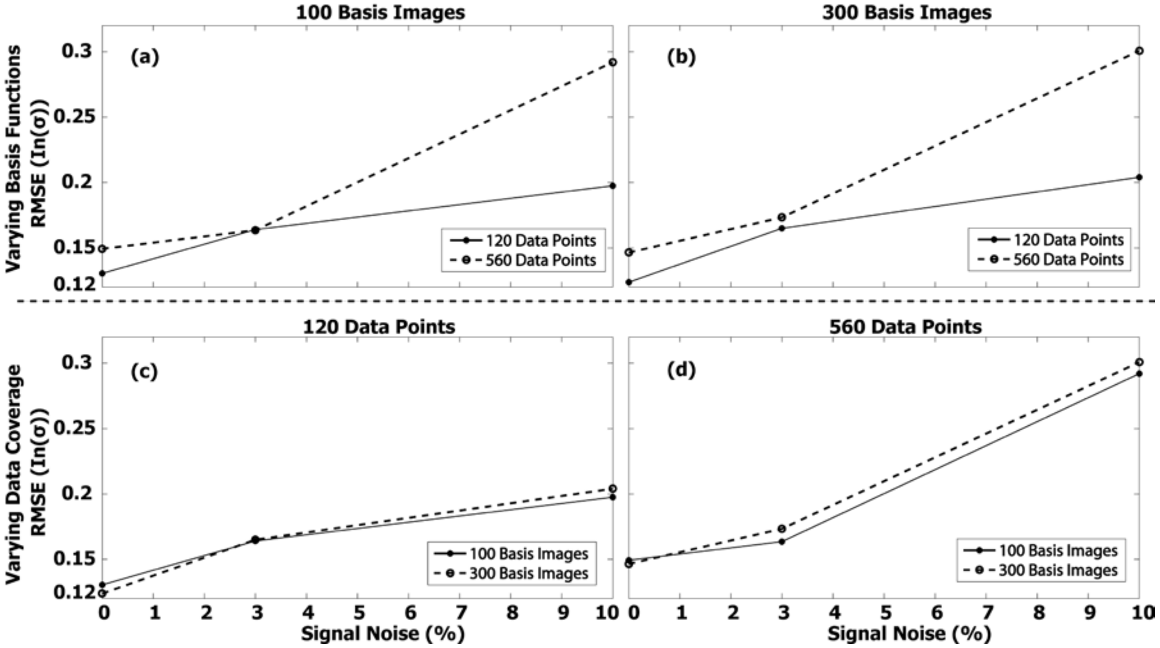

Figure 3.4: Root mean square error (RMSE) versus signal noise for synthetic #2. Application of 120 and 560 data samples based on (a) 100 basis functions, and (b) 300 basis function; Utilization of 100 and 300 basis functions based on (a) 120 data points, and (b) 560 data points. Note that the plots are on the same axis to provide a sense of scale.

4. CONCLUSION

In this contribution, we performed characterization and error analysis of the POD-constrained inversion algorithm originally presented by *Oware et al*. [2013]. Two hypothetical flow and transport scenarios were utilized as test cases. Uncertainties were evaluated based on three distinct error components, namely: (1) measurement errors, (2) uncertain *a priori* hypothesis, and (3) varying data coverage.

On measurement errors, we observed increasing deterioration of model resolution with increasing measurements noise. This goes to emphasize the effects of measurement errors in geophysical investigations, which is extensively documented.

Despite the advances in computational and parallel computing capabilities in recent years, there still exists the need to reduce the number of inversion parameters in geophysical imaging in a lossless fashion, in an effort to increase our capabilities to handle large-scale, 3D imaging problems, especially in field applications. Reducing the number of inversion parameters will not only result in reduction in computational overhead, but can also potentially reduce the ill-posedness of resistivity inverse problems.

We have demonstrated that increasing the number of basis functions, in other words, increasing the number of inversion parameters, from 100 to 300 produced only marginal or no improvement in model resolution. This finding illustrates a potential lossless truncation capability of the POD algorithm that may avoid the estimation of unnecessary inversion parameters. In this regard, further study to determine optimal truncation criterion, either in terms of percentage contribution of singular values or image reconstruction error approach, will be a useful contribution to the advancement of the POD algorithm.

Furthermore, the building of accurate conceptual models, which underpins the generation of the training dataset, is critical to the performance of the POD-constrained inversion algorithm. Nevertheless, the ability of the approach to notice the bimodality in synthetic #2, even though the reconstruction of synthetic #2 was based on a conceptual model of a unimodal plume, illustrates a potential application of the technique to improve our conceptual understanding of hydrogeological systems. Since the initial hypothesis can now be reconceptualized to include bimodal plumes, after which the reconstruction process can then repeated in a similar manner.

Increasing data coverage will not necessarily translate into gains in model resolution without considering optimal array configuration. In fact, it can lead to a net effect of deterioration of model resolution. Specifically, we demonstrated that an increase in the number of data samples exaggerates the aggregate impact of data noise on model resolution. Also, there appears to be an interesting trade-off relationship between the various error parameters appraised, which are data noise, data coverage, and accuracy of *a priori* constraints. The aggregate impact of noise as a result of increased data samples is worsened by inaccurate basis constraints. This observation implies that improving our conceptual understanding of a system, in a bid to improve the accuracy of basis constraints, can presumably enhance the robustness of the POD-algorithm to measurement errors.

This Chapter was originally published in Journal of Hydrology

Oware and Moysey [2014] with doi: 10.1016/j.jhydrol.2014.05.054

CHAPTER FOUR

GEOPHYSICAL EVALUATION OF SOLUTE PLUME SPATIAL MOMENTS USING AN ADAPTIVE POD ALGORITHM FOR ELECTRICAL RESISTIVITY IMAGING

ABSTRACT

We investigate the potential for characterizing spatial moments of subsurface solute plumes from surface-based electrical resistivity images produced within a proper orthogonal decomposition (POD) inversion framework. The existing POD algorithm is improved here to allow for adaptive conditioning of the POD training images on resistivity measurements. The efficacy of the suggested technique is evaluated with two hypothetical transport scenarios: synthetic #1 is based on the case where the target plume and POD training images follow the same (unimodal) plume morphology, whereas a second source location in synthetic #2 makes the target plume bimodal and inconsistent with the POD training images. The resistivity imaging results indicate that the adaptive algorithm efficiently and robustly updates the POD training images to obtain good quality resistivity images of the target plumes, both in the presence of data noise and when conceptual model inaccuracies exist in the training simulations. Spatial moments of the solute plumes recovered from the resistivity images are also favorable, with relative mass recovery errors in the range of 0.6 – 4.4%, center of mass errors in the range of 0.6 – 9.6%, and spatial variance errors in the range of 3.4 – 45% for cases where the voltage

data had 0-10% noise. These results are consistent with or improved upon those reported in the literature. Comparison of the resistivity-based moment estimates to those obtained from direct concentration sampling suggests that for cases with good quality resistivity data (i.e., <3% noise), the imaging results provide more accurate moments until 6-10 multi-level sampling wells are installed. While the specific number of wells will depend on the actual field scenario, we suggest that this finding illustrates the general value of POD-based resistivity imaging techniques for non-invasively estimating the spatial moments of a solute plume.

1. INTRODUCTION

Hydrogeologists often employ statistical moments to describe the morphology of subsurface solute plumes and provide valuable insights to the spatiotemporal evolution of transport processes (e.g., Freyberg, 1986; Goltz and Roberts, 1987, Yeh et al., 2005). Spatial moments play a vital role in numerous hydrological applications such as the design of ground-water quality monitoring networks (e.g., Loaiciga et al., 1992), characterization of flow regimes (e.g., Ye et al., 2005; Yeh et al., 2005; Lazarovitch et al., 2007; Xiong et al., 2011), and the analysis of solute plume behavior (Brewster et al., 1995; Rubin, 2003; Fernàndez-Garcia et al., 2005; de Barros and Nowak, 2010). The two-dimensional spatial moments, $m_{i,j}$, for the image of a solute plume with concentrations $\mathbf{c}(x_k, y_k)$ at locations x_k and y_k can be expressed as:

$$m_{i,j} = \sum_{k}^{NxM} \mathbf{c}(x_k, y_k) x_k^i y_k^j \Delta x \Delta y, \tag{1}$$

where $m_{i,j}$ represents the spatial moment of interest and the overall order of the moment is defined by the sum $i + j$. Here k represents the element index in a discretized representation of the subsurface, Δx and Δy are the dimensions of the pixels, and it is assumed that background concentration variations unrelated to the plume have been removed. The zero-order moment, $m_{0,0}$, quantifies the total mass in the system. The x and y coordinates of the center of mass of the plume can be inferred from the first-order moments ($m_{1,0}$ and $m_{0,1}$):

$$\mu_x = m_{1,0}/m_{0,0},$$

$$\mu_y = m_{0,1}/m_{0,0}.$$

Similarly, the longitudinal and transverse dispersive spreading of the plume can be evaluated from the second-order moments ($m_{2,0}$, $m_{0,2}$, and $m_{1,1}$):

$$\sigma_x = \sqrt{\frac{m_{2,0}}{m_{0,0}} - \left(\frac{m_{1,0}}{m_{0,0}}\right)^2},$$

$$\sigma_y = \sqrt{\frac{m_{0,2}}{m_{0,0}} - \left(\frac{m_{0,1}}{m_{0,0}}\right)^2}.$$

Conventional direct-sampling of concentration approaches (e.g., Everett, 1980; Freyberg, 1986; LeBlanc et al., 1991) are typically applied to gain insight into the spatial extent of subsurface solute plumes. Direct sampling of concentrations, however, is invasive, expensive, and introduces contaminant mobilization risks. In contrast, geophysical methods have the potential to noninvasively estimate spatial moments of conductive solute plumes with low costs and minimal risk.

In a 2-D hypothetical example, for instance, Pidlisecky et al. (2011) formulated a distribution-based parameterization inversion framework from which they successfully characterized spatial moments of plumes from cross-borehole radar tomograms. In a field-scale application, Binley et al. (2002) accurately retrieved spatial moments of fluid flow in the vadose zone using electrical resistivity tomography (ERT). Singha & Gorelick (2005) and Müller et al. (2010) used spatial moments from time-lapse ERT images to investigate transport processes. Hubbard et al. (2001) went further by utilizing spatial moments derived from ERT images to calibrate aquifer flow and transport parameters.

Some challenges regarding the accuracy of moments estimated from geophysical tomograms, such as underestimation of mass and smearing of plumes, have been reported as a result of imaging artifacts (e.g., Singha & Gorelick, 2005; Day-Lewis et al., 2007). To investigate the drawbacks associated with resolving moments from geophysical tomograms, Day-Lewis et al. (2007) derived a semi-analytical moment-resolution matrix. The authors used this tool to conclude that the geophysically recovered plume moments are dependent on the measurement sensitivity, survey geometry, regularization criteria, and measurement errors.

One particularly important cause of tomographic errors has been attributed to limited choices for regularization criteria needed to stabilize the mathematics of the imaging problem (e.g., Oware et al., 2013). Commonly utilized regularization constraints are based on deviations from a reference value or the minimization of the first and second spatial derivatives, which respectively invoke smallness, flatness, and smoothness in the recovered solution (Tikhonov & Arsenin, 1977; Pidliseky et al., 2007). While these constraints are often considered “objective” choices, they may not be optimal for representing how the physics of the underlying process, e.g., groundwater flow and transport, produce spatial property variations, i.e., plume concentrations.

Oware et al. (2013) introduced a Proper Orthogonal Decomposition (POD) constrained inversion strategy to leverage site-specific, physics-based *a priori* information to constrain geophysical inverse problems in a flexible fashion by invoking soft process constraints. The technique applies POD (e.g., Banks et al., 2000; Kunisch and Volkwein, 2003; Rathinam and Petzold, 2004; Pinnau, 2008) to obtain a physics-based POD basis, i.e., set of vectors representing process-relevant spatial patterns, from site-specific Training Images (TI). The basis patterns are subsequently utilized to constrain the inversion procedure. The TIs are generated using Monte Carlo simulations to mimic the perceived physical mechanisms of interest, which in this study are conservative groundwater flow and transport in heterogeneous aquifers.

The POD algorithm is a model order reduction (MOR) technique since it maps a high-order dimensional state-space into a low-order dimensional coefficient-space via optimally selected basis functions. The geophysical optimization then proceeds in the low-order dimensional coefficient-space resulting in the estimation of fewer inversion parameters compared to the original dimensionality of the problem. While MOR techniques are extensively researched in other scientific and engineering disciplines such as applied mathematics (e.g., Li et al., 2009; Yao and Meerbergen, 2013) and image processing (e.g., Milanfer et al., 1981), the technique remains largely under-explored in the field of hydrogeophysics. In contrast to our use of POD as a sparse basis for representing the parameter space, the use of POD in groundwater inverse problems generally tends to focus on improving the computational efficiency of the forward model (e.g., Winton et al., 2011).

In the context of solute plume imaging, available literature related to MOR mainly employs optimal parameterization of the state-space based on statistical moments (e.g., Pidlisecky et al., 2011) or object-based-inversion (OBI) (e.g., Miller et al., 2000; Lane et al. 2004, 2006) that seeks to reduce the number of inversion parameters required to fully describe the target plume, while simultaneously invoking *a priori* constraints regarding the physics or geometry of the target features. In contrast to these approaches POD is a MOR technique that can directly leverage advances in mechanistic modeling in an effort to capture and incorporate realistic, non-parametric, site-specific hydrological process patterns into hydrogeophysical inversion schemes.

A problem with the proposed POD-based inversion scheme, however, was that it lacked the ability to shift basis patterns in space. Hence, the center of mass of the TIs had to be positioned in close proximity to the true center of mass for the plume being imaged. Oware et al. (2013) assumed that the center of mass could be approximated prior to the detailed reconstruction of a resistivity image using methods similar to Pidlisecky et al.'s (2011) distributed parameterization or Fowler and Moysey's (2011) coupled inversion approach, where resistivity data were used to calibrate the effective properties of an analytical transport model. The dependence of the POD approach on this assumption is a major limitation of the algorithm as initially proposed by Oware et al. (2013).

The objective of this paper is twofold. First, we address the limitations of the original POD imaging method to adaptively estimate the solute plume center of mass within the POD-constrained imaging algorithm. We hypothesize that the plume's true center of mass can be evaluated by recursively reconstructing resistivity images as the center of mass of the POD training images is successively updated in each iteration, thereby adaptively conditioning the center of mass to the resistivity data. Second, we evaluate the accuracy of solute plume spatial moments derived from POD-based images using two synthetic transport experiments.

In this paper, we present the proposed adaptive POD-constrained inversion algorithm in section two. Details of the numerical experiment used to test the efficacy of the suggested scheme are then provided in section 3. Results of the investigation including the impact of resistivity measurement errors on the POD-based spatial moments, and comparison to moments estimated by direct sampling from multi-level wells are outlined in section 4. Section 5 summarizes the key conclusions of the study.

2. ADAPTIVE ALGORITHM FOR POD-CONSTRAINED IMAGING

The working details of traditional ERT are extensively documented in the literature (e.g., Kemna et al., 2002). The standard protocol for ERT surveys involves the successive application of electric current (I) to the subsurface via electrodes deployed in the ground. The current flow induces voltages ($\mathbf{V}_{obs}$) dependent on the spatial distribution of electrical resistivity (inverse of electrical conductivity, $\boldsymbol{\sigma}$), which is controlled by the physical properties of the earth (e.g., solute concentrations). The observed voltages are subsequently utilized to reconstruct the electrical conductivity distributions. POD inversion described by Oware et al. (2013) is a variant of Tikhonov regularization that employs a physics-based *a priori* model to constrain the optimization procedure.

The POD inversion represents subsurface conductivities as a linear combination of M basis vectors, i.e.,

$$\boldsymbol{\sigma} = \mathbf{Bc}, \tag{2}$$

where the columns of the set $\mathbf{B} \in \mathbf{R}^{M\ x\ M}$ represent the basis vectors that capture spatial patterns relevant to the imaging problem. The rows of the expansion coefficient $\mathbf{c} \in \mathbf{R}^{M\ x\ 1}$ denote the magnitude of components of $\boldsymbol{\sigma}$ in the basis space (i.e., projected within the POD coordinate system). Implementing Eq.2 within the traditional Tikhonov regularization (Tikhonov & Arsenin, 1977), the objective function for POD-constrained inversion can be defined as:

$$\mathbf{E}(\mathbf{c}) = \mathbf{E}_d + \beta\mathbf{E}_m = \left\|\mathbf{W}_d[\mathbf{V}_{obs} - \boldsymbol{f}_g(\mathbf{Bc})]\right\|_2 + \beta\|\mathbf{W}(\mathbf{Bc} - \mathbf{Bc}_0\|_2$$

$$= \left\|\mathbf{W}_d[\mathbf{V}_{obs} - \boldsymbol{f}_g^*(\mathbf{c})]\right\|_2 + \beta\left\|\widetilde{\mathbf{W}}\,(\mathbf{c} - \mathbf{c}_0\right\|_2. \qquad (3)$$

The $\mathbf{E}_d$ term is the data norm, which measures the fit between observed and modeled data, whereas $\mathbf{E}_m$ is the model norm, which introduces prior information about $\boldsymbol{\sigma}$. The data weighting matrix, $\mathbf{W}_{\boldsymbol{d}}$, is a diagonal matrix containing the inverse of the standard deviations of the measured data along its diagonal. In this study, $\mathbf{W}_{\boldsymbol{d}}$ is formulated according to Pidlisecky et al. (2007). The regularization parameter, β, is utilized to tune the relative importance of data fit versus model regularization. Additionally, $\boldsymbol{f}_g^*(\cdot)$ denotes a transformed resistivity forward model functional that incorporates the reconstruction of $\boldsymbol{\sigma}$ from the POD basis. The regularization operator, $\mathbf{W}$, contains information that enforces spatial criteria (e.g., flatness and continuity) within the reconstructed images. Notice that while the regularization operator, $\mathbf{W}$, acts in the original model space, the composite regularization filter, $\widetilde{\mathbf{W}}$, acts in the transformed coefficient ($\mathbf{c}$) domain and is described in detail later. The reference conductivity model is denoted by $\boldsymbol{\sigma}_0$ or equivalently $\mathbf{c}_0 = \mathbf{B}^T\boldsymbol{\sigma}_0$.

The conceptual algorithm for Oware et al.'s (2013) original POD-constrained inversion is outlined in Figure 4.1. The overall implementation proceeds in four major steps, namely: (i) Monte Carlo simulation of TIs that capture the influence of the target process on state variables, (ii) construction of POD basis (**B**), (iii) optimization of expansion coefficients (**c**), (iv) reconstruction of *in-situ* target profiles (**σ**). Note that if the retrieved model is found to be inconsistent with the assumptions underlying the generation of the training dataset, the initial process hypotheses can be reconceptualized, e.g., based on the imaging results, and the entire data inversion process repeated in the same fashion for improved estimation. The POD approach can therefore also aid in conceptual model development.

In the construction of the POD-bases, the rows of the training dataset, $\mathbf{D} \in \mathbf{R}^{N\ x\ M}$, contain the *N* realizations of the simulated TIs, $\boldsymbol{\sigma}^{TI} \in \mathbf{R}^{1xM}$, obtained by Monte Carlo simulation of relevant flow and transport processes. The POD basis vectors can be approximated from **D** in a least-square minimization manner (e.g., Kunisch and Volkwein, 2003; Pinnau, 2008), or via Singular Value Decomposition (SVD) (e.g., Castleman, 1996). Using SVD, the training dataset can be factorized into its respective left and right singular vectors **U** and **V**, along with their corresponding singular values **Λ**:

$$\mathbf{D} = \mathbf{U}\boldsymbol{\Lambda}\mathbf{V}^T, \tag{4}$$

where $\mathbf{U}\ \in \mathbf{R}^{N\ x\ N},\ \mathbf{V} \in \mathbf{R}^{M\ x\ M}$ and $\boldsymbol{\Lambda} \in \mathbf{R}^{N\ x\ M}$. In practice, the spatial patterns most characteristic of the TIs are captured by the first p basis vectors where $p \ll M$, such that **V** can be truncated without introducing significant reconstruction errors (Oware et al., 2013). The truncation criterion is based on a user-defined threshold of percentage contribution of singular values of the p selected basis vectors with respect to the overall M singular values weight. There are situations, however, where a single basis vector can account for over 99% of the overall variability in the training data. In this case, the above specified truncation criterion will fail to include high-order basis patterns vital to reconstructing details in the geometry of the target plume.

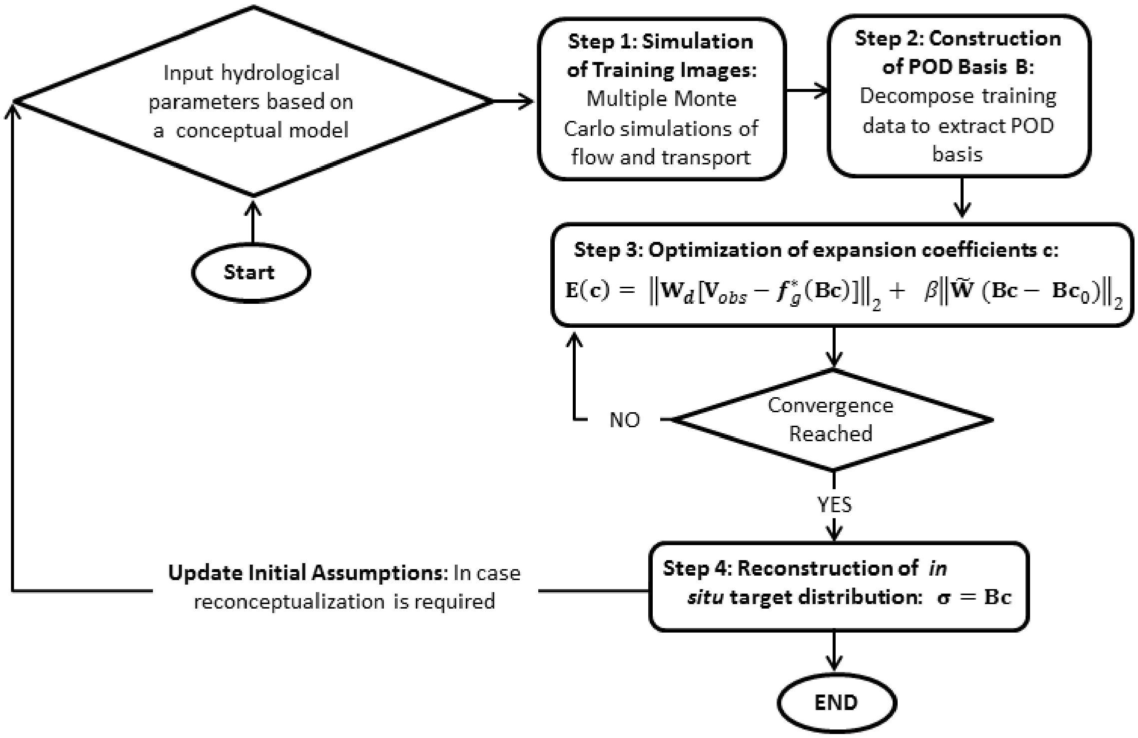

Figure 4.1: Schematic illustration of the conceptual algorithm for the implementation of the POD-constrained inversion.

To address this challenge, we suggest an alternative truncation criterion based on imaging error. In this approach, an arbitrary hypothetical plume model is projected into the coefficient space and then reconstructed based on varying numbers (p) of basis functions. The error of the reconstructed image can then be estimated as a function of p to identify an acceptable truncation. For this exercise, we suggest applying a more complicated hypothetical plume as compared to the TIs used in generating the basis library to avoid truncation of important high-order patterns. Illustrative examples of POD basis functions used in this study are shown in Figure 4.2.

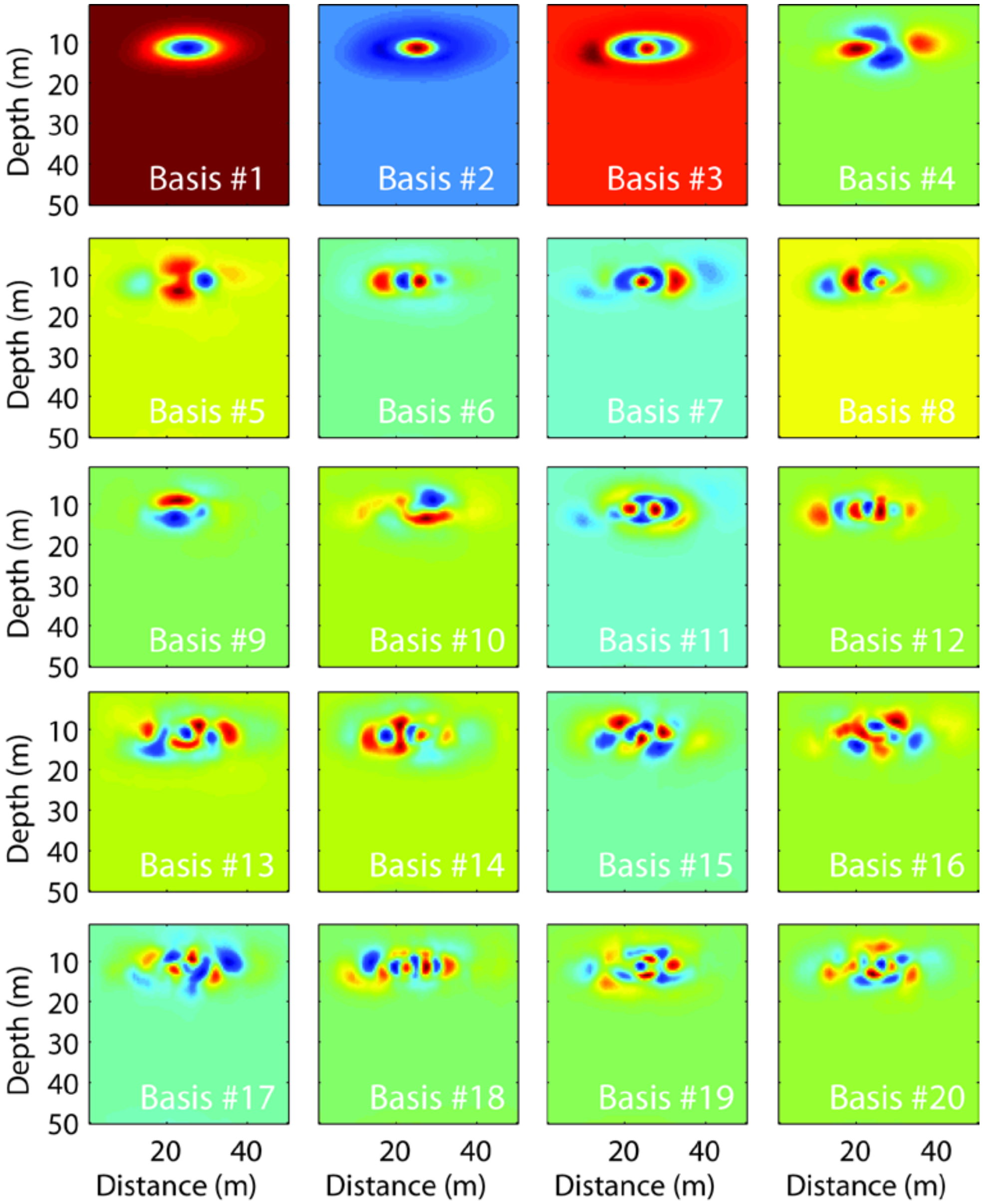

Figure 4.2: Illustrative examples of the first 20 dominant basis patterns extracted from the decomposition of the training images.

The formulation of the regularization filter, **W**, in the Cartesian model space is a combination of difference operators as suggested by Ellis and Oldenburg (1994a):

$$\mathbf{W}^T\mathbf{W} = \mathbf{gx}_2^T\mathbf{gx}_2 + \mathbf{gy}_2^T\mathbf{gy}_2 + \delta\mathbf{M}_w^T\mathbf{M}_w\ ,$$

where $\mathbf{gx}_2$ and $\mathbf{gy}_2$ represent the discretized lateral and vertical second derivative spatial filters, respectively, which penalize for roughness in the spatial distribution of the model parameters. $\mathbf{M}_w$ denotes the model weights matrix, which penalizes against the propagation of singular errors near the electrodes (e.g., Fox, 1979; Dey and Morrison, 1979b). The smallness factor, δ, is a fitting parameter that is utilized to tune the relative importance of these penalties. The filter $\mathbf{W}$ is projected into the coefficient space as

$$\widetilde{\mathbf{W}}^T\widetilde{\mathbf{W}} = \mathbf{B}^T\mathbf{W}^T\mathbf{W}\mathbf{B} + \boldsymbol{\lambda}\mathbf{W}_{sv}, \tag{5}$$

while introducing additional constraints $\mathbf{W}_{sv}$ based on the singular values of the training dataset **D**. The singular values represents the variance (or importance) of the basis vectors in the POD coordinate system for capturing the training data, therefore, $\mathbf{W}_{sv}$ imposes an *a priori* structural constraint on the optimization procedure that biases the images toward the TIs. Another fitting parameter, $\boldsymbol{\lambda}$, is applied to balance out the relative importance of the conventional regularization constraints versus the TIs.

Following the generation of site-specific, non-parametric POD bases and the optimization of the transform coefficients, **c**, the *in-situ* electrical conductivity distributions can be approximated via Eq.2. (step 4 in Figure 4.1).

The POD technique as described above is unable to shift the location of the basis vectors toward the location of the true plume during the optimization procedure. The method therefore requires that the TIs can be located in the vicinity of the true plume prior to initiating image reconstruction. To overcome this limitation, we propose a simple strategy to adaptively estimate the center of mass of the solute plume within the POD inversion scheme from surface-based resistivity measurements.

The adaptive POD algorithm is heuristically illustrated in Figure 4.3. First, an initial estimate of the center of mass of the true plume is used to position the training images (or equivalently the POD basis); note that this location must be within the region of sensitivity of the resistivity measurements though it need not be in the immediate vicinity of the actual plume being imaged. The standard POD algorithm (Figure 4.1) is then used to obtain an estimate of the resistivity image. After the data inversion, the center of mass of the retrieved tomogram is estimated and used to reposition the Tis (or POD basis vectors) for the next iteration. This process is repeated until convergence is reached, where we define the convergence criterion based on a data-fit tolerance limit.

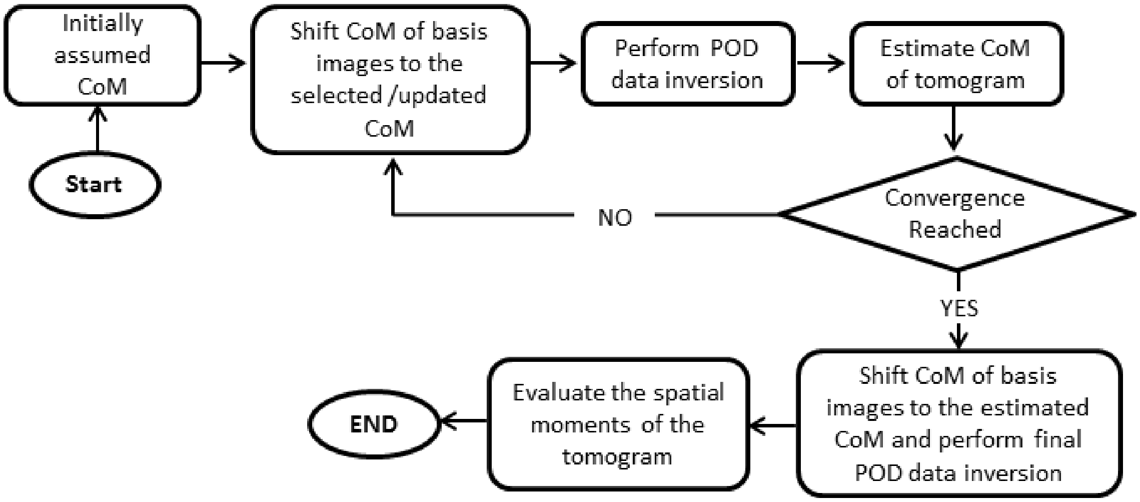

Figure 4.3: Conceptual algorithm to estimate the spatial moments of a targeted subsurface distribution from resistivity measurements. CoM refers to center of mass.

3. METHODS

Two hypothetical transport experiments were applied to test the proposed strategy and evaluate the accuracy of the resulting plume moments. A schematic illustration of the experimental setup is provided in Figure 4.4. The simulations resulted in two synthetic targets, synthetic #1 and synthetic #2 (Figures 4.5a and 4.6a), Both examples assume conservative solute transport through a two dimensional, heterogeneous cross section of the subsurface in response to a horizontally applied uniform hydraulic gradient. The top and bottom boundaries of the system represent zero flux conditions. Resistivity surveys are collected using electrodes placed near the top of the model domain, i.e., at the ground surface. The difference between the two scenarios is that synthetic #1 contains a single source for the solute, thereby producing a unimodal plume, whereas synthetic #2 contains an additional solute source, leading to a bimodal solute plume. Archie's law (Archie, 1942) was used for both the forward and inverse transformation of concentration to electrical conductivity. We therefore do not explicitly account for petrophysical scaling effects as discussed in previous work by Moysey and Knight (2004), Moysey et al. (2004), and Singha and Moysey (2006). Refer to Oware et al. (2013) for further specific details of the hydrological simulations for the test examples and the training images, and also the details of the resistivity survey and the ERI inversions.

The conceptual algorithm for the estimation of the plume center of mass (Figure 4.3) requires the selection of an initial location for the POD basis vectors. To explore the impact on the quantification of the true center of mass as a result of the anisotropic nature of resistivity sensitivities (e.g., Keller and Frischknecht, 1966), three scenarios were investigated where the initial position was laterally, vertically, or diagonally shifted relative to the true center of mass.

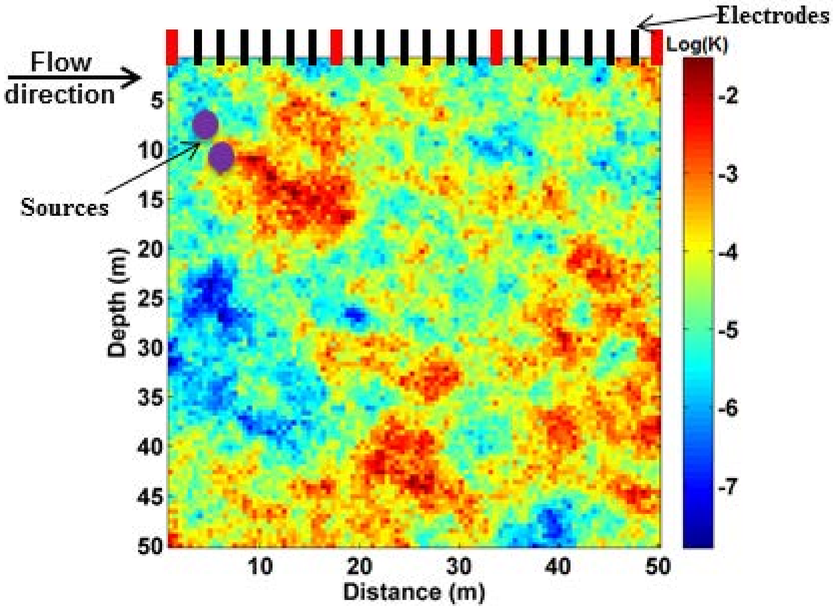

Figure 4.4: Schematic illustration of the experimental setup of the 2-D flow and transport in a random hydraulic conductivity field (image color scale denotes the value of the log of K). The design of the resistivity surveys illustrated by the electrodes along the ground (top) surface; while the red electrodes served as both current and potential electrodes, the black electrodes were used exclusively as potential electrodes leading to a total of 120 resistance measurements in each survey.

To control the positioning error, the initial center of mass was shifted in proportion to the true plume's width as described by the lateral and vertical second spatial moments (e.g., Freyberg, 1986; Goltz & Roberts, 1987). While the lateral perturbation of the x-coordinate was 16 m, the y-coordinate was vertically shifted by 9 m. For instance, for a true center of mass of (x_0,y_0), the vertical, lateral, and diagonal positioning errors were (x_0,y_0+9), (x_0+16,y_0), (x_0+16,y_0+9), respectively. To provide a constant basis for comparing all the results, these positioning errors were kept constant for all the data inversions.

Furthermore, in an effort to explore how data uncertainties affect the predictive power of the center of mass, we assumed random Gaussian errors with standard deviations proportional to the resistivity signals, according to the following noise model:

$$\mathbf{d}_{noise} = \mathbf{d}_{no\_noise} + n_{per} \cdot \mathbf{d}_{no_{noise}} \cdot \mathrm{N}(0,1), \tag{6}$$

where $\mathbf{d}_{noise}$ and $\mathbf{d}_{no\_noise}$ represent the corrupted and noise-free data, respectively. n_{per} denotes the proportion of the resistivity signal to be added as noise. In this study, we investigated scenarios where n_{per} was set to 0, 0.03 (3%), and 0.1 (10%). $\mathrm{N}(0,1)$ signifies a random normal distribution with zero mean and standard deviation of one. While assuming simple Gaussian noise model may be adequate for our demonstrations here, empirical errors in applications can be estimated based on reciprocal measurements (interchanging injection and receiver electrodes) as presented by LaBreque et al. (1996). To evaluate the influence of noise on the center of mass estimation, the data inversion was performed for 100 datasets generated from the excitation of $\mathbf{d}_{no\_noise}$ with 100 realizations of Gaussian noise.

4. RESUTLS AND DISCUSSION

4.1. Estimation of Electrical Conductivity Images

Estimated conductivity images of the plume obtained for each iteration of the adaptive POD inversion are shown in Figures 4.5 and 4.6 for synthetic #1 and synthetic #2, respectively; these results represent the case where the POD TIs were initially laterally displaced from the true center of mass by 16m. Note that the assumed center of mass used to position the POD TIs is shown as white star in these images, which moved progressively toward the true plume center of mass (shown as white cross) as the inversion proceeds. Results are presented for cases where 0, 3, and 10% errors were added to the voltage measurements prior to the inversion.

As the adaptive POD inversion progresses for synthetic #1, the images in Figure 4.5 consistently improve as the TIs are shifted toward the true location of the plume. The influence of noise is qualitatively apparent in the images as over fitting of the data errors causes spurious non-zero conductivities to appear in the regions away from the true plume, which is spatially compact. This observation is quantitatively supported by a consistent increase in the root mean square error (RMSE) of the estimated plume concentration with increasing noise (Table 4.1). It is also apparent, however, that noisy data requires more iterations for the algorithm to converge toward an acceptable image of the true plume.

Table 4.1: True and calculated spatial moments for the final concentration estimates obtained for scenarios with 0, 3, and 10 % signal noise in the resistivity data.

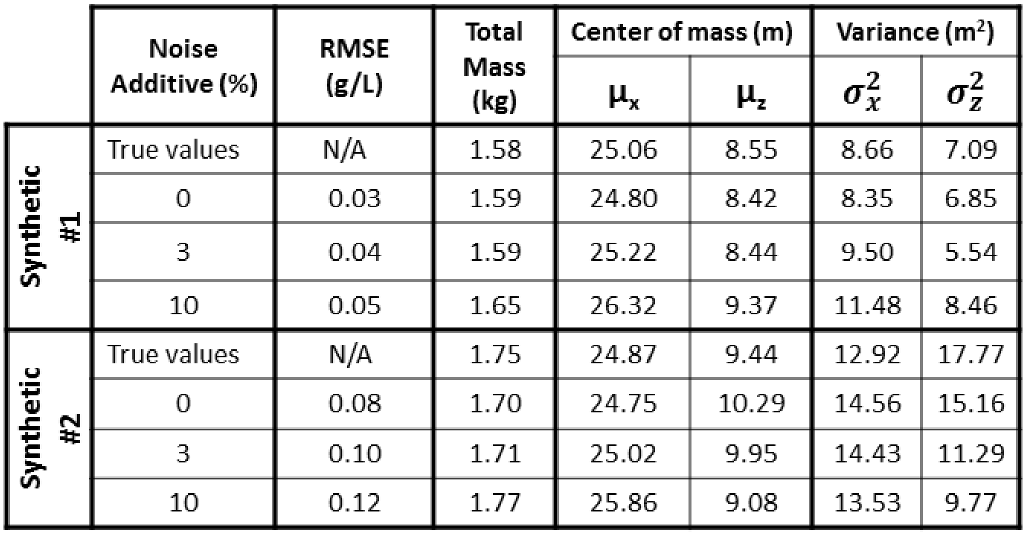

	Noise Additive (%)	RMSE (g/L)	Total Mass (kg)	Center of mass (m)		Variance (m^2)	
				μ_x	μ_z	σ_x^2	σ_z^2
Synthetic #1	True values	N/A	1.58	25.06	8.55	8.66	7.09
	0	0.03	1.59	24.80	8.42	8.35	6.85
	3	0.04	1.59	25.22	8.44	9.50	5.54
	10	0.05	1.65	26.32	9.37	11.48	8.46
Synthetic #2	True values	N/A	1.75	24.87	9.44	12.92	17.77
	0	0.08	1.70	24.75	10.29	14.56	15.16
	3	0.10	1.71	25.02	9.95	14.43	11.29
	10	0.12	1.77	25.86	9.08	13.53	9.77

The situation is somewhat different for synthetic #2, where the estimated images significantly degrade in early iterations before finally converging toward an acceptable solution (Figures 4.6b-j). In this case, the adaptive POD algorithm also requires substantially more iterations to converge for the zero noise case compared to the cases with noise added (Figure 4.6), though the RMSE of the final concentration estimates is ultimately superior for the noise-free case (Table 4.1). The difference in behavior compared to synthetic #1 is due to the fact that the model used to generate the POD TIs, i.e., a unimodal plume with a single source zone, is inconsistent with the actual solute plume being imaged in synthetic #2, i.e., a bimodal plume generated by releases from two distinct source zones. The inconsistency between the *a priori* conceptual model of the system built into the POD basis versus the resistivity measurements that are representative of the actual plume makes it more difficult for the algorithm to efficiently converge toward an acceptable solution. The data noise stabilizes the inversion, but at the same time causes a loss of resolution in the final estimated images.

The results in Figures 4.5 and 4.6 represent the case where the POD TIs were shifted laterally away from the true center of mass of the plume. In Figure 4.7 we evaluate the sensitivity of the adaptive inversion to the direction in which the POD TIs are initially shifted relative to the true plume center of mass (i.e., lateral, vertical, or diagonal). After each tomographic update the refined location of the TIs approaches the true center of mass of the plume, regardless of the direction in which the TIs were originally perturbed (Figure 4.7). This continuous improvement reflects improved utilization of the resistivity data within the inversion to incorporate information about the true plume while decreasing the dependence on the assumed *a priori* transport model. This observation is consistent with the underlying hypothesis of this study.

It is notable that the location of the training images converged to the same position regardless of the initial displacement direction for the TIs. This observation suggests that the adaptive POD algorithm is insensitive to errors in TI positioning (though TIs must be located within a region of sensitivity to the resistivity measurements). In contrast, it is also apparent that as noise is added to the measurements, the converged location of the TIs relative to the true center of mass deteriorates. This observation suggests that the inversion approach is sensitive to data noise.

To investigate the influence of data noise on the adaptive updating of the TI positions we generated 100 realizations of Gaussian noise to corrupt the voltage measurements and subsequently performed an independent adaptive POD inversion for each corrupted data set. Figure 4.8 shows the mean and standard deviation for the final converged location of the TIs performed with the set of 100 noisy datasets. As the data noise increases, there are two clear impacts on how the TI positions are updated in the adaptive algorithm: (1) on average the position of the TIs converges farther away from the true center of mass of the plume, i.e., there is greater positioning error for the final image reconstruction step in the adaptive algorithm; and (2) there is substantially greater spread in the final converged position of the TIs for the cases with higher data errors. Both of these results suggest that the resistivity data contain less information to constrain the adaptive algorithm as the noise level increases, which is consistent with the degradation of the plume concentration estimates indicated by the RMSE values in Table 1 and the general loss of performance of tomographic imaging techniques with noisy data.

The final positioning errors appear to be minimized when starting the TIs with a vertical displacement relative to the true plume compared to lateral and diagonal shifts for both the 3 and 10% noise cases. This observation, however, may be related to the specifics of the morphology and position of the true plume relative to the sensitivity pattern of the resistivity survey or the fact that the TIs were shifted proportionally to the concentration plume moments, thus the original TI displacement was effectively smaller in the vertical than the lateral or diagonal directions. Of greater concern, however, is an apparent systematic bias in the final position of the training images relative to the true plume regardless of how the TIs are initially perturbed. Given that the training images capture patterns associated with the *a priori* model of transport, this bias could also be related to an inconsistency between the morphology of the TIs and the true plume. The potential significance of the bias is therefore best assessed by directly comparing the spatial moments of the true and estimated concentration plumes.

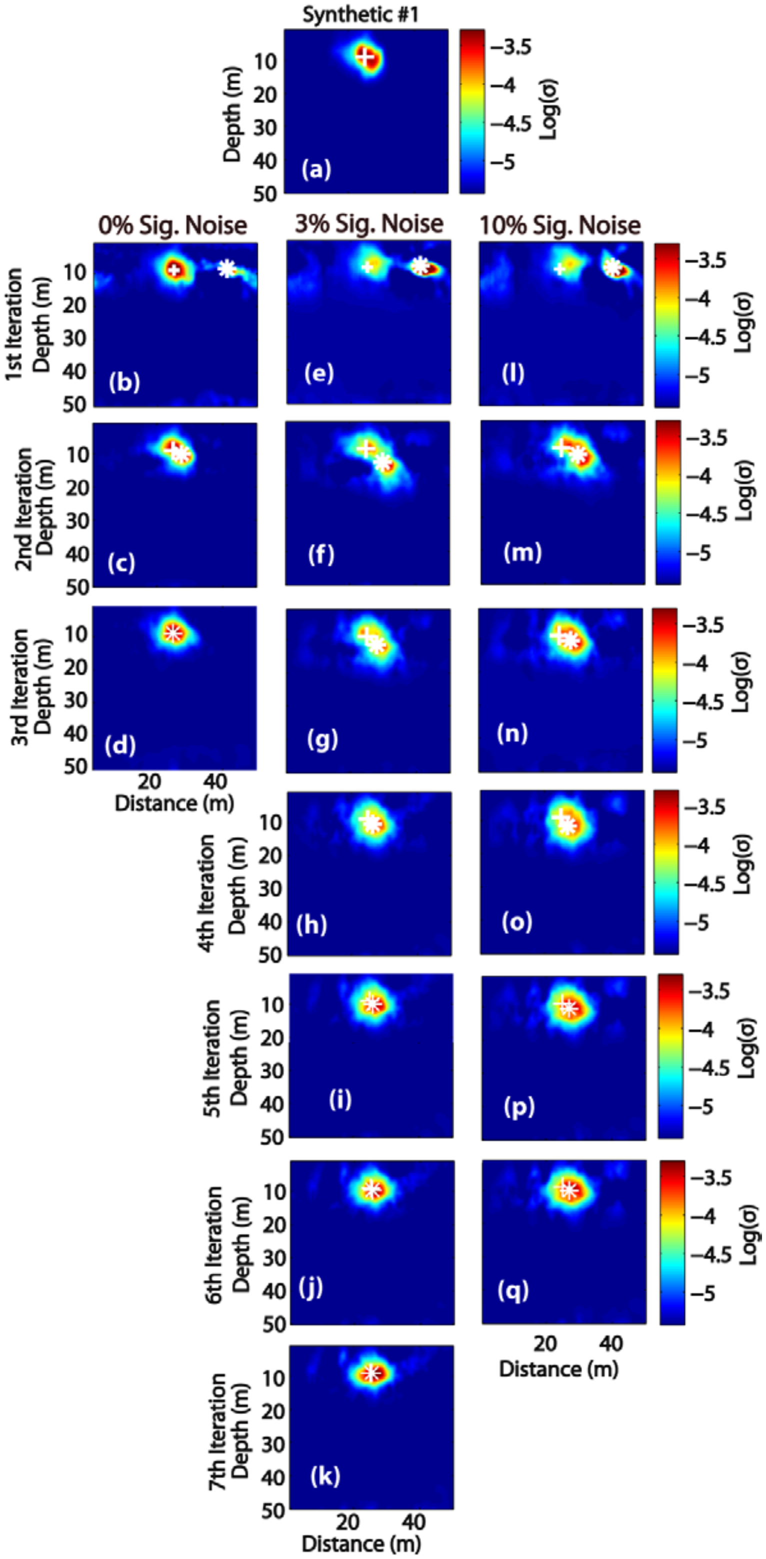
Synthetic #1
Depth (m)
10
20
30
40
50
(a)
−3.5
−4
−4.5
−5
Log(σ)
0% Sig. Noise
3% Sig. Noise
10% Sig. Noise
1st Iteration
2nd Iteration
3rd Iteration
4th Iteration
5th Iteration
6th Iteration
7th Iteration
(b)
(c)
(d)
(e)
(f)
(g)
(h)
(i)
(j)
(k)
(l)
(m)
(n)
(o)
(p)
(q)
20
40
Distance (m)

Figure 4.5: Log of electrical conductivity tomograms demonstrating the iterative reconstructions to estimate center of mass from resistivity measurements for the case of lateral shift of the true center of mass. Synthetic #1 (a). Tomograms showing successive reconstructions from the first to the converged iterations for: 0 % data noise (b-d, column1), 3 % noise (e-k, column 2) and, 10 % noise perturbation (i-q, column 3). The white **+** in each image denotes the position of the center of mass of the true plume, whereas the white * indicates the location of the center of mass of the training dataset for that iteration. Note, it seems the location of the white * gets closer to the white + with each update, in most cases.

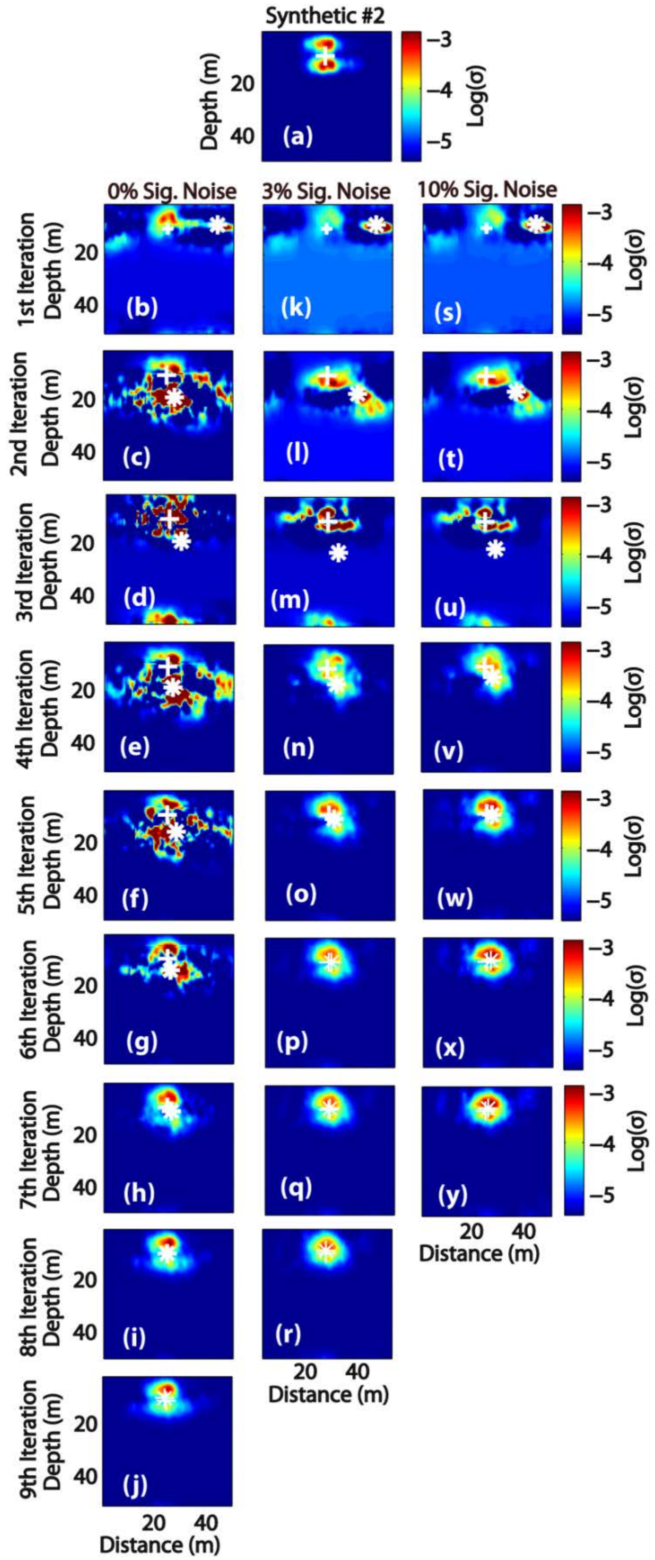
Synthetic #2
Depth (m)
20
40
(a)
−3
−4
−5
Log(σ)
0% Sig. Noise
3% Sig. Noise
10% Sig. Noise
1st Iteration
2nd Iteration
3rd Iteration
4th Iteration
5th Iteration
6th Iteration
7th Iteration
8th Iteration
9th Iteration
(b)
(c)
(d)
(e)
(f)
(g)
(h)
(i)
(j)
(k)
(l)
(m)
(n)
(o)
(p)
(q)
(r)
(s)
(t)
(u)
(v)
(w)
(x)
(y)
20
40
Distance (m)

Figure 4.6: Log of electrical conductivity tomograms demonstrating the iterative reconstructions to estimate center of mass from resistivity measurements, for the example of lateral positioning error. Synthetic #2 (a). Tomograms showing successive reconstructions from the first to the converged iterations for: 0 % data noise (b-j, column 1), 3 % noise (k-r, column 2) and, 10% noise perturbation (s-y, column 3). The white **+** in each image denotes the position of the center of mass of the true plume, whereas the white * indicates the location of the center of mass of the training dataset for that iteration. Note, it appears location of the white * gets closer to the white + with each update, in most cases.

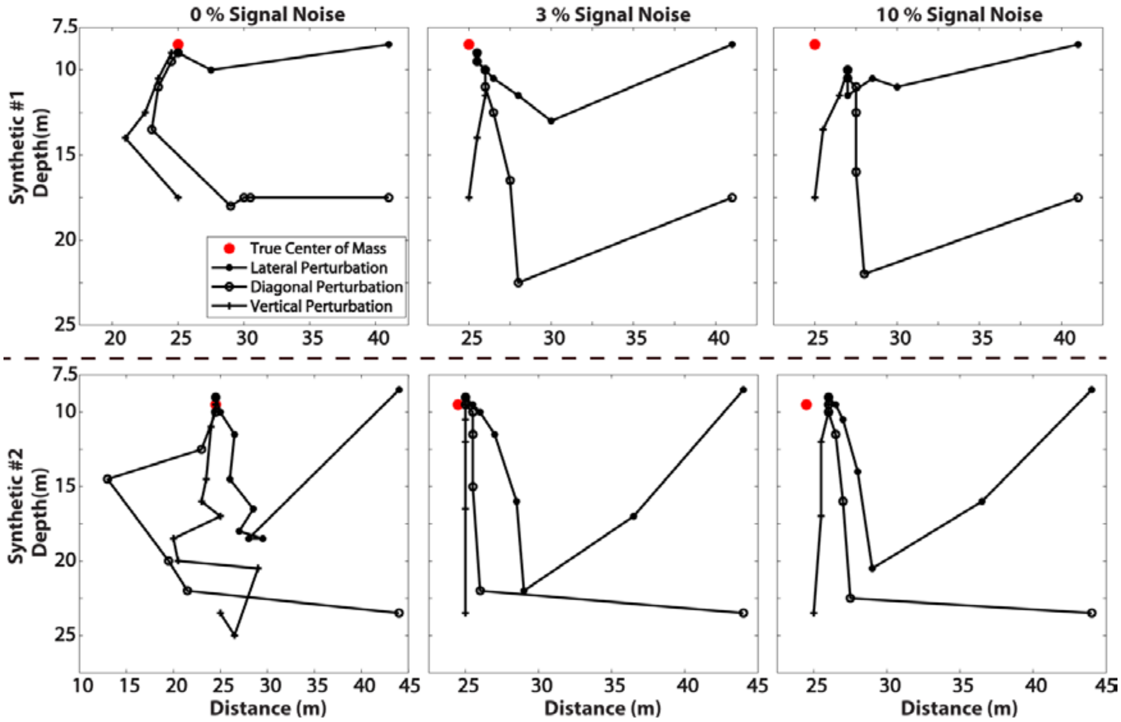

Figure 4.7: Plots showing the update paths for the position of the POD training images: synthetic #1 (row 1), synthetic #2 (row 2). Red circles signify true CoM, black filled circles represent initial lateral shifts in the training image positions, whereas black open circles indicate diagonal shifts and plus symbols denote vertical shifts. Columns 1-3 represent 0, 3, and 10 % signal noise additives, respectively. Observe that for each noise case studied, the estimation of the center of mass from all the perturbed directions, converged at a unique location.

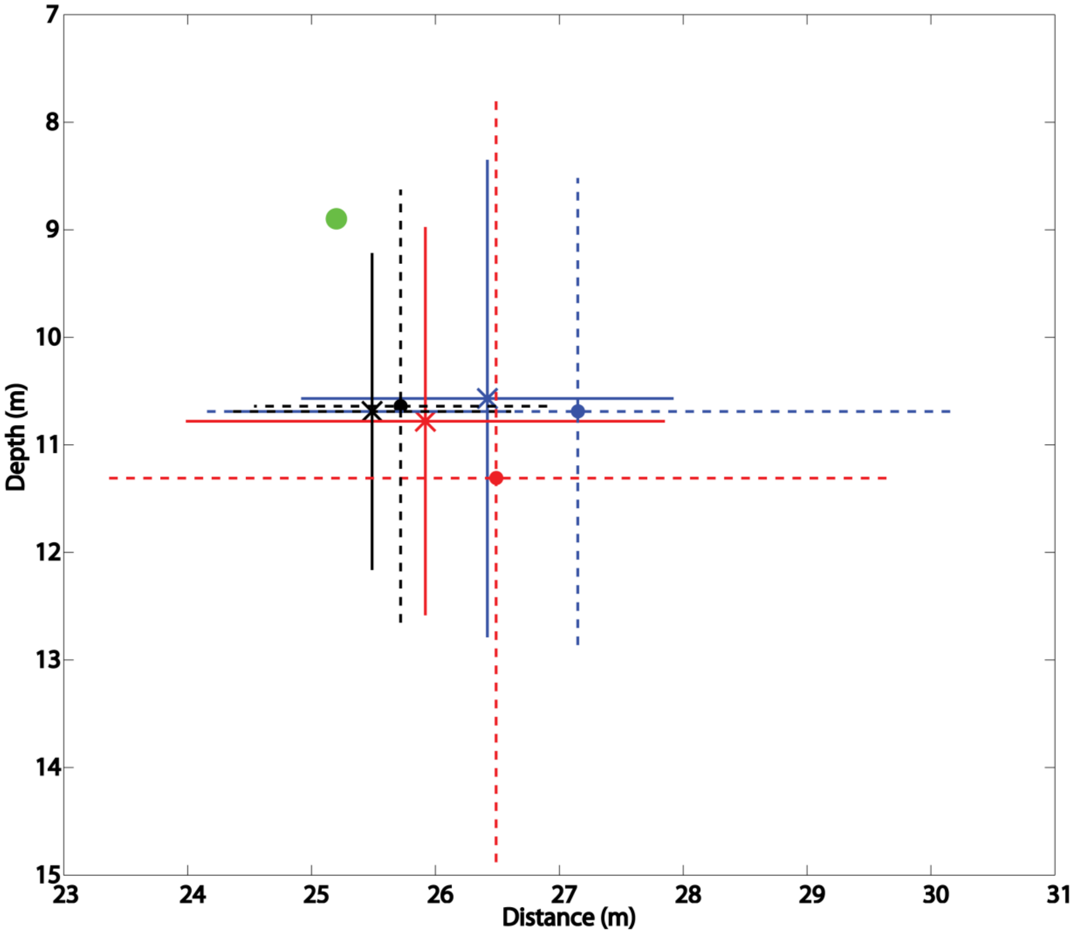

Figure 4.8: Plots of the means and standard deviations of center of mass estimates based on 100 realizations of Gaussian noise additives (Eq.6). The green circle represents the true center of mass; the blue, red, and black denote the lateral, diagonal, and vertical positioning errors, respectively. The cross and the thick lines represent the final mean position of the realizations and one standard deviation for the 3% signal noise perturbations, whereas the circles and the broken lines mark the mean and standard deviation for the 10% signal noise case. The horizontal and vertical lines denote the lateral and vertical standard deviations.

4.2. Quantification of Plume Spatial Moments

As mentioned earlier, the electrical conductivity images were back transformed to concentrations using the same equation applied in the forward transformation from concentration to conductivity when generating the test data. It is also important to note that inherent errors as a result of forward and inverse transformations between electrical conductivities and concentrations, encountered in practical applications, were not accounted for in the results presented here. The accuracies of the zeroth, first, and second spatial moments of the concentration plumes were then estimated from the images using Eq.1. Given that differences in where the final positions of TIs converged in the preceding noise analysis were not significant, we report here only the results for the single realization of data noise associated with the images produced in Figures 4.5 and 4.6.

The spatial moments estimated from the plume images generally degrade with increasing data noise, though all results are reasonably similar to the moments obtained directly from the true plume (Table 4.1). For the case of synthetic #1, the total mass (zeroth moment) was over-estimated by 0.6, 0.6, and 4.4% for the 0, 3, and 10% data errors, respectively. Relative errors in the estimated center of mass (first moment) for the 0, 3, and 10% data uncertainty cases were -1.0, 0.6, and 5.0% for the lateral position and -1.5, -1.3, and -9.6% for the vertical position. Relative errors in the estimated plume size (second moment) for the 0, 3, and 10% data errors were -3.5, 9.7, and 32.6% (lateral variance) and -3.4, -21.9, and 19.3% (vertical variance). These results indicate that estimates of the total solute mass and location of the plume are relatively robust to noise, though the overall size of the plume is more difficult to constrain accurately. In the case of synthetic #2, the estimation accuracy of the spatial moments also generally degraded with increasing data noise (Table 4.1), though the errors were slightly larger and patterns not always clear. For example, the relative error in the estimated center of mass in the lateral direction was -0.5, 0.6 and 4.0 for the 0, 3, and 10% data noise cases, which is consistent with what was observed for synthetic #1. The center of mass in the vertical direction, however, has a substantially higher relative error (9%) for the 0% data noise case than the 3 and 10% data noise cases with relative errors of -5.4 and -3.8%, respectively. Similarly, the lateral and vertical plume variance errors were 12.7, 11.7, and 3.3% (lateral variance) and -14.7, -36.5, and -45.0% (vertical variance), for the 0, 3, and 10% data uncertainties, respectively. These inconsistencies compared to case #1 are associated with the fact that the TIs used to generate the POD basis are conceptually inaccurate for representing the bimodal plume of synthetic #2, as was pointed out early in the context of the reconstruction of Figure 4.6. A close inspection of Figures 3.6j, 3.6r, and 3.6y, for example, reveal that the bottom portion of the bimodal plume (i.e., the second mode) was not fully reconstructed, which explains the relatively high errors in the quantified vertical plume variances for synthetic #2. Regardless of these observations, the overall magnitude of the observed moment errors is relatively modest given that the estimates are obtained using a non-invasive imaging technique.

We emphasize that the laterally central locations of the target plumes were deliberately chosen for maximum resistivity sensitivity. Therefore, we anticipate the resolution of the lateral center of mass to degrade as the target plume is shifted toward the lateral terminals within the domain as pointed out by Day-Lewis et al. (2007).

The literature suggests that the accuracy of the spatial moments estimated using the adaptive POD algorithm in this paper is generally consistent with or slightly better than past experiences achieved with geophysical tomography. Pidlisecky et al. (2011), for example, found percentage mass recovery errors in the range of 0 to -12%, center of mass errors in the range of 0 to 30% (lateral) and 2.7 to 7.5% (vertical), and spatial variance calibration errors of -10 to -80 % (lateral) and -40 to -70% (vertical), though their experiment was a 2D synthetic study of cross-borehole ground-penetrating radar and therefore has substantially different resolution characteristics from the surface based resistivity surveys used in this paper. While direct comparisons across studies with different survey geometries, transport processes, and imaging methods are difficult, the value of the resistivity-based spatial moments estimated in this study can be directly compared to the moments estimated from direct sampling of the solute concentrations.

We simulate direct sampling of the solute plume in Synthetic #1 by placing synthetic boreholes at discrete locations along the cross-section, where for convenience we assume that the entire depth profile of concentration is sampled. It is clear from Figure 4.9 that the estimation accuracy of plume moments from direct sampling is dependent on sampling coverage and the specific locations of the boreholes relative to the true plume.

The moments estimated by direct sampling approach the true plume moments as the number of boreholes increases, stabilizing when approximately 12 boreholes are present or, equivalently, 0.12% of the image has been sampled. The estimate of the vertical center of mass is an exception which appears to retain a slight bias for the limited number of wells shown.

Using Figure 4.9 to compare the center of mass estimates obtained from the resistivity surveys with no and 3% noise to those obtained by direct sampling indicates that the geophysically-based moments are more reliable than those obtained by direct sampling until at least 6-10 wells have been installed. Direct sampling almost always outperforms the resistivity surveys with 10% data noise, however, which demonstrates that the quality of the resistivity data is an important factor in determining its overall value. Similar conclusions can be made for the quality of estimates of the plume size (second moment) and mass (not shown). While the particulars of this comparison are dependent on the details of the specific situation studied, we suggest that these results do support the conclusion that POD-constrained resistivity images provide a promising alternative to extensive direct sampling for reasonably accurate estimation of the spatial moments of solute plumes.

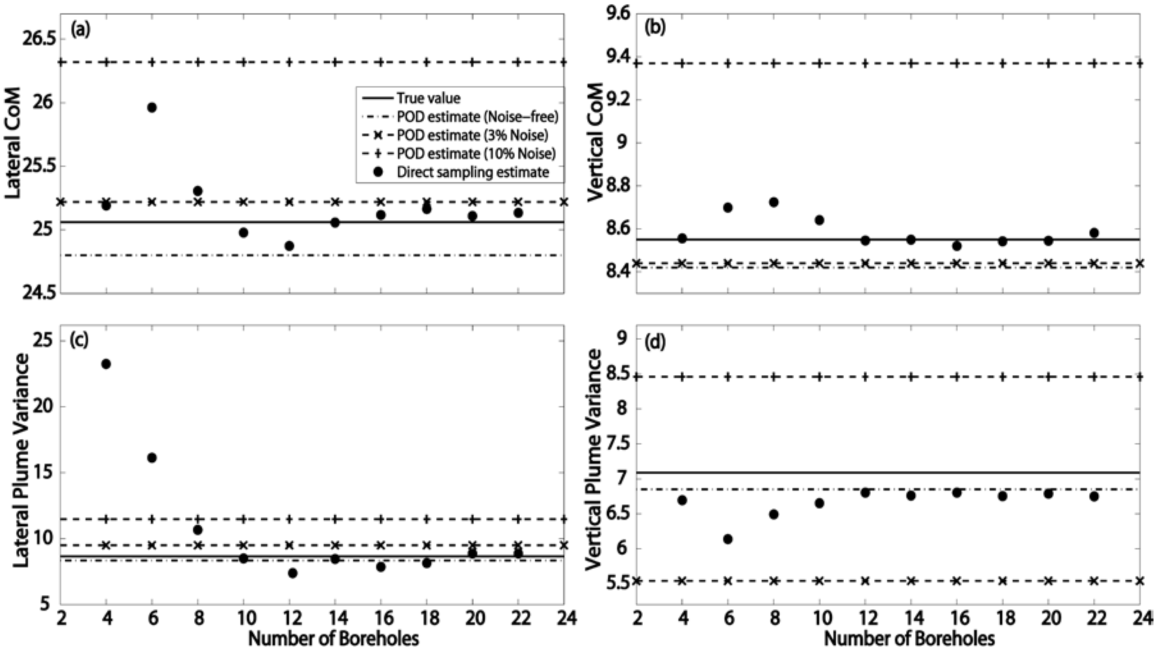

Figure 4.9: Plots comparing the plume spatial moments estimated from resistivity imaging versus direct sampling approaches; upper imagines show results for the center of mass estimated in the lateral (a) and vertical (b) direction, whereas the lower images show results for the plume size in the lateral (c) and vertical (d) directions.

5. CONCLUSIONS

An adaptive POD-based ERT strategy for inferring the spatial moments of subsurface solute plumes was presented. The proposed approach extends the POD inversion strategy introduced by Oware et al. (2013) to iteratively update the spatial location of the POD training images (TIs) (or equivalently the POD basis functions). The algorithm recursively refines the position of the TIs until their position is conditioned on the observed resistivity data. The approach was tested using two hypothetical transport scenarios: synthetic #1, which consists of a unimodal plume that is consistent with the transport model used to produce the POD TIs, and synthetic #2, where the target plume has two source locations that result in a bimodal plume that is inconsistent with the POD TIs.

The adaptive algorithm converged by shifting the TIs to a common region on the domain near the true plume regardless of TI starting position. Although the mean final position of the TIs inverted with 100 different realizations of data noise converged farther away from the center of mass of the true plume as the noise level of the resistivity data was increased, Oware et al. (2013) demonstrated that the TIs did not have to be precisely positioned at the center of mass of the true plume for the POD strategy to be successful. In all cases the final resistivity images provided reasonably accurate representations of the solute plume regardless of issues associated with data noise, the initial TI positioning, or conceptual inconsistencies between the target plume and simulations used to generate the TIs.

Estimates for the spatial moments of the plume based on the proposed imaging strategy were compared to those retrieved from the direct sampling of concentration values. Overall, the total mass and center of mass of the plumes could be accurately quantified by the resistivity results, but the spatial spread of the plume was more difficult to constrain. The estimation accuracy of the moments was found to deteriorate as the noise in the resistivity data increases. Spatial moment evaluations for synthetic #1 are better than the estimates for synthetic #2 due to the inaccurate basis functions applied to constrain the reconstruction of synthetic #2. We also found, however, that the data noise stabilized the inversion process in the case of synthetic #2. For low noise cases (i.e., the 0 and 3% noise cases in this study), the moments estimated from the resistivity images were found to outperform estimates based on direct concentration sampling until 6-10 multi-level sampling wells were installed. Although this particular number of wells is specific to our example, installing any number of multi-port sampling wells in field applications is not trivial given the time, labor, and cost involved in installing boreholes.

The POD algorithm appears particularly appealing due to its MOR capabilities. For instance, in this study, we achieved 97% truncation in the dimensionality of the original problem (i.e., 300 coefficients were estimated to reconstruct an image with 10,000 pixels). Reducing the number of parameters in an inverse problem may result in reductions in computational overhead and a possible improvement in the ill-posedness of the problem.

While our study illustrates a successful application of the adaptive POD-based imaging technique, there are a variety of issues that should be noted. First, the approach will not overcome fundamental sensitivity limitations of resistivity data. For example, if the training images are initially located beyond the influence of the resistivity data, then it will not be possible to shift their locations toward the location of the plume using our framework. Second, the POD basis is limited to capturing patterns representative of the conceptual model used to generate the TIs. Additional research is required to evaluate how this problem might be overcome using adaptive training data, supplementing the POD basis with additional patterns, or using geostatistical tools to capture additional spatial variability. Finally, we have not evaluated how the POD imaging technique or the estimated spatial moments of a plume may be affected by fluctuations in the background resistivity of the aquifer caused by geologic variability or associated uncertainties in the petrophysical relationship between concentration and bulk resistivity.

Despite these limitations, we conclude from this synthetic study that POD-based resistivity imaging provides a viable means for the inference of spatial moments of solute plumes in a noninvasive and cost-effective manner. We look forward to future efforts to undertake field-scale studies to evaluate the generalizability of our numerical findings to real-world settings.

REFERENCES

Archie, G.E., 1942. The electrical resistivity log as an aid in determining some reservoir Characteristics. Trans. Am. Inst. Min. Metall. Pet. Eng., 146, 54–62.

Banks, H.T., Joyner, M.L., Wincheski, B., Winfree W.P., 2000. Nondestructive evaluation using a reduced-order computational methodology. Inverse Problems, 16, 929-945.

Binley, A., Cassiani, G., Middleton, R., Winship, P., 2002. Vadose zone flow model parameterisation using cross-borehole radar and resistivity imaging. J. Hydrol., 267, 147–159.

Brewster, M. I., Annan, A. P., Greenhouse, J. P., Kueper, B .H., Olhoeft, G. R., Redman, J. D., Sander, K. A., 1995. Observed migration of a controlled DNAPL release by geophysical methods. Groundwater vol 33, No. 6, pp 977-987.

Castleman, K. R., 1996. Digital image processing. Prentice Hall, Inc., Upper Saddle River, NJ.

Day-Lewis, F.D., Chen, Y., Singha, K., 2007. Moment inference from tomograms. Geophys. Res. Lett., 34, doi:10.1029/2007GL031621.

de Barros, F. P. J., Nowak, W., 2010. On the link between contaminant source release conditions and plume prediction uncertainty. Journal of Contaminant Hydrology, 116, 24-34. doi:10.1016/j.jconhyd.2010.05.004.

Dey. A., Morrison, H. F., 1979. Resistivity modeling for arbitrarily shaped two-dimensional structures. Geophysical Prospecting, vol 27, No 1, pp 106-136, doi: 10.1111/j.1365-478.1979.tb00961.x.

Ellis, R. G., Oldenburg, D. W., 1994a. Applied geophysical inversion Geophys. J. Int. 116 5–11

Everett, L. G., 1980. Groundwater monitoring. General electric company, Shenectady, N.Y.

Ferna`ndez-Garcia, D., Rajaram, H., Illangasekare, T. H., 2005. Assessment of the predictive capabilities of stochastic theories in a three-dimensional laboratory test aquifer: Effective hydraulic conductivity and temporal moments of breakthrough curves. Water Resour. Res., 41, W04002, doi:10.1029/2004WR003523.

Fox, L., 1979. Finite differences and singularities in elliptic problems: A survey of numerical methods for partial differential equations.Oxford Univ. Press, 43-68.

Fowler, D.E., Moysey, S.M.J., 2011. Estimation of aquifer transport parameters from resistivity monitoring data within a coupled inversion framework,. Journal of Hydrology, 409, 545-554, doi:10.1016/j.jhydrol.2011.08.063.

Freyberg, D.L., 1986. A natural gradient experiment on solute transport in a sand aquifer: 2. Spatial moments and the advection and dispersion of nonreactive tracers. Water Resources Research, 22(13), 2031-2046, doi:10.1029/WR022i013p02031.

Goltz, M.N., Roberts, P.V., 1987. Using the method of moments to analyze three-dimensional diffusion-limited solute transport from temporal and spatial perspectives. Water Resour. Res., 23, 1575–1585.

Hubbard, S.S, Chen, J., Peterson, J., Majer, E.L., Williams, K.H., Swift, D.J., Mailloux, B., Rubin, Y., 2001. Hydrological characterization of the South Oyster bacterial transport site using geophysical data. Water Resour. Res. 37:2431–2456.

Keller, G. V., Frischknecht, F. C., 1966. Electrical methods in geophysical prospecting. Per-gamon Press, New York.

Kemna, A., Vanderborght, J., Kulessa, B., Vereecken, H., 2002. Imaging and characterisation of subsurface solute transport using electrical resistivity tomography (ERT) and equivalent transport models. Journal of Hydrology, 267, 125-146.

Kunisch, K., Volkwein, S., 2003. Galerkin Proper Orthogonal Decomposition for a General Equation in Fluid Dynamics. SIAM Journal on Numerical Analysis, 40(2), 492-515.

LaBreque, D.J., Miletto, M., Daily, W., Ramirez, A., Owen, E., 1996. The effects of noise on Occam's inversion of resistivity tomography data. Geophysics, Vol 6, N0.2, p. 538-548.

Lane, J.W., Jr., Day-Lewis, F.D., Versteeg, R.J., Casey, C.C., 2004. Object-based inversion of crosswell radar tomography data to monitor vegetable oil injection experiments. J. Environ. Eng. Geophys., 9, 63-77.

Lane, J.W., Jr., Day-Lewis, F.D., Casey, C.C., 2006. Geophysical monitoring of field-scale vegetable oil injections for biostimulation. Ground water, 44(3), 430-443, doi: 10.1111/j.1745-6584.2005.00134.x.

Lazarovitch, N., Warrick, A.W., Furman, A., Šimu˚nek, J., 2007. Subsurface water distribution from drip irrigation described by moment analyses. Vadose Zone J. 6 (1), 116–123.

LeBlanc, D. R., Garabedian, S. P., Hess, K. M., Gelhar, L. W., Quadri, R. D., Stollenwerk, K. G., Wood, W. W., 1991. Large-scale natural gradient tracer test in sand and gravel, Cape Cod, Massachusetts: 1. Experimental design and observed tracer movement, Water Resour. Res., 27(5), 895-910.

Li, Y.-T., Bai, Z., Su, Y., 2009. A two-directional arnoldi process and its application to parametric model order reduction. J. of Computational and Applied Mathematics, 226, 10-21, doi:10.1016/j.cam.2008.05.059

Loaiciga, H. A., Charbeneau, R. J., Everett, L. G., Fogg, G. E., Hobbs, B. F., Rouhani, S., 1992. Review of ground-water quality monitoring network design. J. Hydrau. Eng. 118:11-37.

Milanfer, P., Karl, W.C., Willsky, A.S., 1996. A moment-based variational approach to tomographic reconstruction. IEEE Trans. Image Process., 5, 459-470.

Miller, E.L., Kilmer, M., Rappaport, C., 2000. A new shape-based method for object localization and characterization from scattered field data, IEEE Transactions on Geoscience and Remote sensing, Vol. 38, 1682-1696.

Moysey, S., Knight, R. J., 2004. Modeling the field-scale relationship between dielectric constant and water content in heterogeneous systems. Water Resour. Res., 40, W03510, doi:10.1029/2003WR002589.

Moysey, S. M. J, Singha, K., Knight, R., 2005. A framework for inferring field-scale rock physics relationship through numerical simulation. Geophys. Res. Lett., 32, L083, doi:10.1029/2004GL022152.

Muller, K., Vanderborght, J., Englert, A., Kemna, A., Huisman, J.A., Rings, J., Vereecken, H., 2010. Imaging and characterization of solute transport during two tracer tests in a shallow aquifer using electrical resistivity tomography and multilevel groundwater samplers. Water Resour. Res. 46, W03502.

Oware, E. K., Moysey, S. M. J., Khan T., 2013. Physically based regularization of hydrogeophysical inverse problems for improved imaging of process-driven systems. Water Resour. Res., 49, doi:10.1002/wrcr.20462.

Pidlisecky, A., Haber, E., Knight, R., 2007. RESINVM3D: A 3D resistivity inversion package. Geophysics, 72(2), H1-H10, doi:10.1190/1.2402499.

Pidlisecky, A., Singha, K., Day-Lewis, F.D., 2011. A distribution-based parameterization for improved tomographic imaging of solute plumes. Geophys. J. Int., 187, 214-224, doi:10.1111/j.1365-246X.2011.05131.x.

Pinnau, R., 2008. Model reduction via proper orthogonal decomposition, in: W.H.A. Schilder and H. van der Vorst, Model Order Reduction: Theory, Research Aspects and Applications, Springer, New York, pp. 96-109.

Rathinam, M., Petzold, L.R., 2004. A new look at Proper Orthogonal Decomposition. SIAM Journal on Numerical Analysis, 41(5), 1893-1925.

Rubin, Y., 2003. Applied Stochastic Hydrogeology. Oxford University Press, Oxford.

Singha, K., Gorelick, S.M., 2005. Saline tracer visualized with three-dimensional electrical resistivity tomography: Field-scale spatial moment analysis. Water Resources Research, 41, W05023, doi:10.1029/2004WR003460.

Singha, K., Moysey, S. M., 2006. Accounting for spatially variable resolution in electrical resistivity tomography through field-scale rock physics relations. Geophysics, 71(4), A25-A28, doi:10.1190/1.2209753.

Tikhonov, A.N., Arsenin, V. Y., 1977. Solutions of ill-posed problems, John Wiley & Sons.

Winton, C., J. Pettway, C.T. Kelley, S. Howington, O.J. Eslinger, 2011, Application of proper orthogonal decomposition (POD) to inverse problems in saturated groundwater flow, *Advances in Water Resources*, 34, 1519-1526, doi: 10.1016/j.advwatres.2011.09.007.

Xiong, Y., Furman, A., Wallach, R., 2011. Moment analysis description of wetting and redistribution plumes in wettable water-repellent soils. Journal of Hydrology, 422-423, 30-42.

Yao, Y., Meerbergen, K., 2013. Parametric model order reduction of damped mechanical systems via the block arnoldi process. Applied Mathematics Letters, 26, 643-648, doi:10.1016/j.aml.2013.01.006.

Ye, M., Khaleel, R., Yeh, T.-C. J., 2005. Stochastic analysis of moisture plume dynamics of a field injection experiment.Water Resour. Res., 41, W03013, doi:10.1029/2004WR003735.

Yeh, T.-C. J., Ye, M., Khaleel, R., 2005. Estimation of effective unsaturated hydraulic conductivity tensor using spatial moments of observed moisture plume. Water Resour. Res., 41, W03014, doi:10.1029/2004WR003736.

CHAPTER FIVE

TIME-LAPSE APPLICATION OF POD FOR GEOELCTRICAL MONITORING OF LAB-SCALE SALINE-TRACER EXPERIMENT.

ABSTRACT

The ability of a geophysical estimation algorithm to invert real-world data is important to establishing useful scientific applications. We demonstrate the use of the POD-constrained adaptive inversion algorithm on real-world dataset. The POD algorithm is based on recursive refinements of center of mass (CoM) of tomograms in an effort to minimize the fidelity between the true and estimated CoMs. Resistivity measurements obtained from lab-scale saline-tracer unsaturated flow experiment were applied for the purpose of demonstrating the utility of the algorithm to interpret real-world datasets.

The estimation error of the solute release point is 17.6% with respect to the lateral spread of the target plume. This illustrates a potential utilization of the POD adaptive algorithm as a possible non-invasive tool for identifying unknown contaminant sources. This also shows that the algorithm can be applied to locate a region of maximum concentration of contamination, which can inform the design of remediation or sampling schemes. The continuous improvement in the misfit between the true and estimated release points is driven by high-order basis functions, which demonstrates the need for capturing more variability in the basis constraints. The dynamics of the respective contributions of the basis functions as the adaptive iteration progresses depict a shift from the patterns deemed important from the stochastic simulations of the target toward

patterns relevant for the reconstruction of the actual target. This illustrates the flexibility of the POD-constrained algorithm to move away from the characteristics of the *a priori* constraints in order to represent the observed resistivity data, i.e., the algorithm enforces *soft process* constraint. The POD algorithm presents a potential tool to leverage advances in mechanistic modeling to incorporate physics-based specifications into geophysical imaging. The complexity of the patterns to incorporate is unlimited, as long as it can be numerically simulated.

1. INTRODCUTION

Time-lapse electrical resistivity tomography (ERT) is becoming an increasingly important tool for monitoring subsurface processes due to advances in computational capabilities and field instrumentation. The increased rate of data acquisition facilitates static imaging (snapshots) of the subsurface through time. ERT time-lapse has been applied to monitor evolving targets such as infiltration [e.g., *Binley et al*., 2001; *Nimmo et al*., 2009], solute transport [e.g., *Slater et al*., 2000; *Kemna et al*., 2002, *Singha and Gorelick*, 2005], engineered *in-situ* remediation [e.g., *Ramirez et al*., 1996; *Lane et al*., 2004; *Hubbard et al*., 2008].

Of particular relevance to this study are the works of *Oware et al.* [2013] and *Oware and Mosey* [2014]. *Oware et al.* [2013] introduced a POD-constrained inversion algorithm that incorporates physics-based *a priori* constraints into geophysical imaging schemes. The algorithm constructs basis functions from training images. The basis functions are then applied to condition the geophysical optimization process. A limitation of the original algorithm is that the basis vectors are not translational in space during the inversion procedure.

To address this limitation, *Oware and Mosey* [2014] introduced the POD adaptive algorithm. The adaptive algorithm recursively updates the center of mass (CoM) of tomograms in order to minimize the misfit between the true and estimated CoM, conditioned on geophysical measurements.

Both *Oware et al.* [2013] and *Oware and Mosey* [2014] utilized hypothetical saturated flow and transport experiments to demonstrate the original and the adaptive versions of the POD algorithm. The objective of this study, in the spirit of advancement of the POD algorithm, is to demonstrate the performance of the POD strategy using a lab-scale, saline-tracer unsaturated experiment. The study also aims to illustrate the time-lapse imaging capability of the POD algorithm.

Two commonly applied time-lapse imaging strategies are the difference inversion and cascaded time-lapse inversion. The difference inversion involves the subtraction from the time-lapse data, data acquired from the target system at some baseline condition (reference data). The differenced data is then inverted, which is referred to as pre-data differencing time-lapse inversion. When the differencing is done after the inversion of the time-lapse and reference datasets, it is called post-model differencing time-lapse inversion. *Singha and Gorelick* [2005] reported that they did not observe significant differences between model resolutions recovered from post-model differencing in contrast to those obtained from pre-data differencing inversions, in a field-application.

The cascade time-lapse inversion, on the other hand, applies the inverted reference dataset as a starting model to invert subsequent time-lapse datasets. *Miller et al.* [2008], in their study to evaluate the performance of different time-lapse inversion techniques, found the post-model differencing and the cascaded time-lapse approaches to be superior. The authors, however, pointed out their preference for the latter approach due to its faster convergence rate and its ease of implementation compared to the difference approach. Therefore, the cascaded time-lapse inversion is adopted for the implementation of the POD time-lapse inversion in this study.

2. METHODS

2.1. Overview of Lab-scale Saline-tracer Experiment for Test Case

We performed a lab-scale, saline-tracer unsaturated experiment in a homogenous sand matrix to illustrate time-lapse imaging capability of the POD-constrained inversion algorithm. The experiment was performed in an acrylic tank of dimension 100 cm x 2 cm x 30 cm. An image of the experimental setup is shown in Figure 5.1. The small thickness (2 cm) of the model was specifically selected to produce a quasi-two-dimensional flow [e.g., *Pollock and Cirpka*, 2012], in an effort to generate a 2-dimensional parsimonious test case as opposed to a complicated 3-dimensional target.

To avoid enhanced flow from micro-layers as a result of uneven packing of the tank, we applied wet packing with continuous stirring. Afterwards, the saturated medium was allowed to drain under gravity for one hour before the commencement of the experiment.

This short drainage time allowed the infiltration domain to remain fairly moist in order to ameliorate the effects of high contact resistance for the resistivity measurement.

Sodium chloride solution with electrical conductivity of 18.91 S/m was utilized as a tracer in order to accentuate the electrical conductivity contrast between the background electrical conductivity values and those of the infiltrating media. Dye was also added to the inflow solution to enable video monitoring of the experiment. Brilliant Blue dye (C.I. Food Blue 42090) was selected due to its favorable properties such as mobility, high visibility, and low toxicity [*Flury et al.*, 1994].

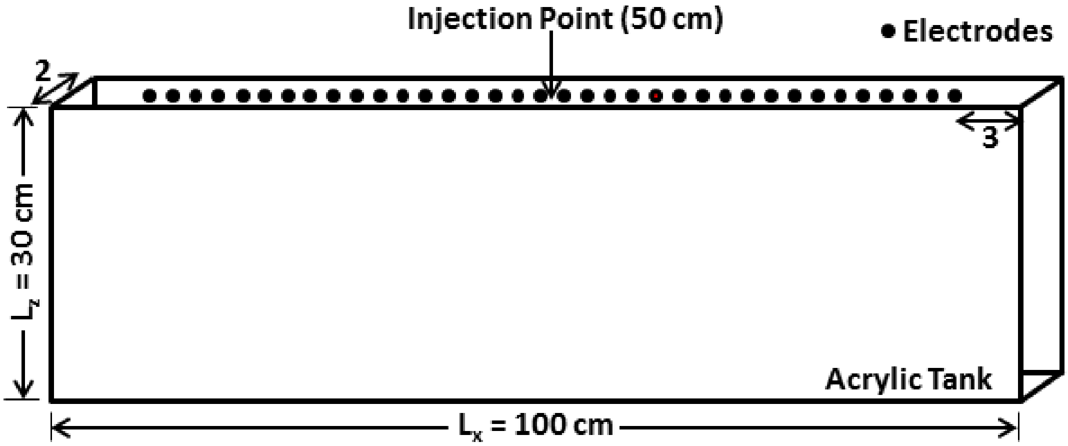

Figure 5.1: A schematic diagram of the experimental setup. A total of 48 surface electrodes were deployed with 2 cm spacing between them.

The dyed saline solution was released at the 50 cm mark on the surface of the tank (Fig. 5.1) with a continuous drip rate of 0.59 ml/min. The experiment lasted for three hours. A total of 106 ml of the saline solution was released over the course of the experiment.

A Syscal Pro ten-channel resistivity-meter with a 48 switch board by IRIS Instruments was used to perform the resistivity monitoring. All of the 48 electrodes were distributed on top of the sand matrix with 2 cm spacing between them (Fig. 5.1). Dipole-dipole electrode configuration was employed for all measurements in the resistivity survey. A total of 45 independent current pairs were triggered within each complete survey resulting in a total of 1035 quadripole measurements. To estimate data errors, reciprocal measurements (i.e., interchanging the positive and negative current sources) were also performed during each survey. The acquisition time for both the forward and reciprocal measurements lasted for 4.5 mins for each complete survey. The surveys were repeated every 0.6 mins to enable time lapse monitoring of the experiment.

2.2. Details for Generating Case-specific POD Basis Patterns

The POD inversion scheme requires the construction of basis functions from training images (TIs) in a bid to capture relevant hydrological features specific to the system under investigation. To generate the training dataset for this purpose, we applied Monte Carlo sampling of the target process [e.g., *Oware et al.*, 2013] using HYDRUS 2D/3D [*Simunek et al.*, 2008] variably saturated flow and transport model. The process of interest in this study is an infiltrating saline-tracer through a fairly homogeneous, variably saturated sand matrix (Fig. 5.1).

The Hydrus simulations were based on a conceptual model of the experimental design applied in generating the test case (Section 2.1), in an effort to generate problem-specific TIs that captures our conceptual understanding of the lab-scale test case. To increase the variability in the training dataset in order to capture a wide range of uncertainties in an attempt to increase the chances of capturing basis patterns that may be relevant in reconstructing the target, multiple combinations of typical hydraulic properties of sand (Tab. 5.1), varying antecedent matrix saturations (0.08 and 0.12), and varying injection flux (1 and 1.5 m/day) were applied to generate the TIs, in an effort to capture multiple rates of infiltrating fronts and multiple solute morphologies. The combinations resulted in the simulations of a total of 1374 TIs.

In most practical applications, while the region of solute release (i.e., contaminant source) may be known, the exact location is, however, rarely known. To appraise the performance of the POD algorithm in the event of uncertain knowledge about the solute release location, the initial inflow point in the simulation of the TIs was shifted to the 70 cm mark as opposed to the true release location of 50 cm.

Table 5.1: Typical hydraulic parameter values for sand were used in generating the training images (TIs). The values in parenthesis indicate the step size applied to generate multiple combinations of parameters to simulate the TIs. Q_r and Q_s denote the mean residual and saturated water contents, respectively. Alpha and *n* are empirical constants that determine the shape of the water retention curve [*van Genuchten*, 1980] while K_s signifies saturated hydraulic conductivity. *Sources of Parameters*: [*Rawls et al*, 1982; *Schaap*, 1999].

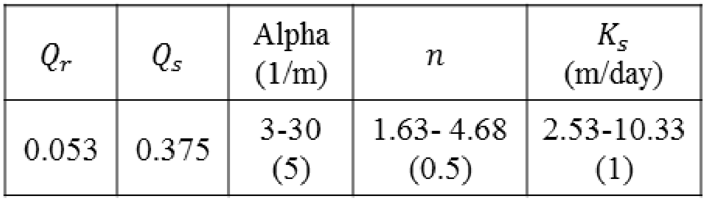

Q_r	Q_s	Alpha (1/m)	n	K_s (m/day)
0.053	0.375	3-30 (5)	1.63- 4.68 (0.5)	2.53-10.33 (1)

The simulated concentration profiles were converted to electrical conductivity based on the relationship 2 mg/L = 1μS/cm [*Keller and Frischknecht*, 1966]. The electrical conductivities, thereafter, were converted to bulk electrical conductivities (σ_{bulk}) according to the following Archie's [*Archie*, 1942] unsaturated petrophysical model:

$$\sigma_{bulk} = \sigma_f n^m S^d, \tag{10}$$

where *n* is the porosity, which was estimated to be 0.4; σ_f represents pore fluid electrical conductivity; *m* denotes the cementation factor, which is a measure of pore connectivity [*Jackson et al*., 1978] and was set to 1.3; S denotes water saturation; and *d* represents saturation index, which was set to 2.3. Effect of surface conductivity in the clean sand was assumed to be negligible due to the absence of clay [*McNeil*, 1980].

Background bulk electrical conductivity was estimated to be about 6.14 mS/m, based on inversion data (reference tomogram) from resistivity monitoring of the background condition prior to the onset of infiltration. Electrical conductivity of tap water was measured to be 9.5 mS/m.

The simulated TIs were decomposed into their basis functions as explained in Chapter 2 section 3.2. Images of the first twenty principal patterns captured from the TIs with their release point located at the 70 cm mark are shown in Figure 5.2.

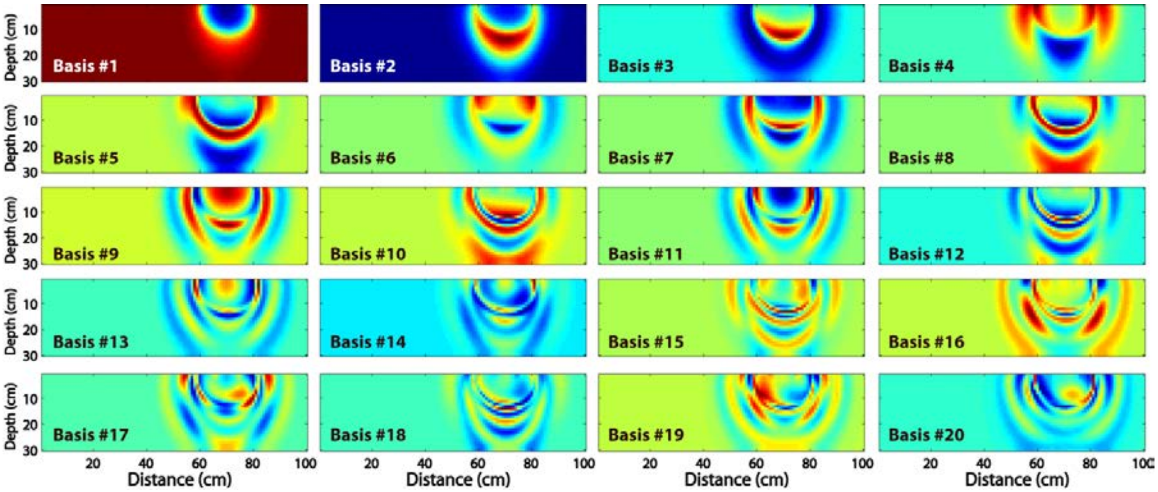

Figure 5.2: Images of first twenty dominant POD basis functions for the first time-step. They are numbered in decreasing order of dominance. Those of the subsequent time steps are not shown, but they follow similar patterns with increasing spread (see mean of training images in Figure 5.7 for a sense of scale). Note that the lateral center of mass of the basis is located at the 70 cm mark whereas the true injection point is at 50 cm. Also, the wide spread of the basis images is due to logarithmic scaling of the basis, since the target is the log of conductivities.

2.3. Details for the Resistivity Inversions

In this section, we provide a description of the inversion protocol. The experiment was monitored at three time steps, i.e., 30, 60, and 90 mins after onset of infiltration.

The POD adaptive algorithm presented by *Oware and Moysey* [2014] was applied to estimate the release point. It was assumed that the release was at the surface, therefore, only the lateral coordinate of the release point was estimated. The POD adaptive algorithm is based on recursive refinement of center of mass (CoM) of tomograms in order to minimize the misfit between true and estimated CoM. Specifically, the first POD data inversion was performed with the basis functions localized at the 70 cm mark. Afterwards, the lateral CoM of the recovered image was estimated. The estimated lateral CoM then served as the location of the basis vectors for the next iteration of the inversion process. The inversion was recursively repeated in this fashion until convergence. That is, until there was no significant changes in the estimated lateral CoM.

The full inversion of all the time-step datasets then proceeds with the basis functions localized at the estimated CoM. Since we adapted the cascaded time-lapse approach, the reference tomogram was applied as the starting model for the inversion of each time-step dataset.

Data errors were assumed to be normally distributed and uncorrelated; therefore, the diagonal elements of the data weighting matrix, $\mathbf{W}_{\boldsymbol{d}}$ in Eq.9, comprised the inverse of data standard deviations. *Tiedman and Green* [2013] discuss the effect of neglecting correlations in observed errors on parameter estimation. Data variances were estimated from reciprocal measurements as presented by *LaBrecque et al.*, 1996 as:

$$variance_i = A^2 + B^2(d_i)^2, \tag{11}$$

where d_i denotes the ith data point, and A^2 and B^2 are fitting parameters, which were estimated in this study to be 0.64 and -0.19, respectively. However, the estimation of A^2 and B^2 were found to be severely underestimated as the inversion would not converge. The A^2 and B^2 parameters were, therefore, scaled by 1000. Note that the estimation of A^2 and B^2, in a least-squares sense, involved a pool of recorded data from all the time-steps considered.

3. RESULTS AND DISCUSSION

3.1. Adaptive estimation of release point

As the iterations progress the estimated plume begins to form coherently at a particular region (Fig. 5.3) and the evaluated release point approaches the true value (Fig. 5.4). A plausible explanation for the observed continuous reduction in the misfit between the estimated and true release points can be deduced from the dynamics of the FofC weights as the iterations progress (Figs. 5.5 and 5.6). The comparatively small FofC weight of the first-order basis at the beginning of the iteration (Fig. 5.6) implies that the optimization at the early iterative stages depends more on the wide spread of the high-order basis in order to reach the sensitivity region of the target plume, which bias the updated release point toward the true value.

For instance, the white cross in Fig. 5.3 iteration 1 shows the initial location of the basis functions, which also depicts the central location of the first-order basis. However, the reconstruction in Fig. 5.3, iteration 1 shows a high electrical conductivity in the sensitivity region of the target plume, a region that is far beyond the lateral spread of the first-order basis (Fig. 5.2). This observed reconstruction in a region far beyond the lateral reach of the first-order basis is as a result of the accentuation of high-order bases whose lateral spread extends to the sensitivity region of the target plume, which explains the comparatively small fraction of coefficient contribution from the first-order basis for the for the first iteration (Fig. 5.6).

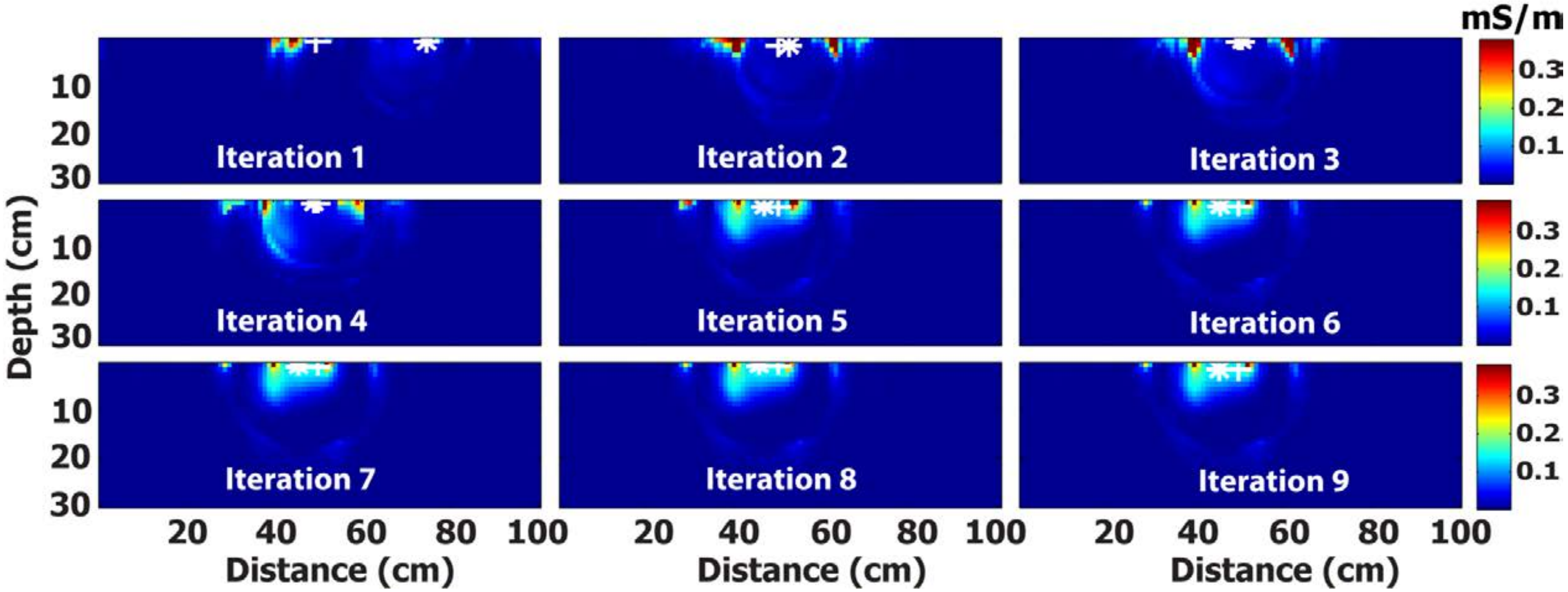

Figure 5.3: Recovered tomograms after each update to estimate the injection point. The white half star shows the starting and estimated release points, whereas the white half cross depicts the true release point. Note: the cross and star symbols are supposed to be on the surface. They were slightly shifted downward to enhance visibility. The inversion technique is based on the POD adaptive algorithm by *Oware and Moysey* [2014]. Since we were interested in estimating the injection point, an expected high conductivity region, the estimated background conductivity values, including estimated conductivity values greater than the estimated background, were set to zero prior to each CoM estimation, in order to accentuate the plume

As the misfit between the true and the estimated release point reduces, however, the reverse of this process occurs. The spread of the first-order basis begins to reach the sensitivity zone of the target plume and, therefore, more weight is now shifted unto the first-order basis in order to reconstruct the target. These phenomena suggest that while the construction of the target profile is controlled by the first-order basis, the drifting of the estimated release point toward the true value, during the early stages of the adaptive optimization is, on the other hand, driven by the high-order basis.

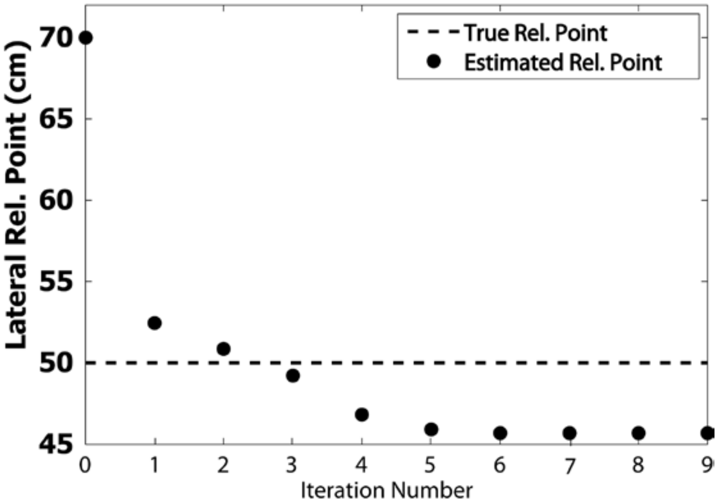

Figure 5.4: Comparison of true lateral release location (50 cm) with those estimated after each update. Estimation of the release location attained an asymptotic value of 45.7 cm after 5th iterations.

In the same context of the dynamics of coefficient contribution of the high-order basis as iteration progresses, analysis of Fig. 5.5 discloses that while basis numbers 3, 6, and 13 were the 3rd, 6th, and 13th (Fig 5.2) principal features extracted from the training dataset, they were however the 2^{nd}, 4^{th}, and 5^{th} (Fig. 5.5, iteration 9) most important patterns in reconstructing the target. This reflects the utilization of the resistivity measurements to capture details about that target that were not represented in the stochastic simulations of the target, i.e., the training images. It also demonstrates the flexibility of the POD algorithm to drift away from the *a priori* specifications in order to represent the recorded data from the target. That is, the POD algorithm invokes a *soft process* constraint.

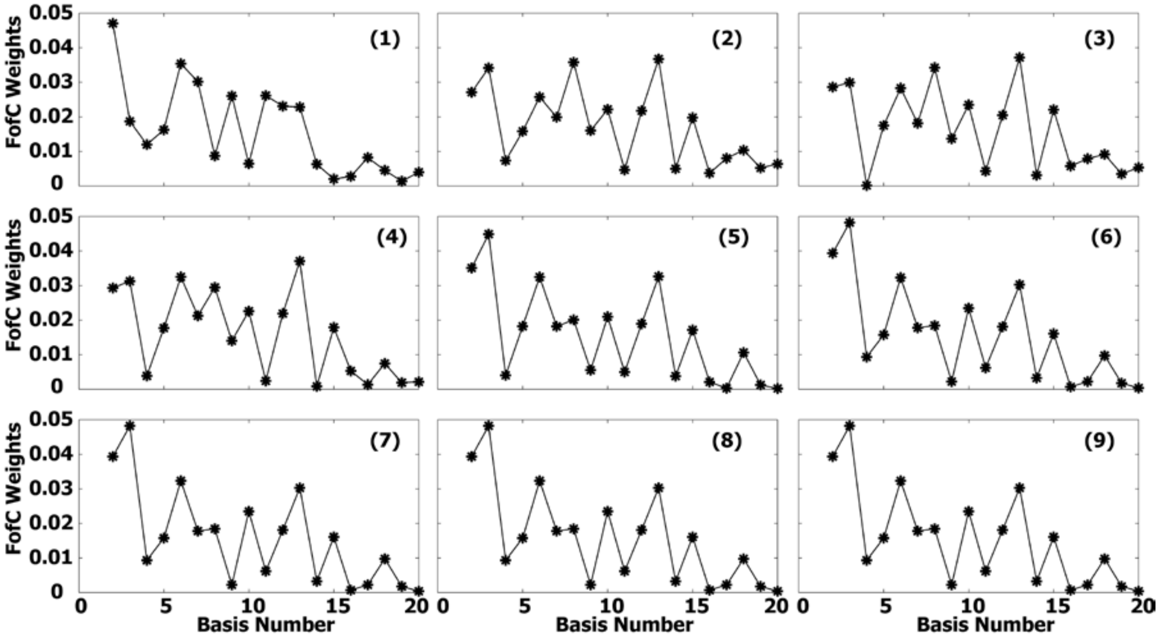

Figure 5.5: Plots illustrating the dynamics of the high-order basis coefficient weights during the adaptive optimization process. The optimization process is more dependent on the high-order basis at the early stages of the iteration (see also Fig. 6). Note that the numbering of the high-order basis starts from 2. Also FofC defines fraction of coefficient.

Inspections of the tomograms in Figure 5.3 and the plots in Figure 5.4 indicate that the estimation converged after six iterations with an asymptotic value of 45.7 cm. The lateral spread of the target was estimated to be 24.5 cm based on the dye plume. This translates into a relative estimation error of 17.6% with respect to the lateral spread of the target. Since the geometry of the evolved plume appears slightly asymmetric (Fig. 5.7b), we are of the opinion that the estimated release point may be closer to the lateral center of mass of the true plume in contrast with the actual release point. We noted some artefacts in the background values of the converged solution, which we believe are due to outline of some of the high-order bases used for the inversion.

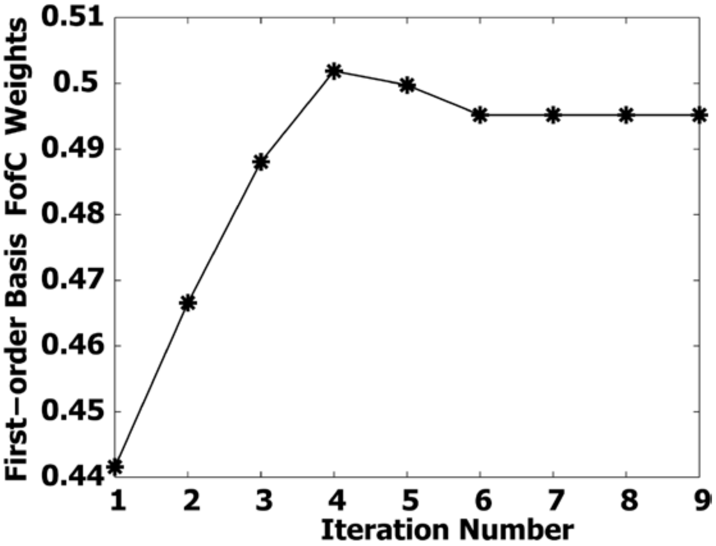

Figure 5.6: Plot depicting the dependence of the adaptive optimization on the first-order basis function with increasing number of iterations. Note: FofC defines fraction of coefficient.

3.2 Time-lapse Implementation of the POD-constrained Inversion Framework

There seems to be underestimation of the lateral and vertical spatial variances of the POD EC reconstructions (Fig. 5.7, column 3). A close examination of Fig. 5.7 discloses better match-ups between the dye images (Fig 5.7, column one) of, for instance, time-step t and the reconstructed images of time-step t+1. This suggests that the resistivity response is lagging the dye plumes by one time-step. Further explanation and evidence that support this assertion are provided in Chapter Six, section 3. As a result of this temporal discrepancy, the analysis that follows associates dye plume images of time-step t with POD reconstructions of time-step *t*+1.

Fig. 5.7, column two shows results of the mean of stochastic sampling of the target plume anchored to a conceptual model of the imaging domain and uncertain release point (70 cm). These TI mean images depict how the targets would have been stochastically characterized based on the physics of the process alone, without any geophysical constraints. Fig. 5.7, column three, on the other hand, presents results of the POD-constrained EC reconstructions constrained to the resistivity measurements.

In this study, whiles the stochastic sampling alone would have missed the location of the true plume, the fusion of the resistivity data using the adaptive algorithm helped to resolve the uncertainty regarding the location of the true plume. However, in terms of the target's morphology, qualitative comparison of the dye plumes with images of TI mean and the POD reconstructions reveals that the POD reconstructions could not capture small details in the morphology of the target beyond the details captured by the TI means. The inability of the POD technique to reconstruct small details in the target is presumably due to lack of variability in the basis functions. Examination of the high-order basis in Fig. 5.2, for example, shows several circularly shaped patterns due to the homogeneous assumption upon which the generation of the training dataset is based.

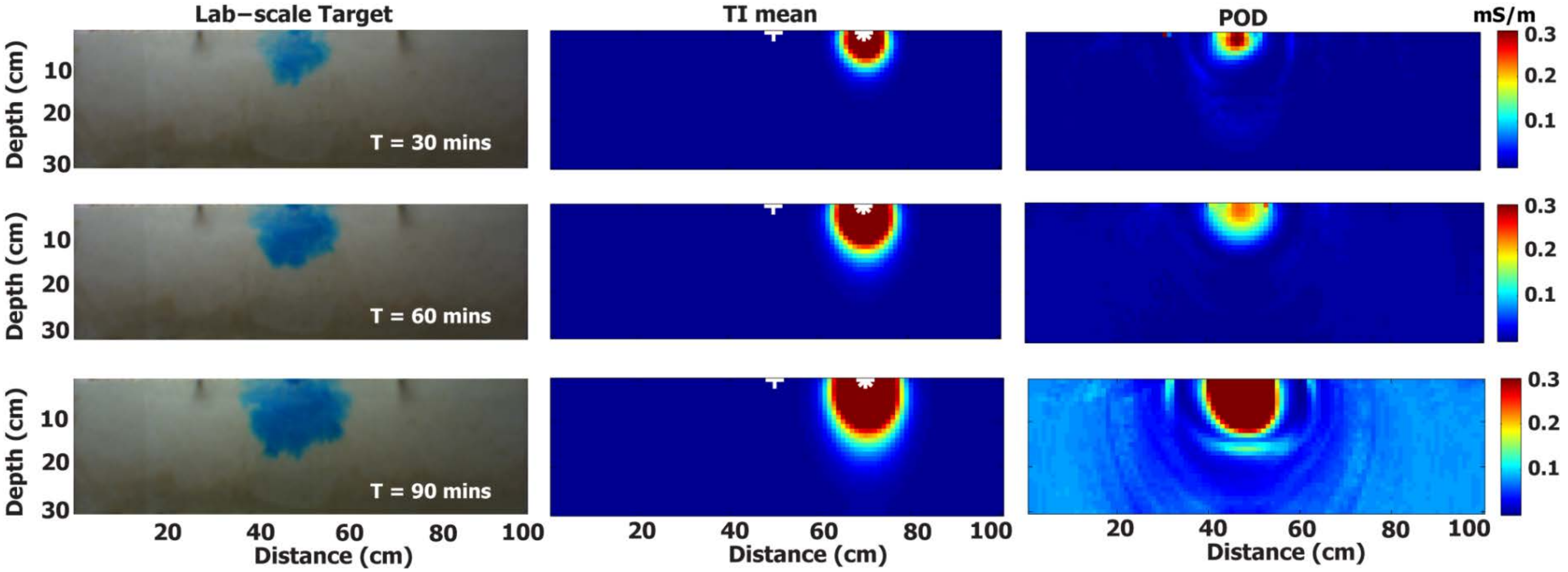

Figure 5.7: Comparison of images of the lab-scale target with those of the mean of simulated training images (TI mean) and those obtained from the POD reconstructions. (Colum one) Lab-scale target; (Column two) TI mean; (Colum three) POD snapshots. The white half star on the TI means shows the starting release points (70 cm), whereas the white half cross depicts the true release point (50 cm). The cross and star symbols are supposed to be on the surface. They were slightly shifted downward to enhance visibility.

4. CONCLUSIONS

We demonstrate the applicability of the POD-constrained inversion algorithm and its adaptive version presented by *Oware et al*. [2013] and *Oware and Mosey* [2014]. Resistivity measurements obtained from lab-scale saline-tracer unsaturated flow experiment were applied to test the potential applicability of the POD inversion scheme on real-world data.

Real-world data present uncertainty challenges such as measurement errors, non-parametric error distributions, lack of data sensitivity, faulty instruments, operational errors, errors as a result of approximation of a 3-dimensional world to 2-dimensional case, etc. While the model resolutions presented here are not be elegant, they demonstrate the potential utility of the POD-constrained algorithm in practical applications, especially, given that is the very first application of the POD-constrained inversion algorithm on real-world data. The issue of lack of variability in the basis function will be addressed in the future in an effort to improve the POD reconstructions.

We have demonstrated that the continuous improvement in the fidelity between the true and estimated release points, in the adaptive algorithm, is driven by the high-order basis functions, which usually have spatial spread that may extend to the sensitivity region of the target. This stipulates the need for capturing more variability in the basis constraints, especially, patterns with wide spatial reach.

The dynamics of the respective contributions of the basis functions as the adaptive iteration progresses show a drift from the patterns that were deemed important from the stochastic simulations of the target anchored on the conceptual specification of the experimental design. This finding reflects the incorporation of additional information from the resistivity measurements to reconstruct features of the target that were not captured in the unconditional stochastic simulations alone. It also illustrates the flexibility of the POD-constrained algorithm to shift away from the characteristics of the *a priori* constraints in order to represent the observed resistivity data, i.e., the ability the algorithm to enforce *soft process* constraint.

REFERENCES

Archie, G.E., 1942. The electrical resistivity log as an aid in determining some reservoir Characteristics. Trans. Am. Inst. Min. Metall. Pet. Eng., 146, 54–62.

Binley, A., Winship, P. , Middleton, R., Pokar, M., West, L. J. , 2001. High resolution characterization of vadose zone dynamics using cross-borehole radar. Water Resour. Res., 37 (11), 2639-2652.

Flury M., Fluhler, H.,Jury, W.A., Leuenberger, J., 1994. Susceptibility of soils to preferential flow of water: A field study. Water Resour. Res., 30 (7), 1945-1954.

Hubbard, S.S.,Williams, K., Conrad,M., Faybishenko,B., Peterson, J.,Chen, J., Long, P. & Hazen, T., 2008. Geophysical monitoring of hydrological and biogeochemical transformations associated with Cr(VI) biostimulation, *Environ. Sci. Technol.,* 42(10), 3757–3765, doi:10.1021/es071702s.

Jackson, P.D., Smith, D.T., Standford, P.N., 1978. Resistivity-porosity-particle shape relationships for marine sands. Geophysics, 43, 1250-1268.

Kelle, G.V., Frischknecht, F.C., 1966. Electrical methods in geophysical prospecting, Pergamon, Oxford, U.K.

Kemna, A., Vanderborght, J., Kulessa, B., Vereecken, H., 2002. Imaging and characterisation of subsurface solute transport using electrical resistivity tomography (ERT) and equivalent transport models. Journal of Hydrology, 267, 125-146.

LaBrecque, D. J., M. Miletto,W. Daily,A. Ramirez, E. Owen, 1996. The effects of noise on Occam's inversion of resistivity tomography data: Geophysics, 61, 538–548.

Lane, J.W. Jr., F.D. Day-Lewis, R.J. Versteeg, and C.C. Casey. 2004. Object-based inversion of cross-well radar tomography to monitor injection experiments. Journal of Environmental and Engineering Geophysics 9, no. 2: 63–77.

McNeil, J.D., 1980. Electromagnetic terrain conductivity measurement at low induction numbers, tech notes TN-6, Geonics Limited, Canada.

Miller, C.R., Routh, P.S., Brosten, T.R., McNamara, J.P., 2008. Application of time-lapse ERT to watershed characterization. Geophysics, 73 (3), 7-17. doi:10.1190/1.2907156

Nimmo, J.R., Perkins, K.S., Schmidt, K.M., Stock, J.D., Miller, D.M. & Singha, K., 2009. Hydrologic characterization of desert soils with varying degrees of pedogenesis. I. Field experiments evaluating plant-relevant soil-water behavior, *Vadose Zone J.,* **8,** 480–495. doi:10.2136/vzj2008.0052.

Oware, E. K., Moysey, S. M. J., Khan T., 2013. Physically based regularization of hydrogeophysical inverse problems for improved imaging of process-driven systems. Water Resour. Res., 49, 1-10. doi:10.1002/wrcr.20462.

Oware, E. K., Moysey, S. M. J., 2014. Geophysical evaluation of solute plume spatial moments using an adaptive POD algorithm for electrical resistivity imaging. Journal of Hydrology, 517, 471-480. doi:x.doi.org/10.1016/j.jhydrol.2014.05.054

Pollock, D., Cirpka O. A., 2012. Fully coupled hydrogeophysical inversion of a laboratory salt tracer experiment monitored by electrical resistivity tomography, Water Resour. Res., 48, W01505, doi:10.1029/2011WR010779.

Rawls W.J., Brakensiek, D.L., Saxton, K.E., 1982. Estimation of soil water properties. Trans. of the ASAE, Paper No. 81-2510, 1316-1328.

Ramirez, A., W. Daily, A. Binley, D. LaBrecque and D. Roelant, 1996. Detection of Leaks in Underground Storage Tanks Using Electrical Resistance Methods, (UCRL-JC-122180, October, 1995), J. Engineering and Environmental Geophysics, 1, 189-203.

Schaap, M.G., 1999. Rosetta, version 1.0, U.S. Salinity Laboratory, U.S. Department of Agriculture, Riverside, California.

Slater, L., A.Binley, W.Daily and R.Johnson, 2000, Cross-hole electrical imaging of a controlled saline tracer injection, J.Applied Geophysics, 44, 85-102.

Šimu˚nek, J., van Genuchten, M.T., Sejna, M., 2008. Development and applications of the HYDRUS and STANDMOD software packages an related codes. Vadose Zone Journal, 7, 587-600. doi:10.2136/vzj2007.0077

Singha, K., and S.M. Gorelick (2005), Saline tracer visualized with three-dimensional electrical resistivity tomography: Field-scale spatial moment analysis, Water Resources Research, 41, W05023, doi:10.1029/2004WR003460.

Tiedman C.R., Green C.T., 2013. Effect of correlated observation error on parameters, predictions, and uncertainty. Water Resour. Res., 49, doi:10.1002/wrcr.20499.

van Genuchten, M.T., 1980. A closed-form equation for predicting the hydraulic conductivity of unsaturated soils. Soil Society of America Journal, 44(5), 892-898.

CHAPTER SIX

MCA TIME-LAPSE INVERSION: A NEW APPROACH TO GEOELCTRICAL MONITORING OF DYNAMIC HYDROLOGICAL PROCESSES

ABSTRACT

Geophysical time-lapse inversion is a useful non-invasive tool for monitoring subsurface dynamic processes. The cascaded time-lapse inversion is a popular time-lapse inversion strategy that utilizes inverted baseline data as a starting model for inverting subsequent time-lapse datasets. This approach implicitly assumes time-invariance of the transient system and, therefore, does not consider the physics of the process driving the evolving system from the reference condition to the current state. We propose a new time-lapse inversion scheme, maximum covariance analysis (MCA) time-lapse inversion, which incorporates into each starting model, the physics of the time-variant process responsible for the state transitioning between two adjacent time-periods. The strategy uses training images (TIs) to construct temporal covariance structure between two adjacent time-periods of interest. The TIs are generated via Monte Carlo simulations of the target process anchored to a conceptual model of the imaging system. MCA is then applied to construct coupled patterns between the two adjacent time-steps from the temporal covariance matrix. Given a known or an estimate of the t time-step parameters, an unconditional estimate (UCE) of the t+1 time-period model is retrieved via the coupled relationship, based on the concept of maximum covariance regression. The UCE then serves as a starting model for the inversion of the t+1 dataset. We apply a lab-scale,

saline-trace experiment to demonstrate the potential of the proposed strategy. Qualitative comparison of dye monitored images of the lab-scale target with those retrieved from the proposed scheme and those obtained from the cascaded time-lapse based on the POD-constrained inversion strategy are made. The proposed MCA strategy appears to outperform the cascaded time-lapse as the monitored time-periods increase. We observed that resistivity response lags dye monitored plume by about 30 mins.

1. INTRODUCTION

Geophysical time-lapse inversion is becoming a popular non-invasive tool for gaining qualitative and quantitative insights into subsurface dynamic processes. Electrical resistivity tomography (ERT) time-lapse inversion, in particular, has been applied to monitor subsurface evolving targets such as vadose zone water movement [e.g., *Park*, 1998; *Yeh et al.*, 2002; *French et al*., 2002], conductive tracer migration [e.g., *Slater et al*., 2000; *Singha and Gorelick*, 2005; *Kim et al*., 2009] and, remediation processes [*Ramirez et al*., 1993; *Daily and Ramirez*, 1995].

There are several time-lapse inversion strategies such as ratio inversion [e.g. *Daily et al*., 1992], difference inversion [e.g., *LaBrecque and Yang*, 2001], cascaded time-lapse [*Anno and Routh*, 2007; *Odenborger et al*., 2007; *Miller et al*., 2008], simultaneous time-lapse inversion [e.g., *Hayley et al*., 2011].

The difference and cascaded time lapse appear to be the commonly utilized time lapse techniques. Difference inversion [*LaBrecque and Yang*, 2001], inverts the difference between data at a particular time and data obtained at a reference time (reference data), which is referred to as pre-data difference inversion. The differencing can also involve the difference between the inverted data at a particular time and the inverted reference data, which is also referred to as post-model difference inversion. The cascaded time-lapse, on the other hand, utilizes the inverted reference data as initial model for the inversion of subsequent time-lapse datasets.

Miller et al. [2008], in their application of ERT for watershed characterization, appraised various strategies for inverting time-lapse data and found the post-model difference and the cascaded time-lapse approaches to be superior. The authors, however, pointed out their preference for the cascaded time-lapse. Therefore, the cascade time-lapse inversion is adopted as a reference time-lapse methodology to compare with the maximum covariance analysis (MCA) strategy proposed in this paper.

Miller et al. [2008] described some advantages of the cascaded time-lapse inversion, such as faster convergence rate and its ease of implementation compared to the difference approach. While these benefits are significant, we believe that applying a base tomogram as a starting model for inverting future time-lapses data does not consider the physics of the underlying time-variant process that is driving the transition of the target variables from the baseline condition to its current state.

We propose a new dynamic inversion strategy, MCA time-lapse inversion, which incorporates into each starting model the physics of the time-variant process driving the spatiotemporal evolution of the target parameters.

MCA [*Meehl,* 1973; *Meehl and Yonce*, 1996; *von Storch and Zwiers*, 1999], which is also known as singular value decomposition [*Kutzbach*, 1967; *Bretherton et al.*, 1992;

Wallace et al., 1992], maximizes the covariance between two co-varying fields. MCA is used in climate studies for applications such as identification of coupled patterns between two fields, for statistical downscaling of GCM (Global Circulation Model) data to the local scale, and also for forecasting [e.g., *Bretherton et al.*, 1992].

Of particular relevance to this contribution are the works of *Oware et al*. [2013], *Oware and Mosey* [2014], and *Oware and Mosey* [Chapter five]. *Oware et al*. [2013] presented the original POD-constrained strategy that incorporates non-parametric, site-specific physics-based patterns into geophysical inversion framework. A notable limitation of the original POD-constrained algorithm was that it lacked the ability to shift the basis images during the optimization procedure. To address this limitation, *Oware and Mosey* [2014] presented an adaptive version of the POD-constrained scheme, which recursively shifted the center of mass of the basis functions, in an effort to minimize the misfit between the estimated and true centers of mass, conditioned on the geophysical measurements. *Oware and Mosey* [Chapter five] employed lab-scale data to demonstrate the POD- constrained algorithm in a cascaded time-lapse inversion fashion.

The fundamental difference between the POD-constrained scheme and the proposed MCA strategy is that, while POD bases are constructed from covariance matrix denoting one time-step (field), the construction of coupled MCA basis, on the contrary, is based on the cross-covariance between two time-steps (fields). This implies that the POD-constrained inversion is a static imaging strategy, whereas, MCA is a dynamic imaging technique.

The computational framework for the implementation of the proposed MCA time-lapse inversion proceeds in five major steps (Fig. 6.1): (1) Monte Carlo simulation of training images based on a conceptual model of the imaged system; (2) construction of coupled patterns. A homogenous half space model of background values is then projected onto the *t*+1 basis to serve as starting model $(\boldsymbol{c}_0)$; (3) the optimization then proceeds to retrieve $\boldsymbol{c}_{t+1}$ conditioned on geophysical measurements; (4) the reconstruction of the model parameters, $\mathbf{m}_{t+1}$; (5) the recovered $\mathbf{m}_{t+1}$ is utilized as $\mathbf{m}_t$ for the next iteration, which is projected onto the t+1 basis to serve as input starting model $(\boldsymbol{c}_t)$ for the next iteration. The process is repeated for all the imaging time steps.

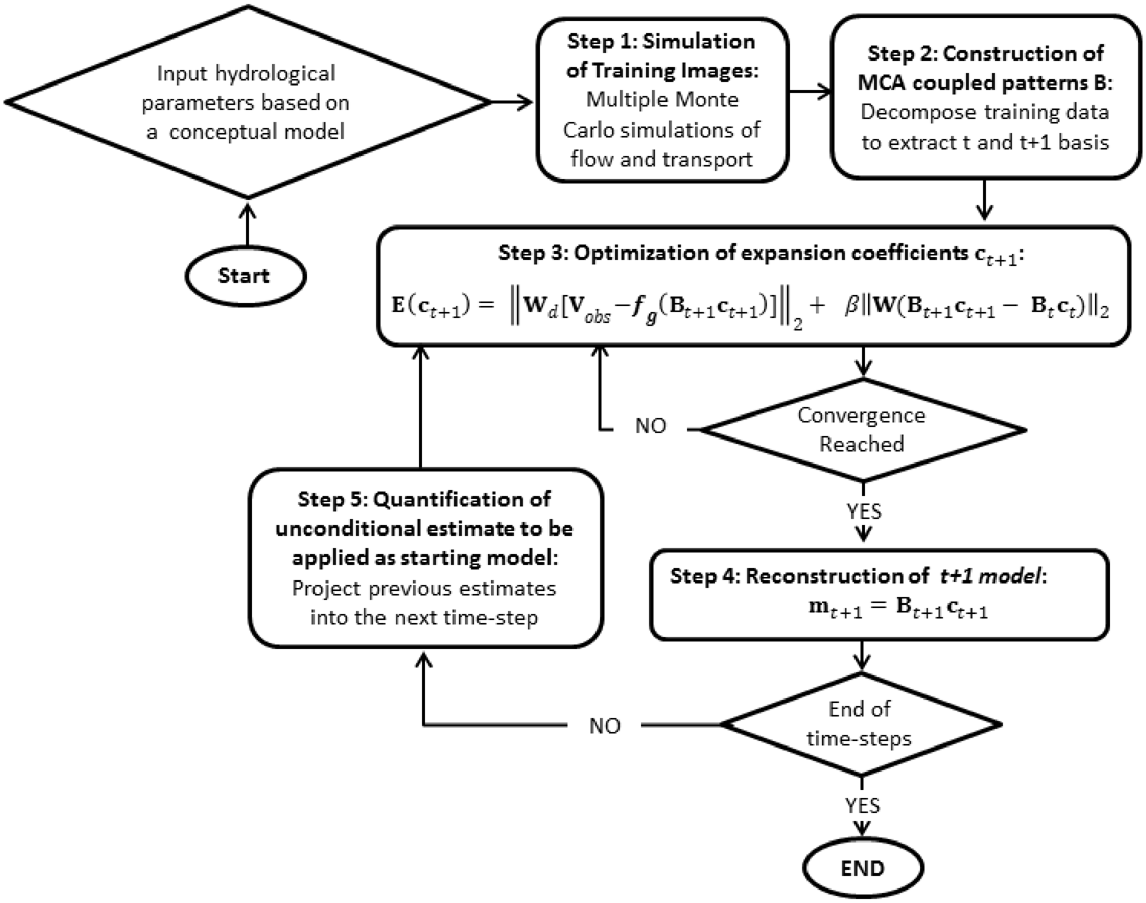

Figure 6.1: Computational scheme for the implementation of the MCA time-lapse inversion modality. See section 2.2 Eq.9 for definition of variables and explanation of the optimization model.

2. MAXIMUM COVARIANCE ANALYSIS (MCA) THEORY

This section provides details of the proposed mathematical framework for constructing coupled patterns between two consecutive time-steps (section 2.1). Section 2.2 outlines how the proposed MCA strategy will be implemented in the standard Tikhonov geophysical inversion framework. Detailed description of MCA is provided by von *Storch and Zwiers* [1999].

2.1 Obtaining Coupled Pairs of Maximum Covariance Patterns (MCP)

Coupled variability between two successively evolving fields can be constructed by maximizing the co-variability between the two fields. Consider two adjacent time series of "left" and "right" state parameters $\boldsymbol{\sigma}_t \in \mathbf{R}^M$ and $\boldsymbol{\sigma}_{t+1} \in \mathbf{R}^M$, respectively. Each field can be expressed as a linear combination of its basis patterns, that is:

$$\boldsymbol{\sigma}_t = \mathbf{B}_t \mathbf{c}_t \quad \text{and}$$

$$\boldsymbol{\sigma}_{t+1} = \mathbf{B}_{t+1} \mathbf{c}_{t+1}, \qquad (1)$$

where $\mathbf{c}_t$ and $\mathbf{c}_{t+1}$ are the time series expansion coefficients and $\mathbf{B}_t$ and $\mathbf{B}_{t+1}$ are the pairs of coupled patterns between the "left" and "right" spaces. Note that the expansion coefficients represent the transformed data, or the component of the original data in the optimal basis space (transformed coordinate system). Specifically,

$$\mathbf{c}_t = \mathbf{B}_t^T \boldsymbol{\sigma}_t \quad \text{and}$$

$$\mathbf{c}_{t+1} = \mathbf{B}_{t+1}^T \boldsymbol{\sigma}_{t+1}, \qquad (2)$$

where T denotes transpose. From Eq.2, the covariance between the two expansion coefficients can be written as:

$$\mathrm{Cov}(\mathbf{c}_t, \mathbf{c}_{t+1}) = \mathbf{B}_t^T \mathbf{S}_{\sigma_t \sigma_{t+1}} \mathbf{B}_{t+1} \tag{3}$$

where Cov denotes covariance and $\mathbf{S}_{\sigma_t \sigma_{t+1}} \in \mathbf{R}^{MxM}$ represents the cross-covariance between the two successive domains. To identify the pairs of coupled patterns that capture the most coupled variability between the two fields, we maximize Eq.3. The identified basis functions must be linearly independent for Eq.1 to be valid. Therefore, the maximization of Eq.3 is subject to the orthogonality criterion defined as:

$$\mathbf{B}_t^T \mathbf{B}_t = 1 \text{ and}$$

$$\mathbf{B}_{t+1}^T \mathbf{B}_{t+1} = 1. \tag{4}$$

The temporal covariance, $\mathbf{S}_{\sigma_t \sigma_{t+1}}$, can also be factorized into its “left” and “right” coupled basis using singular value decomposition (SVD) [e.g., *Castleman*, 1996; *Oware and Moysey*, 2014] as follows:

$$\mathbf{S}_{\sigma_t \sigma_{t+1}} = \mathbf{B}_t \mathbf{\Lambda} \mathbf{B}_{t+1}^T \tag{5}$$

where $\mathbf{\Lambda} \in \mathbf{R}^{MxM}$ is a diagonal matrix representing singular values. It can be deduced from Eq.s 3, 4, and 5 that: $\mathrm{Cov}(\mathbf{c}_t, \mathbf{c}_{t+1}) = \mathbf{\Lambda}$. Hence, SV decomposition of the temporal covariance between two adjacent time steps will yield the maximum covariance between their respective expansion coefficients and also identify their coupled pairs of maximum covariance patterns (MCP)

2.2 MCA time-lapse inversion

Given *a priori* coupled pairs of MCP between two successive time steps, it follows from maximum covariance regression (MCR) that if the left state parameters of a coupled system are known (predictor), then its associated right parameters can be predicted (predictand), and vice versa [e.g., *Troccoli et al.*, 2008], that is:

$$\widehat{\mathbf{m}}_{t+1} = \mathbf{B}_{t+1}\mathbf{G}\mathbf{B}_t^T\mathbf{m}_t, \qquad (6)$$

where, $\mathbf{m}_t$ is the predictor and $\widehat{\mathbf{m}}_{t+1}$ denotes the predictand; **G** represents the variance normalized singular values, i.e., $\mathbf{G} = [\mathbf{\Lambda}/var(\mathbf{B}_t^T\mathbf{m}_t)]$.

For geophysical time-lapse imaging applications, the predictand ($\widehat{\mathbf{m}}_{t+1}$) in Eq.6 can be viewed as an unconditional estimate of model parameters at time *t*+1. In other words, the known or estimated model parameters at time *t* have been projected into the next time step, *t*+1, through the *a priori* temporal covariance, $\mathbf{B}_{t+1}\mathbf{G}\mathbf{B}_t^T$. Since temporal covariance captures coupled modes of variability between two fields, by this temporal projection, we have accounted for the time-variant process responsible for the excitation of the state parameters from $\mathbf{m}_t$ to $\widehat{\mathbf{m}}_{t+1}$.

The next step is to estimate $\mathbf{m}_{t+1}$ conditioned on geophysical data measured at *t*+1. For this reason, we suggest that the coefficients in Eq.6, i.e., $\mathbf{c}_t = \mathbf{B}_t^T\mathbf{m}_t$ are scaled with an appropriate data conditioning matrix, § ∈ $\mathrm{R}^{M\ x\ M}$, where § is a diagonal matrix with its diagonal elements corresponding to the appropriate scaling values. To do this, Eq.6 can be recast to reflect the data conditioning procedure as follows:

$$\mathbf{m}_{t+1} = \mathbf{B}_{t+1}\mathbf{G}\mathbf{c}_t\S. \qquad (7)$$

To increase the flexibility of the proposed scheme to drift away from the *a priori* constraints in order to represent the observed data, **G** in Eq.7 is absorbed into the formulation of the composite regularization operator [see, *Oware and Moysey*, 2014].

Also, since the product $\mathbf{c}_t$§ in Eq.7 will result in another vector of coefficients, Eq.7 can therefore be rewritten in the following compact form:

$$\mathbf{m}_{t+1} = \mathbf{B}_{t+1}\mathbf{c}_{t+1}, \tag{8}$$

where $\mathbf{c}_{t+1}$ is the expansion coefficients at t+1, and $\mathbf{c}_t$ is instead applied as starting coefficients for the optimization of $\mathbf{c}_{t+1}$.

To optimize for the expansion coefficients, $\mathbf{c}_{t+1}$ Eq.8 is implemented within the traditional Tikhonov regularization [Tikhonov & Arsenin, 1977]. The objective function for the optimization can be defined as:

$$\begin{aligned}\mathbf{E}(\mathbf{c}_{t+1}) = \mathbf{E}_d + \beta\mathbf{E}_m &= \left\|\mathbf{W}_d[\mathbf{V}_{obs} - \boldsymbol{f}_{\boldsymbol{g}}(\mathbf{B}_{t+1}\mathbf{c}_{t+1})]\right\|_2 + \beta\|\mathbf{W}(\mathbf{B}_{t+1}\mathbf{c}_{t+1} - \mathbf{B}_t\mathbf{c}_t)\|_2 \\ &= \left\|\mathbf{W}_d[\mathbf{V}_{obs} - \boldsymbol{f}_g^*(\mathbf{c}_{t+1})]\right\|_2 + \beta\left\|\widetilde{\mathbf{W}}\,(\mathbf{c}_{t+1} - \mathbf{c}_t)\right\|_2. \end{aligned} \tag{9}$$

The $\mathbf{E}_d$ term is the data norm, which measures the misfit between observed and modeled data, whereas $\mathbf{E}_m$ is the model norm, which introduces prior information about $\boldsymbol{\sigma}$. The regularization parameter, β, is utilized to tune the relative importance of data fit and model regularization. Additionally, $\boldsymbol{f}_g^*(\cdot)$ denotes a transformed resistivity forward model functional that incorporates the reconstruction of $\boldsymbol{\sigma}$ from the POD basis. The regularization operator, $\mathbf{W}$, contains information that enforces spatial criteria (e.g., flatness and continuity) within the reconstructed images. Note that while the regularization operator, $\mathbf{W}$, acts in the original model space, the composite regularization filter, $\widetilde{\mathbf{W}}$, acts in the transformed coefficient domain. Detailed exposition of the formulation of the composite operator is presented in *Oware and Moysey* [2014]. The data weighting matrix $\boldsymbol{W_d}$ is the inverse of the square root of the data covariance matrix.

Following the optimization of $\mathbf{c}_{t+1}$, $\mathbf{m}_{t+1}$ is evaluated based on Eq.8. To monitor the evolution of the subsequent time periods, the calculated $\mathbf{m}_{t+1}$ is applied as $\mathbf{m}_t$ for the current time step, and the process is repeated recursively in a likewise fashion.

3. RESULTS AND DISCUSSION

The same lab-scale experiment used in Chapter five is applied to demonstrate the suggested MCA time-lapse scheme presented here. Therefore, refer to section 2 in Chapter five for the methods. Images of the first twenty principal basis functions captured for POD and MCA are presented in Figs. 6.2 and 6.3, respectively. Comparison of images of the lab-scale target with tomograms obtained from cascaded (POD) time-lapse (see Chapter Five) and those retrieved from the MCA unconditional estimate (Eq. 6) and MCA reconstructions (Eq. 8) are presented in Fig. 6.4. Also, images of the lab-scale target are contrasted with the mean of simulated training images (TI mean) in Fig. 6.5.

The lateral and vertical spreads of the electrical conductivity (EC) reconstructions obtained from both the cascaded time-lapse (Fig. 6.4, column 2) and the MCA (Fig. 6.4, column 4) appear underestimated. Inspection of the images in Fig. 6.3, however, reveals better match-up of the images of the dye plume of, for instance, time-step t with reconstructed images of the next time-step t+1. This implies that images of the dye plume are leading the images recovered from the resistivity measurements by one time-step (about 30 mins). This observation is plausibly attributable to faster flow rate of the inflow solution at the interface between the glass walls and the soil matrix in contrast to the flow rate within the soil matrix itself. It is important to note that both the dye and resistivity monitoring were done on the same computer; therefore, there was synchronization of the dye and resistivity monitoring time clocks.

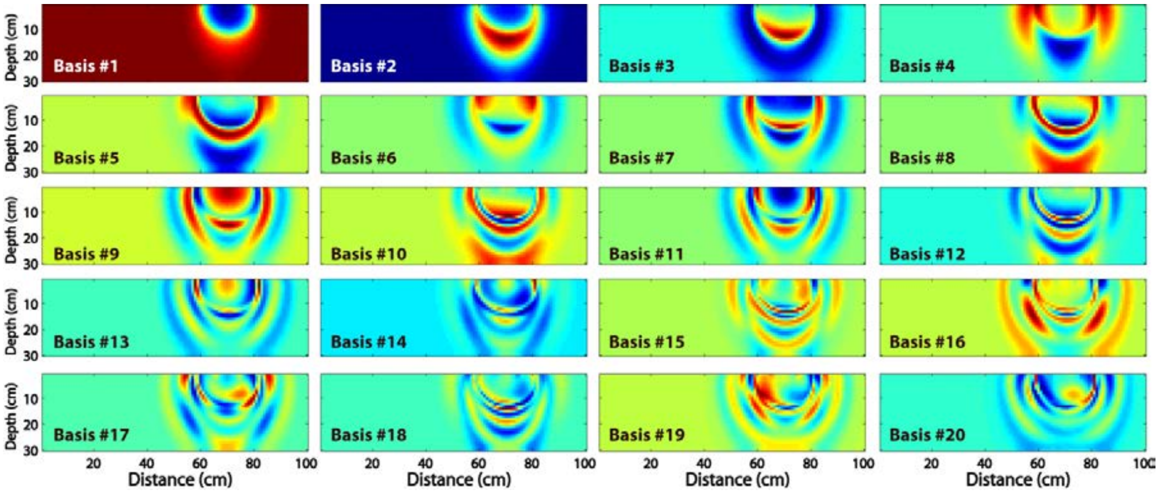

Figure 6.2: Images of first twenty dominant POD basis captured for the first time-step. They are numbered in decreasing order of dominance. Those of the subsequent time steps are not shown, but they follow similar patterns with increasing spread .

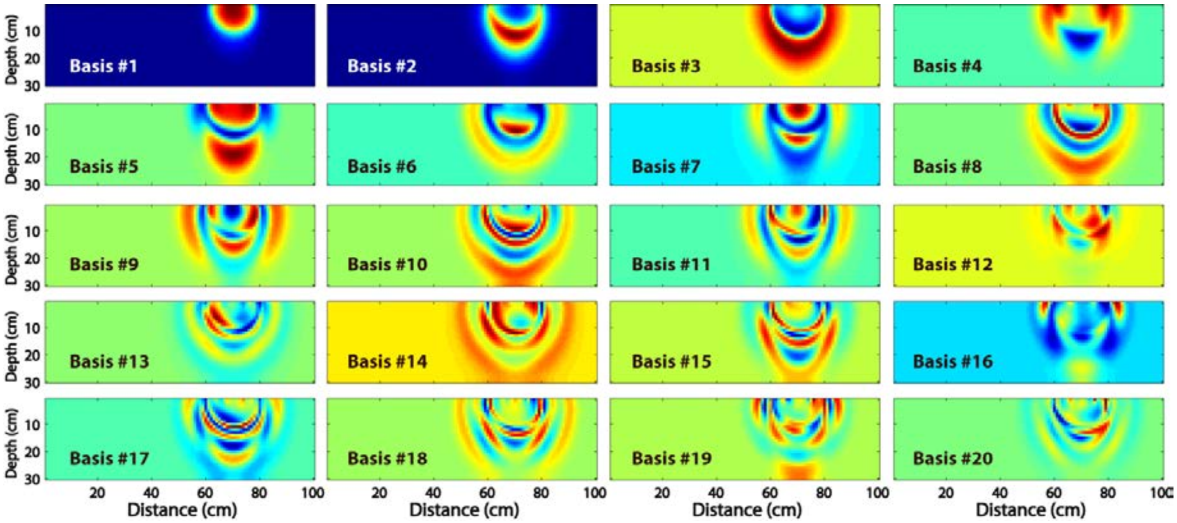

Figure 6.3: Images of first twenty dominant maximum covariance patterns (basis) captured for the first time-step (right basis). They are numbered in decreasing order of dominance. Those of the subsequent time steps are not shown, but they follow similar patterns with increasing spread.

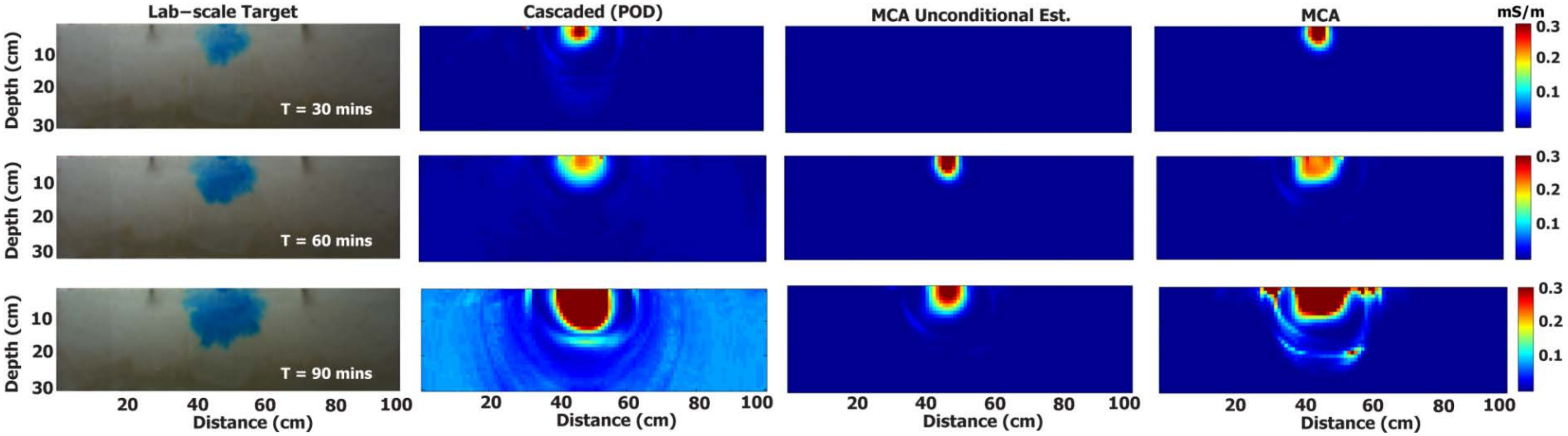

Figure 6.4: Comparison of images of the lab-scale target with tomograms obtained from cascaded (POD) time-lapse and those obtained from the MCA unconditional (Eq. 6) and MCA reconstructions (Eq. 8). (Colum one) Lab-scale target; (Column two) Cascaded (POD); (Colum three) MCA unconditional estimates; (Column four) MCA.

There was clogging of the tracer inflow pipe at the beginning of the experiment, which was detected and rectified. Analyses of all picture frames from video monitoring of the experiment (picture frames not shown) put this clogging event at about 15-25 mins into the experiment. As a consequence, the seeming low peak EC values estimated by both cascade and MCA for the 60 mins time-step compared to the estimated peak EC values for the 30 and 90 mins time-periods (Fig. 6.4) is possibly a further confirmation of the assertion that the resistivity response is lagging the dye plume by about 30 mins. This stems from the fact that the underestimation, which is presumably due the clogging, was expected to be evident in the 30 mins reconstructions instead of the 60 mins tomograms.

Furthermore, even though Fig. 6.5 depicts fairly good match-ups in the lateral and vertical dispersions of the dye images compared to those of the TI mean, those match-ups were, however, not translated into the EC reconstructions. This demonstrates the flexibility of both inversion strategies to drift away from the imposed *a priori* constraints in order to represent the behaviors dictated by the resistivity measurements.

We postulate that the observed temporal discrepancy in the resistivity response time in contrast to that of the dye plume possibly stems from a fast flow rate of the inflow tracer at the interface between the glass walls and the soil matrix, which was monitored by the video camera, as compared to the flow rate within the soil matrix itself, which was monitored by the resistivity measurements.

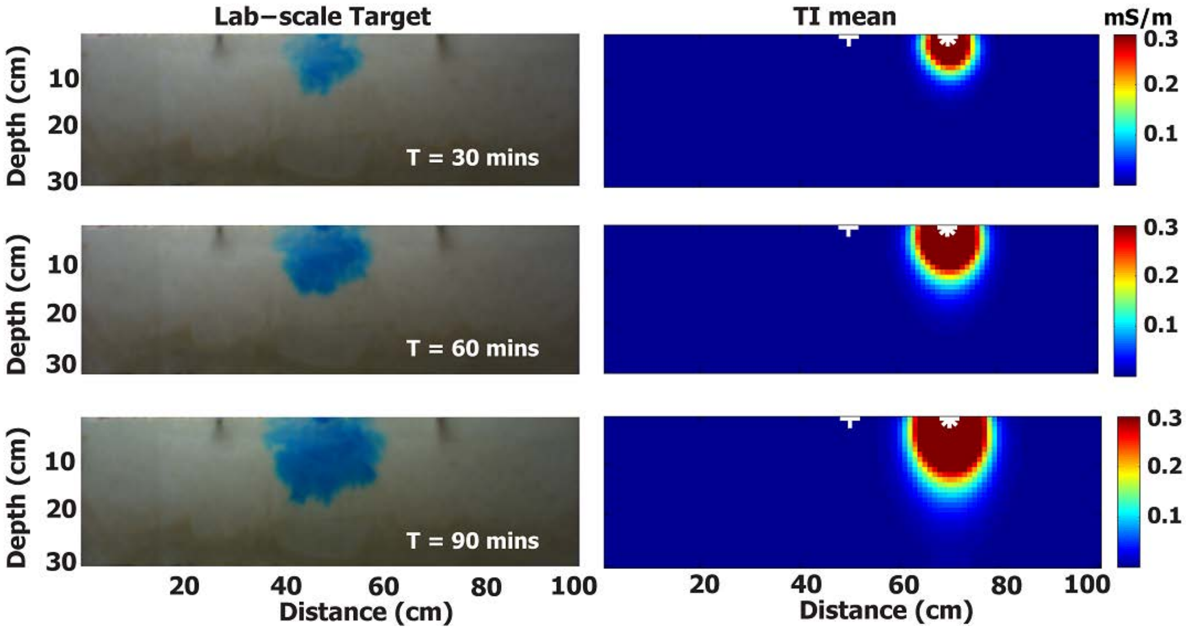

Figure 6.5: Comparison of images of the lab-scale target with those of the mean of simulated training images (TI mean). (Colum one) Lab-scale target; (Column two) TI mean.

In the context of comparison of the cascaded (POD) and the MCA time-lapse inversions, qualitative comparison of the dye images (at time-step *t*) with tomograms obtained from the two strategies (at time-step *t*+1) indicates that the recast from MCA seems superior to those obtained from the cascade (POD) approach. Whiles the MCA approach detected the slightly southwest pointedness in the morphology of the dye plume, the cascaded technique failed to detect that detail. We suggest that the inability of the cascaded (POD) to detect that small detail in the morphology of the target is attributable to lack of variability in the basis functions.

Inspection of the high-order basis in Fig. 6.2, for example, shows several circularly shaped patterns as a result of the homogeneous hypothesis which underpinned the generation of the training dataset. Nevertheless, the same training dataset was utilized in constructing both POD and MCA basis functions (Figs. 6.2 and 6.3). This demonstrates the utility of the complimentary physics-based information incorporated into the starting model of the MCA inversions, which presumably resulted in improved MCA estimations. For instance, while the cascaded approach utilized a baseline tomogram as starting model, the MCA applied their associated unconditional estimates (Fig. 6.4, column three) as starting model, which provided the MCA reconstruction with an additional *a priori* physics-based specification.

4. CONCLUSIONS

We present a novel time-lapse inversion strategy, MCA time-lapse inversion, which seeks to incorporate into starting models of time-lapse inversion procedures, the physics of the time-variance process responsible for the state transitioning between two adjacent time-periods. The potential of the proposed concept was illustrated based on resistivity measurements obtained from lab-scale, saline-tracer unsaturated flow experiment.

We have demonstrated that the incorporation of the physics of the time-variance process into time-lapse starting models provides additional physics-based complimentary information which can result in improved model resolution, as compared to reconstructions based on cascaded time-lapse inversion, which implicitly assumes time-invariance of the process between two adjacent time-periods. However, it is important to emphasize that the predictive ability of the proposed strategy is dependent on the degree of empirical cross-covariance captured between the two successive time steps under study. Therefore, the applicability of the technique may be limited to the investigation of systems in which the physics of the underlying processes are not changing rapidly. In the event of a rapidly changing system, however, we recommend a reduction in the monitored time-step size in order to capture reasonable temporal covariance between the two adjacent fields. Nevertheless, flow in most aquifers is laminar; therefore, the perturbations of the monitored features, in most cases, may typically vary over only diurnal or seasonal temporal spaces.

In this study, we found that the movement of the dye plume leads the resistivity response by about 30 mins. We are of the opinion that the 30 mins temporal discrepancy could probably be smaller if smaller time-step sizes were considered. Whiles lab-scale, dye monitored experiments provide good basis for comparison and validation of geophysical reconstructions, care must, however, be taken to reconcile the infiltrating front of the dye plume with those obtained from the geophysical inversions. Further studies to develop standard techniques to accomplish this reconciliation will be helpful to the advancement of the utilization of dye monitored tank experiments for validating geophysical inversion techniques.

Finally, the study encountered some logistical bottlenecks such as lack of variability in the training dataset due to the assumption of a homogeneous conceptual model. This is in spite of efforts made in packing the tank in order to achieve a homogeneous infiltrating domain. We recognize that this is an almost impossible objective to achieve in real-world application. This challenge will be addressed in future conceptual model by including some small level of heterogeneity in a bid to increase the variability captured in the training dataset. This will enable us to fully demonstrate the true potential of the proposed strategy compared to the cascaded (POD) time-lapse inversion.

REFERENCES

Anno, P., and P. Routh, 2007, A new 4d workflow for legacy seismic data: 77th Annual International Meeting, SEG, Expanded Abstracts, 2888–2892.

Bretherton, C.S., Smith, C., Wallace J.M., 1992. An intercomparison of methods for finding coupled patterns in climate data. J. Climate, 5, 541-560.

Castleman, K. R., 1996. Digital image processing. Prentice Hall, Inc., Upper Saddle River, NJ.

Daily, W., Ramirez, A., 1995. Electrical resistance tomography during in-situ trichloroethylene remediation at the Savannah river site. Journal of Applied Geophysics 33, 239– 249.

Daily, W., Ramirez, A., LaBrecque, D., Nitao, J., 1992. Electrical resistivity tomography of vadose water movement. Water Resources Research 28, 1429– 1442.

French, H., C. Hardbattle, A. Binley, P. Winship, and L. Jakobsen, 2002. Monitoring snowmelt induced unsaturated flow and transport using electrical resistivity tomography, *Journal of Hydrology*, (267), 273–284.

LaBrecque, D.J., Yang, X., 2001. Difference inversion of ERT data. A fast inversion method for 3-D in situ monitoring. Journal of Environmental and Engineering Geophysics 6, 83–89.

Kim, J.H., Yi, M.J., Park, S.G., Kim, J.G., 2009. 4-D inversion of DC resistivity monitoring data acquired over a dynamically changing earth model. Journal of Applied Geophysics 68, 522–532.

Kutzbach, J., 1967. Empirical eigenvectors of sea-level pressure, surface temperature, and precipitation complexes over North America. J. Appl. Meteor., 6, 791-802.

Yeh, T.-C.J., S. Liu, R.J. Glass, K. Baker, J.R. Brainard, D. Alum- baugh, and D. LaBrecque, 2002. A geostastically-based inverse model for electrical resistivity surveys and its applications to vadose zone hydrology. Water Resour. Res. In press.

Ramirez, A., Daily, W., Labrecque, D., Owen, E., Chesnut, D., 1993. Monitoring an underground steam injection process using electrical-resistance tomography. Water Resources Research 29 (1), 73–87.

Slater, L., Binley, A.M., Daily, W., Johnson, R., 2000. Cross-hole electrical imaging of a controlled saline tracer injection. Journal of Applied Geophysics: Special Issue Environmental Geophysics 44, 85–102.

Singha, K., and S.M. Gorelick (2005), Saline tracer visualized with three-dimensional electrical resistivity tomography: Field-scale spatial moment analysis, Water Resources Research, 41, W05023, doi:10.1029/2004WR003460.

Meehl, P.E., 1973. MAXCOV-HITMAX: a taxonomic search method for loose genetic syndromes. In P.E. Meehl, Psychodiagnosis: selected papers.Minneapolis, MN: Univer. of Minneasota Press. Pp 200-224.

Meehl P.E., Yonce, L.J., 1996. Tasometirc analysis: II. Detecting taxonicity using covariance of two quantitative indicators in successive intervals of a third indicator (MAXCOV procedure). Psychological Reports, 78, 1091-1227.

Miller, C.R., Routh, P.S., Brosten, T.R., McNamara, J.P., 2008. Application of time-lapse ERT to watershed characterization. Geophysics, 73 (3), 7-17. doi:10.1190/1.2907156

Hayley, K., Pidlisecky, A., Bentley, L.R., 2011. Simultaneous time-lapse electrical resistivity inversion. Journal of Applied Geophysics, 75, 401-411.

Oldenborger, G.A., Knoll, M.D., Routh, P.S., LaBrecque, D.J., 2007. Time-lapse ERT monitoring of an injection/withdrawal experiment in a shallow unconfined aquifer. Geophysics 72 (4), 177–187.

Oware, E. K., Moysey, S. M. J., Khan T., 2013. Physically based regularization of hydrogeophysical inverse problems for improved imaging of process-driven systems. Water Resour. Res., 49, 1-10. doi:10.1002/wrcr.20462.

Oware, E. K., Moysey, S. M. J., 2014. Geophysical evaluation of solute plume spatial moments using an adaptive POD algorithm for electrical resistivity imaging. Journal of Hydrology, 517, 471-480. doi:x.doi.org/10.1016/j.jhydrol.2014.05.054.

Park, S. K. (1998), Fluid migration in the vadoze zone from 3-d inversion of resistivity monitoring data, *Geophysics*, *63*, 41–51.

Troccoli, A., Harrison, M,, Anderson, D.L.T., Mason, S.J., 2008. Seasonal Climate:

Forecasting and Managing Risk, NATO Science Series. Springer Academic Publishers: Dordrecht, Netherlands.

Tikhonov, A.N., Arsenin, V. Y., 1977. Solutions of ill-posed problems, John Wiley & Sons.

von Storch, H., Zwiers, F.W., 1999. Statistical analysis in climate research. Cambridge University Press.

Wallace J.M., Smith, C., Bretherton, C.S.,1992. Singular-value decomposition of sea surface temperature and 500-mb height anomalies. J. Climate, 5, 561-576.

CHAPTER SEVEN

GENERAL CONCLUSIONS

This dissertation presents two strategies to incorporate physics-based information into geophysical and geostatistical estimation schemes. The inversion strategies presented are Proper Orthogonal Decomposition (POD) and Maximum Covariance Analysis (MCA). The fundamental protocol for both strategies involves the extraction of a set of basis functions for the imaging problem that mimics a particular hydrologic problem of interest using Monte Carlo simulation.

Two synthetic transport scenarios were utilized to test the POD algorithm. Synthetic #1 presents a unimodal plume in which the conceptual transport model was accurate, whereas Synthetic #2 represents a bimodal target that was inconsistent with the conceptualized hypothesis.

First, the performance of the POD inversion strategy was compared with those of the traditional Tikhonov and contemporary coupled inversion schemes. When the conceptual transport model was correct in the first scenario, both coupled and POD-based inversions are able to produce better estimates of the target plume than the Tikhonov inversion. In contrast, the coupled inversion failed when the conceptual model of transport was incorrect in the second scenario. The POD inversion, however, captured the bimodality of the plume by constraining the inversion by *a priori* process information while retaining the flexibility to honor observed geophysical data.

Second, the robustness of the POD-constrained inversion algorithm to input data and model uncertainties were evaluated based on three distinct error components, namely: (1) measurement errors, (2) uncertain *a priori* hypothesis and model complexity, and (3) varying data coverage.

Model resolution deteriorates with increasing measurement noise. Regarding basis constraints, increasing the number of basis functions (inversion parameters) from 100 to 300 produces only marginal or no improvement in model resolution. This finding illustrates a potential lossless truncation capability of the POD algorithm that can reduce the number of inversion parameters. Furthermore, the accuracy of basis functions is critical to the performance of the POD-constrained inversion algorithm. In terms of data coverage, increasing data coverage will not necessarily translate into improvement in model resolution without considering optimal array configuration. In fact, it can lead to a net effect of deterioration of model resolution.

Third, we evaluated the application of the POD algorithm to calibrate subsurface plume spatial moments. An adaptive version of the POD algorithm was also introduced to shift the basis functions to the region of the location of the target plume. The adaptive algorithm recursively refines the position of the basis functions until their position is conditioned on the observed resistivity data.

Final resistivity images provided reasonably accurate representations of the solute plume regardless of issues associated with data noise, the initial training images (TIs) positioning, or conceptual inconsistencies between the target plume and simulations used to generate the TIs.

Estimates for the spatial moments of the plume based on the proposed imaging strategy were compared to those retrieved from the direct sampling of concentration values. Overall, the total mass and center of mass of the plumes could be accurately quantified by the resistivity results, but the spatial spread of the plume was more difficult to constrain. The estimation accuracy of the moments was found to deteriorate as the noise in the resistivity data increases. Spatial moment evaluations for synthetic #1 are better than the estimates for synthetic #2 due to the inaccurate basis functions applied to constrain the reconstruction of synthetic #2. For low noise cases (i.e., the 0 and 3% noise cases in this study), the moments estimated from the resistivity images were found to outperform estimates based on direct concentration sampling until 6-10 multi-level sampling wells were installed. Although this particular number of wells is specific to our example, installing any number of multi-port sampling wells in field applications is not trivial given the time, labor, and cost involved in installing boreholes.

While our study illustrates a successful application of the adaptive POD-based imaging technique, there are a variety of issues that should be noted. First, the approach will not overcome fundamental sensitivity limitations of resistivity data. For example, if the training images are initially located beyond the influence of the resistivity data, then it will not be possible to shift their locations toward the location of the plume using our framework. Second, the POD basis is limited to capturing patterns representative of the conceptual model used to generate the TIs. Additional research is required to evaluate how this problem might be overcome using adaptive training data, supplementing the POD basis with additional patterns, or using geostatistical tools to capture additional spatial variability. Finally, we have not evaluated how the POD imaging technique or the estimated spatial moments of a plume may be affected by fluctuations in the background resistivity of the aquifer caused by geologic variability or associated uncertainties in the petrophysical relationship between concentration and bulk resistivity.

The second inversion strategy introduced here is the MCA time-lapse inversion. In contrast, while POD is a static imaging scheme, MCA is a time-lapse inversion technique. The MCA strategy seeks to account for the time-variant process responsible for the state transitioning between two consecutive states of an evolving system. Resistivity measurements obtained from lab-scale, saline-tracer unsaturated flow experiment were applied to demonstrate the MCA concept. The MCA approach was also compared with the cascaded time-lapse inversion, which does not consider the time-variant mechanism driving the state transitioning.

The MCA results are slightly superior compared to those obtained from the cascaded time-lapse. This observation demonstrates the potential utility of the incorporation of the time-variant process into time-lapse starting models, which provides complimentary information to improve model resolution, as compared to reconstructions based on cascaded time-lapse inversion, which implicitly assumes time-invariance of the process between two consecutive time-periods.

The predictive ability of the MCA strategy is, however, dependent on the degree of empirical cross-covariance captured between the two successive time steps. Therefore, the applicability of the technique may be limited to the investigation of systems in which the physics of the underlying processes are not changing rapidly. In the event of a rapidly changing system, however, we recommend a reduction in the monitored time-step size in order to capture reasonable temporal covariance between the two adjacent fields. Nevertheless, flow in most aquifers is laminar, therefore, perturbations of the monitored features, in most cases, may typically vary over only diurnal or seasonal temporal spaces.

This study encountered some logistical bottlenecks. We suspect potential resistivity sensitivity problems, and also lack of variability in the training dataset due to the assumption of a homogeneous conceptual model. These challenges will be addressed in the future in order to fully demonstrate the MCA concept. The lab experiment will be redesigned and repeated, and small level of heterogeneity will also be introduced into the conceptual model underpinning the generation of the training dataset, in an attempt to increase the variability in the extracted basis functions.

Finally, whiles resistivity data were specifically employed to illustrate the inversion strategies developed in this dissertation, it is important to note that the concepts can be implemented in other geophysical and geostatistical inversion algorithms.